2018
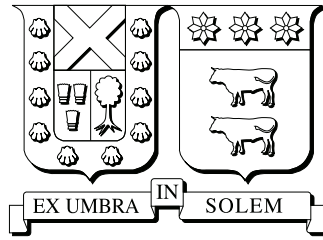
PARTIAL POWER DC-DC CONVERTERS FOR TWO STAGE PHOTOVOLTAIC ENERGY CONVERSION SYSTEMS

ZAPATA AMORES, JAIME WLADIMIR

UNIVERSIDAD TECNICA FEDERICO SANTA MARIA

Partial Power DC-DC Converters for Two-Stage Photovoltaic Energy Conversion Systems

Tesis de Grado presentada por
Jaime Wladimir Zapata Amores
como requisito parcial para optar al grado de
Doctor en Ingeniería Electrónica

Profesor Guía
Dr. Samir Kouro Renaer

Valparaíso, Marzo de 2018

Remember, the force will be with you, always

Obi-Wan Kenobi

RESUMEN

Las configuraciones fotovoltaicas (PV) tradicionales de dos etapas han incrementado su popularidad debido al desacoplamiento entre el voltaje en el enlace-dc y el voltaje a nivel de módulos PV, agregando flexibilidad para extender el rango de operación al realizar el algoritmo de seguimiento de máximo punto de potencia (MPPT). Sin embargo, el convertidor dc-dc adicional incrementa el número de etapas de conversión de energía, y por ende las pérdidas en la etapa de conversión. El concepto de convertidores de potencia parcial (PPC), el cual está enfocado en reducir la cantidad de potencia procesada en la etapa-dc, reduce esta cantidad de pérdidas. Sin embargo, el tipo de topología, la cantidad de potencia procesada y el rango de operación pueden variar de manera significante dependiendo del tipo de aplicación PV. Además, el tipo de funcionamiento de la etapa-dc va a diferir entre operar como etapa de elevación, en caso de un módulo PV, o de reducción cuando el sistema tiene un varios módulos conectados en serie. Esta tesis provee un análisis de las posibles soluciones para realizar las configuraciones PPC, además la aplicación PV más adecuada según la configuración PPC. Para las pruebas se han diseñado tres configuraciones PPC, considerando las más interesante para aplicaciones prácticas. Los resultados experimentales muestran que los PPC incrementan considerablemente la eficiencia global del sistema, aún cuando el convertidor dc-dc tiene una baja eficiencia. Otras ventajas al manejar una potencia menor, es la reducción del tamaño del convertidor sin perder desempeño del sistema.

Palabras Claves

- Convertidores dc-dc
- Energía solar fotovoltaica
- Convertidores de potencia parcial

ABSTRACT

Two-stage photovoltaic (PV) configurations (for microinverters, string or multistring inverters) have become increasingly popular due to the decoupling between the inverter dc-link voltage and the PV voltage, adding flexibility to extend the MPPT range. However, the additional dc-dc converter increases the component count, reduces the volume and power converter losses. The concept of partial power converters (PPC), which reduces the amount of power handled by the dc-stage can mitigate this effect. However, the type of topology, its power and voltage rating, efficiency, and operating range can vary significantly depending on the type of PV application and scale. Furthermore, the type of function of the dc-dc stage will also differ depending on the PV application. From boosting with a high step-up ratio for one module in a microinverter, to a buck mode for larger PV strings when using modern 1500V isolation modules. This thesis provides an analysis of the possible combinations of connections and corresponding applications based on the scale of the PV system. The three most suitable solutions for practical PV systems are further elaborated, including simulations and experimental validation. Experimental results show that the PPC greatly improves the overall PV system efficiency, even when the efficiency of the isolated dc-dc converter is low. An added benefit is that the dc-dc stage power rating achieved are only a fraction of the PV system, reducing size and increasing power density of the power converter without affecting system performance.

Keywords

- Dc-dc converters

- Photovoltaic energy

- Partial power converters

ACKNOWLEDGMENTS

del POWERLAB, y a todos quienes he conocido en cada rincón perdido del mundo. Me es imposible escribir el nombre de cada uno de ustedes en estas pocas líneas, pero de seguro les enviaré un mensaje en Whatsapp y siempre serán bienvenidos en donde sea que me encuentre el día de mañana.

CONTENTS

List of Figures

List of Tables

NOMENCLATURE

Abbreviations

AC	Alternating Current
a-Si	Amorphous Silicon
CdTe	Cadmium Telluride
CIGS	Copper Indium Gallium Selenide
DC	Direct Current
DFIG	Doubly Fed Induction Generator
EMI	Electromagnetic interference
FPC	Full Power Converter
HF	High Frequency
HV	High Voltage
LV	Low Voltage
MPPT	Maximum Power Point Tracking
MPC	Model Predictive Control
PPC	Partial Power Converter
PV	Photovoltaic
STC	Standard Test Conditions

LIST OF SYMBOLS

A_c	Surface area of the converter	cm^2
C_1	Intrawinding capacitance of the transformer primary side	μF
C_2	Intrawinding capacitance of the transformer secondary side	μF
C_{12}	Interwinding capacitance of the transformer	μF
C_c	Clamping capacitance at dc-side	μF
C_{dc}	Capacitance at dc-side	μF
C_p	Parasitic capacitance of the MOSFET	μF
C_{pv}	Capacitance at PV side	μF
C_{cl}	Clamping capacitance	μF
d	Duty cycle	p.u.
f_{sw}	Switching frequency	Hz
G	Solar irradiation	W/m^2
G_v	Global voltage gain	$-$
G_{vc}	Voltage gain of the dc-dc converter	$-$
I_{dc}	Dc-load current	A
I_{in}	Input current of the partial power converter	A
I_{MPP}	Current at maximum power point	A
I_o	Output current of the partial power converter	A
I_{ph}	Cell photocurrent	A
I_{pc}	Converter current in a partial power converter	A
I_{pv}	Photovoltaic current	A
I_{sat}	Cell reverse saturation current	A
I_{sc}	Short-circuit current	A
$I_{L_{lk}}$	Current of transformer the leakage inductance	A
K_B	Boltzmann constant: $1.38e^-23$	J/K
K_{pr}	Partial power ratio	$\%$
L	Inductance in the dc-dc converter	μH
L_1	Leakage inductance of the transformer primary winding	μH

L_2	Leakage inductance of the transformer secondary winding	μH
L_{lk}	Equivalent leakage inductance of the transformer	μH
n	Diode ideal factor	$n = 1$
n_1	Number of turns of the low-voltage side of the transformer	
n_2	Number of turns of the high-voltage side of the transformer	
n_T	Transformer turns ratio	
η_{ac_s}	AC-stage power conversion efficiency	$\%$
η_{dc_c}	dc-dc converter efficiency	$\%$
η_{dc_s}	Dc-stage power conversion efficiency	$\%$
η_t	Global power conversion efficiency	$\%$
P_{ac}	AC-side power	W
P_{ac_l}	Power losses of the dc-ac converter	W
P_{dc}	Dc-side power	W
P_{dc_l}	Power losses of the dc-dc converter	W
p_{dc_l}	Power losses dissipation of the dc-dc converter	W/cm^2
P_{pc}	Power of partial converter	W
P_{pv}	Power of the photovoltaic system	W
P_{sat}	Lower limit of power saturation	W
P_{ring}	Power loss due to ringing	W
q	Electronic charge: $1.6e^-19$	$Coulombs$
R_1	Resistance of the transformer primary winding	Ω
R_1	Resistance of the transformer secondary winding	Ω
R_{dc}	Resistance of the load	Ω
R_s	Cell series resistance	Ω
R_{sp}	Equivalent series resistance of the transformer	Ω
R_{sh}	Cell shunt resistance	Ω
ρ_{dc_s}	Power density of the dc-stage	W/cm^3
ρ_{FPC}	Power density of the full power converter	W/cm^3
ρ_{PPC}	Power density of the partial power converter	W/cm^3
T	Absolute temperature	K
Ts	Period of the driving signal	s
V_{dc}	Dc-link voltage	V
V_{in}	Input voltage	V
V_m	MOSFET voltage	V
V_{MPP}	Voltage at maximum power point	V
V_{oc}	Open-circuit voltage	V
V_{pc}	Voltage in the partial power converter	V
V_{pv}	Photovoltaic voltage	V
V_t	Thermal diode voltage	V

V_{tp}	Voltage at primary side of the transformer	V
V_{ts}	Voltage at secondary side of the transformer	V
V_{FPC}	Volume of the full power converter	cm^3
V_{PPC}	Volume of the partial power converter	cm^3
Ω_o	Natural resonance frequency	rad/s
$W_{L_{lk}}$	Energy stored in the leakage inductance	Joules
ξ	Damping ratio	-
Z_o	Wave impedance	Ω

Chapter 1

INTRODUCTION

THE sustainable development of the modern world in terms of efficient energy management, is highly dependent on the role played by the power electronics. This technology is ushering in a new industrial revolution because of its participation in the current trends, solving problems found in different electrical applications [1]. One of the most important areas relying on the power electronics development is renewable energy applications [2].

An estimated of 303 gigawatts (GW) of solar photovoltaic (PV) global capacity was installed until 2016, the largest annual increase ever, as shown in Fig. 1.1. About 1.0% of the global capacity corresponds to the installed capacity in Chile [3]. Some reasons behind this great development are: the growing environmental concerns, technology development, and the increased competitiveness of PV energy due to the good solar irradiation conditions. Although a PV system are of multidisciplinary nature, including several engineering disciplines, power electronics plays a fundamental role allowing an efficient control of the system and enabling the generated power transfer to the grid [4]. The main drivers behind the development of power electronic technologies are oriented toward more efficient, reliable, lightweight and cost effective power converters.

Considering these approaches, some configurations oriented to work with a reduced portion of the entire power, have been proposed in the literature. This can be achieved using dc-dc converters connected in partial power mode, also known as partial power converters (PPC), which is the focus of the presented work.

1.1 Overview of photovoltaic energy conversion systems

An example of a generic configuration of a grid-connected PV system is depicted in Fig. 1.2. In a traditional PV system, the power generation comes from the PV cells, which can be arranged in a single module, a string of series connected

Gigawatts
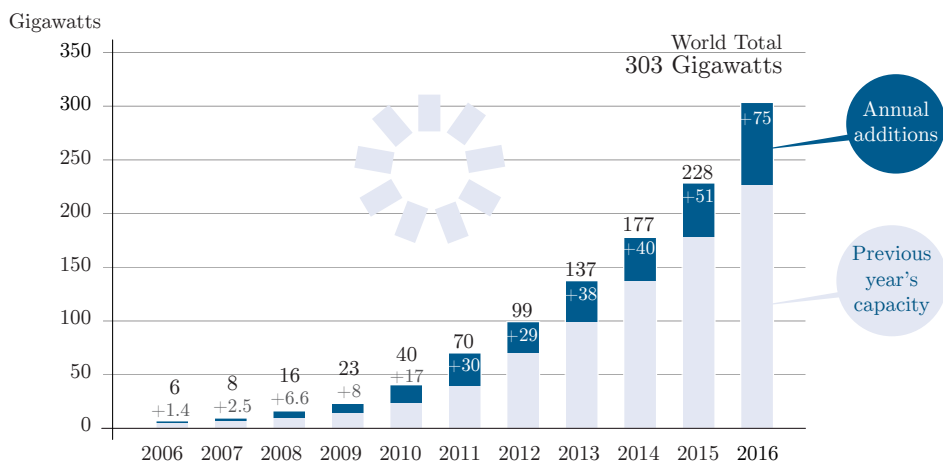
Figure 1.1: Solar PV global capacity and annual additions, 2006-2016 [3].

modules, or an array of parallel connected strings. The generated dc-current greatly depends on the solar irradiation, temperature and voltage at the output terminals of the PV system [5]. The PV system is followed by a passive filter, which is used to decouple the input voltage and current from the subsequent stages by reducing the voltage and current ripple at the PV side. The dc-power is interfaced to the grid by a PV inverter and some additional elements such as grid connection filter, grid monitor or interaction unit, and a low-frequency transformer when local regulations demand for it [6].

Some applications require a decoupling between the PV system and the PV inverter side, hence a dc-stage is included to decouple the PV operating point and the PV inverter control. Because of this additional stage, the PV voltage can be independently controlled by performing any maximum power point tracking (MPPT) algorithm. Additionally, the dc-stage can elevate the PV voltage when it is not high enough for performing grid-connection, or depending on the dc-dc topology this stage can also provide galvanic isolation [4]. Despite of the similar generic structure of grid-connected PV systems, they are not necessarily the same. They can vary in size, power and configuration from small-scale (a single PV module of hundred of watts) to a large-scale PV system (up to hundred of MW). This means that the application will define the suitable power conversion configuration that better adjusts to the needs of the PV system.
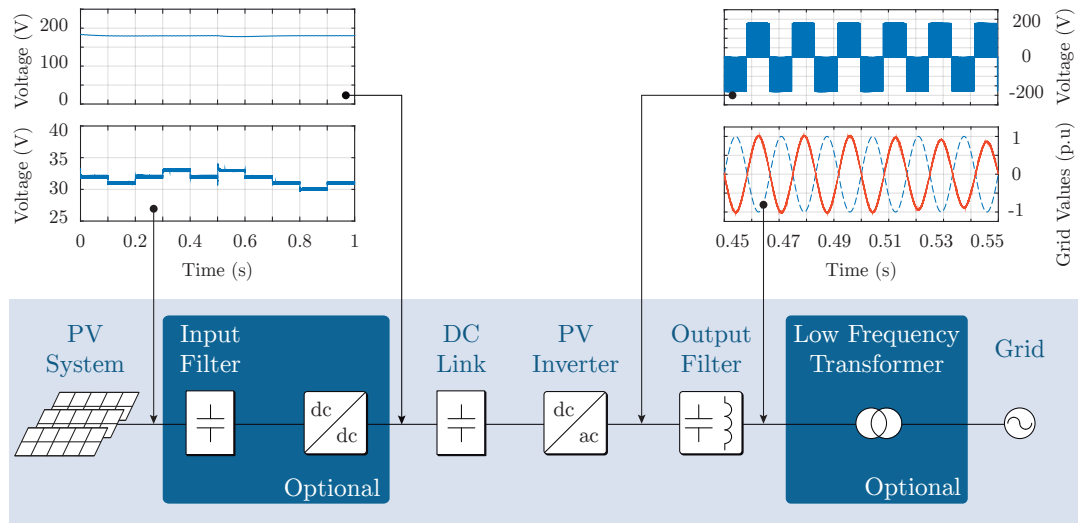
Figure 1.2: Generic structure of a grid-connected PV system.

1.1.1   Photovoltaic energy conversion

The photovoltaic phenomenon is an internal effect of some semiconductor materials, by which the photons of equal or greater energy than the band gap of the semiconductor material can excite and free the electrons. Basically, the photovoltaic cells are made of layers of crystalline silicon devices (mono-crystalline and poly-crystalline), or by using thin-film devices (copper indium gallium selenide (CIGS), cadmium telluride (CdTe) and amorphous silicon (a-Si)) [7]. The solar cell can be understood as a specialized semiconductor diode with a large barrier layer which is exposed to light. It allows forward current to flow from the p-side to the n-side polarizing directly the diode [8]. When the diode is exposed to solar irradiation, the photocurrent is generated being proportional to the solar irradiation.

Some models have been developed to represent the PV behavior. But in all the cases, the single-diode model shown in Fig. 1.3 (a), which includes a series and a parallel resistor connected with the diode and a current source, was selected as the best approach based on a good balance between accuracy and model complexity [9]. Moreover, this model allows the possibility to express voltage as a function of the current, and its inverse. Additionally, the single-diode model can be expressed into two explicit mathematical equations by using Lambert's $\mathcal{W}$ function, which expresses the PV voltage exclusively in terms of the PV current, and vice versa [10], [11]. The single-diode model is described
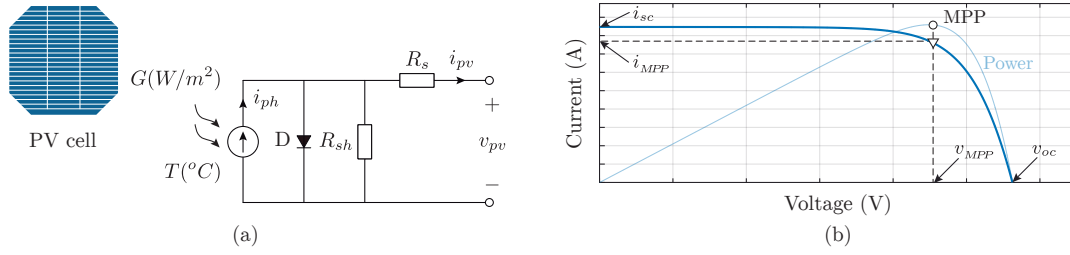
Figure 1.3: (a) Single-diode model of a PV cell. (b) Operation curve of a PV module.

with the following equation [12]:

$$I_{pv} = I_{ph} - I_{sat}\left(e^{\frac{V_{pv} + R_s I_{pv}}{V_t}} - 1\right) - \frac{V_{pv} + R_s I_{pv}}{R_{sh}} \qquad (1.1.1)$$

The electric characteristics of a PV module highly depends on the environmental factors (temperature and solar irradiation). In addition, Eq.1.1.1 shows the PV current i_{pv} as a relation of its output PV voltage v_{pv}, where a number of parameters of the model are described as follows:

- *Cell photocurrent I_{ph}*: This current mainly depends on the solar irradiation, also it is linearly dependent with the temperature T and the short circuit current I_{sc}^o under standard test conditions (STC) [13]. The cell photocurrent can be expressed with the following equation:

$$I_{ph} = G(K_{ipv}(T - T_{ref}) + I_{sc}^o) \qquad (1.1.2)$$

  where, G is the solar irradiation expressed in (W/m^2), T the temperature in ^oC, I_{sc}^o under STC (G=1000W/m^2, T=25^oC), and K_{ipv} is the coefficient of temperature dependency.

- *Cell reverse saturation current I_{sat}*: This current increases roughly exponentially as temperature rises, and it is also influenced by the semiconductor characteristics.

- *Thermal diode voltage V_t*: This voltage consider the PV cell temperature and diode ideal factor (n). The equation is expressed as follows:

$$V_t = \frac{nK_B T}{q} \qquad (1.1.3)$$

  where, K_B is the Boltzmann's constant, and q is the charge of an electron.
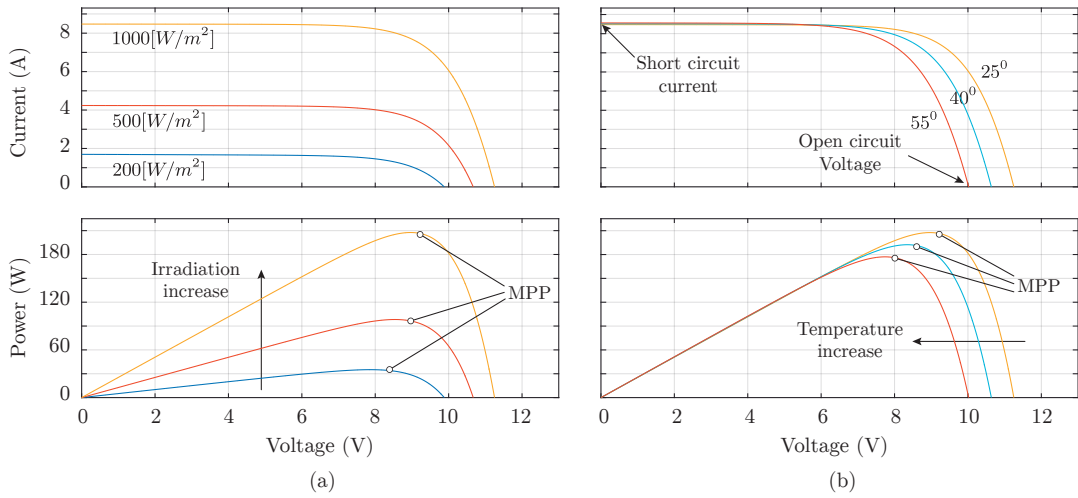
Figure 1.4: I-V and P-V curves of a PV module under: (a) Different solar irradiation at $25^o C$. (b) Different temperature at $1000 \ W/m^2$.

- *Serial and Shunt resistor R_s and R_{sh}*: The serial resistor depends on the temperature and irradiation level, it has a significantly influence on the MPP of the characteristic curve of a solar cell. On the other hand, the shunt resistor commonly is significantly larger than the serial resistor, for that reason this parameter is often neglected.

The typical PV current-voltage (I-V) and power-voltage (P-V) curves are illustrated in Fig. 1.3 (b). The PV module behaves as a dc-current source with a maximum value when it is short-circuited I_{sc}, remaining in an almost constant value while the voltage at the output terminals increases. When the voltage gets higher, the current gets lower until it reaches zero at the open-circuit PV voltage V_{oc}. From the P-V curve it is possible to note that the power rises when the voltage increases until it reaches a maximum power point. For voltages higher than the MPP, the power starts to descend. The main objective of the control system is to find the V_{MPP} voltage, which allows to extract the maximum power of the PV system.

However, the PV curve varies depending on the environmental conditions (solar irradiation and temperature) as depicted in Fig. 1.4. Working at the same temperature, as can be seen in Fig. 1.4 (a), the short-circuit current I_{sc} is highly linear-dependent on the solar irradiation. Consequently, the P-V curve which is obtained by multiplying the axes of the I-V curve, also varies with three operation features: a constant positive $dp/dv > 0$ slope equal linearly

proportional to the generated current, a zero slope $dp/dv = 0$ in the MPP and, a negative slope until zero power is reached at the open-circuit voltage v_{oc}. The slopes of the PV curves can be adjusted by the series and shunt resistances of the electrical PV cell model to achieve a better representation of the real PV cell. In contrast, the open-circuit voltage is not affected as much as the short-circuit current by the solar irradiation, but it varies significantly depending on the operating temperature. It is shown in Fig. 1.4 (b), where the voltage is reduced while the temperature increases, leading to a lower power generated by the PV module.

1.1.2   Explicit model of a photovoltaic cell

The single-diode model of a PV cell (1.1.1), does not express the electrical behavior through independent terms. For that reason, it is not possible to express the equation for PV current I_{pv} as a explicit function of the PV voltage V_{pv}, or vice-versa. However, a explicit solution for the PV current and voltage can be derived using the Lambert's $\mathcal{W}$ function. It leads to an computationally efficient model of the PV cell, resulting in significantly reduced calculation times and improved robustness of simulation [14].

The Lambert's $\mathcal{W}$ function is defined to be multivalued inverse of the function:

$$\mathcal{W}^{-1} : x \rightarrow xe^x \tag{1.1.4}$$

If x is a real number, as is depicted in Fig. 1.5, then for $-1/e \leq x < 0$ there are two possible real values of $\mathcal{W}(x)$. The Lambert's $\mathcal{W}$ function is expressed as two branches. The branch satisfying $-1 \leq \mathcal{W}(x)$ is denoted by $\mathcal{W}_0(x)$, which is referred as the principal branch being an increasing monotonic function. It means that a positive real number will have a unique solution. On the other hand, the branch satisfying $\mathcal{W}(x) \leq -1$ is denoted by $\mathcal{W}_{-1}(x)$.

The applications come from the problem to solve equations where linear and exponential responses are combined as:

$$y = x + ae^x \tag{1.1.5}$$

By using the Lambert's $\mathcal{W}$ function, it is possible to find the explicit solution as:

$$(y - x)e^{-x} = a$$
$$(y - x)e^{y-x} = ae^y$$
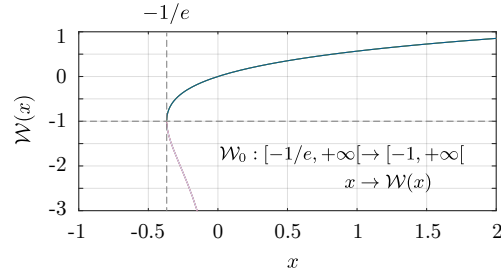
Figure 1.5: Lambert's $\mathcal{W}$ function for real values.

$$y - x = \mathcal{W}(ae^y)$$

$$x = y - \mathcal{W}(ae^y) \tag{1.1.6}$$

Moreover, the derivate of the Lambert's $\mathcal{W}$ function can be expressed as:

$$\mathcal{W}'(x) = \frac{\mathcal{W}(x)}{x(1 + \mathcal{W}(x))} \tag{1.1.7}$$

Due to the transcendental nature of the single-diode model describing the current-voltage relation of the PV cell, the explicit solution can be found by using the Lambert's $\mathcal{W}$ function.

Explicit photovoltaic current expression

Considering the single-diode model described in (1.1.1), and rearranging the terms, the expression can be expressed as:

$$
\begin{aligned}
\frac{R_s R_{sh}}{(R_s + R_{sh})V_t}(I_{ph} + I_{sat}) = {} & \frac{V_{pv}\left(\frac{R_s}{R_s + R_{sh}}\right) + R_s I_{pv}}{V_t} \\
& + \frac{R_s R_{sh} I_{sat}}{(R_s + R_{sh})V_t} e^{\frac{R_{sh} V_{pv}}{(R_s + R_{sh})V_t}} e^{\frac{V_{pv}\left(\frac{R_s}{R_s + R_{sh}}\right) + R_s I_{pv}}{V_t}}
\end{aligned}
\tag{1.1.8}
$$

By considering:

$$y = \frac{R_s R_{sh}}{(R_s + R_{sh})V_t}(I_{ph} + I_{sat})$$

$$x = \frac{V_{pv}\left(\frac{R_s}{R_s + R_{sh}}\right) + R_s I_{pv}}{V_t}$$

$$a = \frac{R_s R_{sh} I_{sat}}{(R_s + R_{sh})V_t}e^{\frac{R_{sh} V_{pv}}{(R_s + R_{sh})V_t}}$$

The equation has the form presented in (1.1.5), which can be solved using the Lambert's $\mathcal{W}$ function as (1.1.6). Then, the PV current can be expressed as an explicit function of the PV voltage as:

$$I_{pv} = \frac{V_t}{R_s}[y - \mathcal{W}(ae^y)] - \frac{V_{pv}}{R_s + R_{sh}} \tag{1.1.9}$$

In order to simplify the calculation, a simplified model is derived considering that $R_s << R_{sh}$, then:

$$\frac{R_s R_{sh}}{R_s + R_{sh}} \simeq R_s \tag{1.1.10}$$

In that case, (1.1.9) can be expressed as:

$$I_{pv} = \frac{V_t}{R_s}\left[\frac{R_s(I_{ph} + I_{sat})}{V_t} - \mathcal{W}\left(\frac{I_{sat}}{V_t}R_s e^{\frac{V_{pv}}{V_t}}e^{\frac{R_s(I_{ph} + I_{sat})}{V_t}}\right)\right] - \frac{V_{pv}}{R_{sh}} \tag{1.1.11}$$

Explicit photovoltaic voltage expression

In the same way, using the Lambert's $\mathcal{W}$ function it is possible to express the PV voltage as an explicit function of the PV current as:

$$\frac{R_{sh}}{V_t}(I_{ph} + I_{sat} - I_{pv}) = \frac{R_{sh} I_{sat}}{V_t}e^{\frac{V_{pv} + R_s I_{pv}}{V_t}} + \frac{V_{pv} + R_s I_{pv}}{V_t} \tag{1.1.12}$$

By considering:

$$y = \frac{R_{sh}}{V_t}(I_{ph} + I_{sat} - I_{pv})$$

$$x = \frac{V_{pv} + R_s I_{pv}}{V_t}$$

$$a = \frac{R_{sh} I_{sat}}{V_t}$$

Table 1.1: PV module parameters of Sunmodule SW 280 Mono Black at STC.

Parameter	Symbol	Value
PV power	P_{pv}	$280W$
Open-circuit voltage	V_{oc}	$39V$
Voltage at maximum power point	V_{mpp}	$31.8V$
Short-circuit current	I_{sc}	$7.74A$
Current at maximum power point	I_{mpp}	7.22
Cell series resistance	R_s	$3m\Omega$
Cell shunt resistance	R_{sh}	2.8Ω
Cell reverse saturation current	I_{sat}	$6.33e-9A$
Cell photocurrent	I_{ph}	$7.74A$

Then, the PV voltage can be expressed as an explicit function of the PV current as:

$$V_{pv} = V_t \left[y - \mathcal{W}\left(ae^y\right) \right] - R_s I_{pv} \tag{1.1.13}$$

$$V_{pv} = V_t \left[\frac{R_{sh}}{V_t}(I_{ph} + I_{sat} - I_{pv}) - \mathcal{W}\left(\frac{R_{sh}I_{sat}}{V_t} e^{\frac{R_{sh}}{V_t}(I_{ph}+I_{sat}-I_{pv})} \right) \right] - R_s I_{pv} \tag{1.1.14}$$

As can be seen, now the PV cell is represented by an explicit model. It has been analyzed in depth in the literature, and the accuracy of the technique also has been tested [15]. In this presented work, this model will be used in order to estimate the operation range ot the PV cells, specially under partial shading conditions.

In order to show the application of the Lambert's $\mathcal{W}$ function, a commercial PV module has been modeled using the explicit PV voltage expression. The PV module parameters are listed in Table 1.1.

The theoretical evolution of the PV curves, under different solar irradiation changes, are depicted in Fig. 1.6, where the maximum power points are marked. It is worth noticing that it is possible to obtain an accurate model of the PV module using an explicit model. Moreover, in Fig. 1.7 it is possible to see the PV voltage reduction under the variation of the solar irradiation, in this case a variation between $50-1000(W/m^2)$ is made. Under this condition, the obtained results are a PV voltage V_{mp} reduction of 20.9%. This result highlights the effect of the solar irradiation changes over the PV voltage.
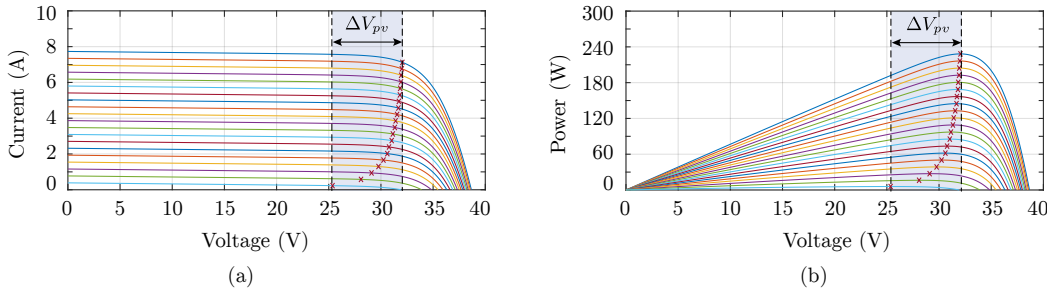
Figure 1.6: PV curves obtained with explicit expression using Lambert's function. (a) I-V PV curve. (b) P-V PV curve.
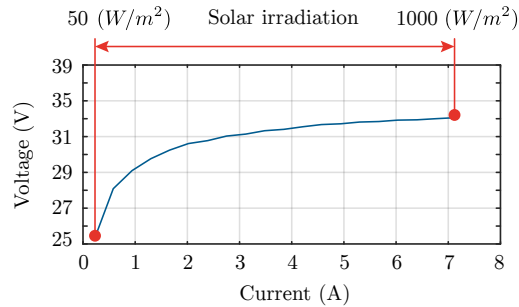
Figure 1.7: PV voltage variation in terms of the PV current variation under different solar irradiation.

1.1.3   Operation under partial shading

Normally, PV cells have a low open-circuit voltage hence, it is necessary to create a string of PV cells connecting them in series. Moreover, in order to increase the power of the PV system, the strings are connected in parallel forming an array. In the case of identical PV cells operating under uniform conditions (solar irradiation and temperature), the voltage and current of the PV array are proportional to the PV cells connected in series, and the strings connected in parallel. However, the uniform conditions are not always warranted then, the PV system will have a different behavior depending on module mismatch and partial shading effect.

The non-uniform conditions are mainly related with short-term effects (clouds and obstacles) and long-term conditions (snow and soiling effect [16]). These conditions can reduce the energy yield of the PV system and, it also could lead in the deterioration of the PV cell because of hot spots [8]. A commercial PV module is typically made by the series connection of PV cells (60 or 72 cells)
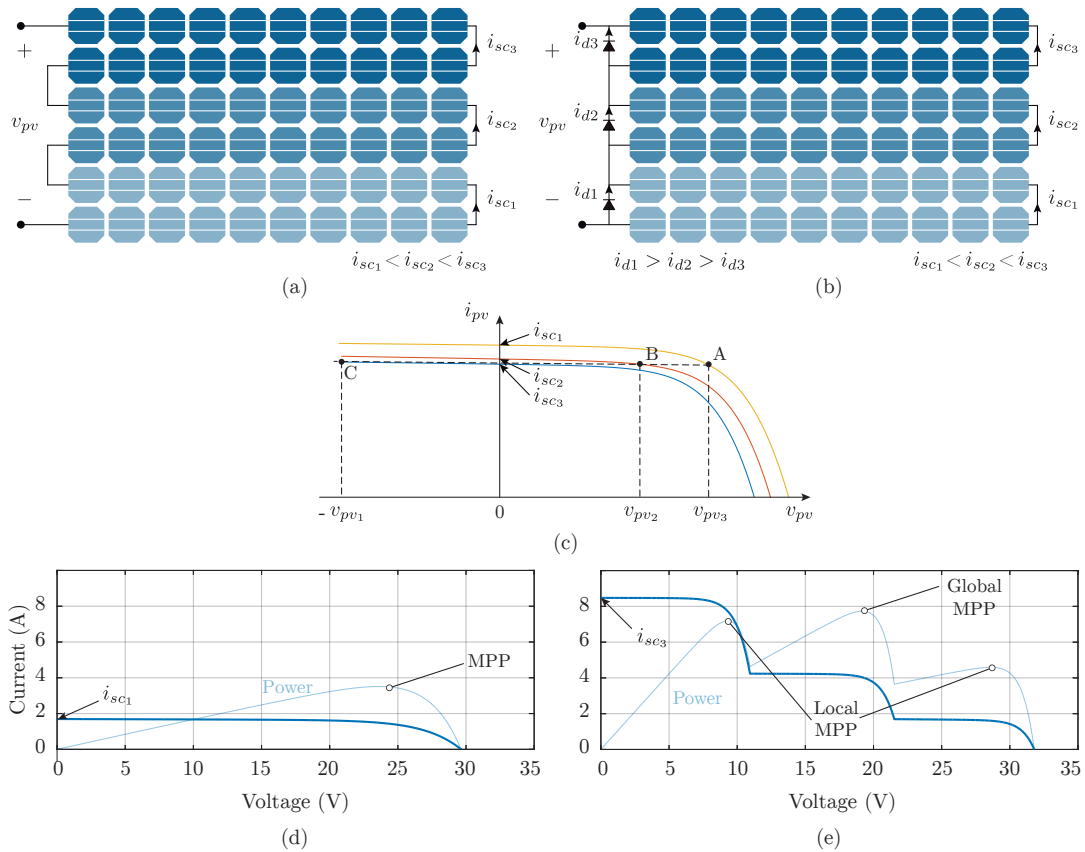
Figure 1.8: Operation under partial shading. (a) PV module without bypass diodes under three different solar irradiation levels. (b) PV module with bypass diodes under three different solar irradiation levels. (c) I-V curve of the shaded PV module. (d) I-V and P-V curves of a PV module without bypass diodes. (e) I-V and P-V curves of a PV module with bypass diodes.

[17], and they are connected in parallel to one diode in groups of 20 or 24 PV cells (3 diodes per PV module) forming small strings inside the PV module. In a generic case, as is depicted in Fig. 1.8 (a), the shaded strings will have a reduced photocurrent (depending on the shaded area). In this case when there are no bypass diodes connected to the PV cells, the current generated by the other cells flows trough the shunt resistor R_{sh} resulting in a high negative voltage [18]. Since this resistor is usually large, the shaded cell reduces the output voltage in the PV module instead of adding to it.

This effect is depicted in Fig. 1.8 (c), where the I-V curves are drawn for the

three different PV strings. In that case, for an operation of the PV module at point A of the characteristic, due to the series connection, the same current will flow trough the PV module resulting in a operation at point C for the more shaded string. It means that those cells will work with large negative voltage functioning as receptors, which will lead to degradation or destruction of the PV cells. In order to overcome this problem, bypass diodes are connected in parallel to a group of PV cells. In that case, the current passes trough the diode of the shaded group resulting in a semiconductor voltage drop.

In the same way, working with parallel strings the blocking diodes (connected in series with the string) are required to prevent reverse currents flowing into the strings with lower voltage. In commercial PV modules the bypass diodes are already included within the same module, but the blocking diodes have to be added by the user when the parallel connection is made.

The protection diodes influence the global behavior of the PV system. Working with no protection diodes, the power characteristic shown in Fig. 1.8 (d), presents a similar behavior as an uniform condition with the difference that the global power is reduced because of the shaded string. However, when the diodes are included, they avoid the decrease of the short circuit current i_{sc} during partial shading. Nevertheless, the power characteristic, depicted in Fig. 1.8 (d), shows the presence of multiple local maximum power points instead of a single one. This effect presents a challenge for the control algorithm searching the global maximum power point, which can affect the power yield of the PV system.

1.2   Two-Stage Photovoltaic Energy Conversion Systems

The most common applications where a PV system is implemented are the standalone configurations and grid-connected systems [19]. The standalone PV system has practical values in off-grid areas such as microgrids. However, the power generation is highly dependent of the atmospheric conditions and normally they require additional storage devices to balance the energy of the PV system [20]. On the other hand, the grid-connected PV systems do not require batteries since all the power is directly supplied to the grid for direct consumption [5]. Then, grid-connected systems are more cost-effective and require less maintenance than standalone PV systems.

1.2.1 Traditional grid-connected PV system architectures

The grid-connected PV systems are not always the same, they can vary in size and power, from small-scale (a single PV module of a hundred of watts) to a large-scale power plant (currently up to $1000MW$, Kurnool Solar Park, India [21]). For that reason, several power converter configurations are developed to address the needs of each PV system. The traditional grid-connected PV systems can be grouped into four architectures, as depicted in Fig. 1.9: Central inverter for large-scale PV systems, multistring inverter for large and medium-scale PV systems, string inverter for medium and small-scale systems, and microinverter for small-scale systems [22].

Centralized architecture, depicted in Fig. 1.9 (a), is oriented to large-scale PV systems. The advantages are: high conversion efficiency under uniform atmospheric conditions, simple structure and control system due to the single central inverter. However, the main drawback is the reduction of the generated power in case of partial shading. Therefore, the use of protection diodes are required, leading to power losses because of the external semiconductors [23].

Multistring architecture, depicted in Fig. 1.9 (b), allows individual MPPT made by the dc-stage and it also provides voltage elevation and isolation if is required. Therefore, this configuration is implemented in medium and small-scale PV systems, keeping a high efficiency in case of partial shading conditions. Among the drawbacks there are the component counts, increment of control systems and DC-cables losses because of the connections.

String inverter architecture, depicted in Fig. 1.9 (c), uses one inverter per PV string avoiding the need to add series blocking diodes. The input voltage is high enough to avoid an elevation stage and a separate MPPT can be applied to each string. The main drawbacks of this topology are the higher component counts, and several individual control systems to perform grid connection.

Finally, the small-scale PV systems use the microinverter architecture depicted in Fig. 1.9 (d). It has the most flexible architecture among all those presented previously, since one converter is connected to each PV module in order to do the MPPT. The main drawback is the low conversion efficiency due to the high voltage elevation stage required for the grid-connection.

The main features of the traditional grid-connected PV systems are listed in Table 1.2 [4].

1.2.2 Two-stage configurations

The traditional single-stage architectures (string and central inverters) for several years have been a mainstream solution for grid-connected PV systems. The
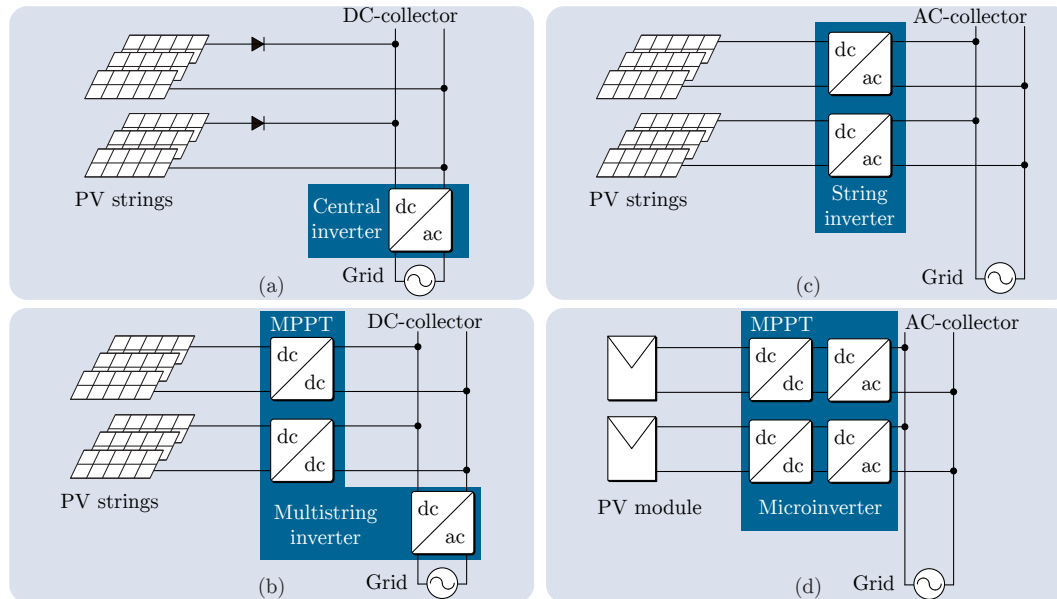
Figure 1.9: Traditional grid-connected PV system architectures. (a) Central inverter. (b) Multistring inverter. (c) String inverter. (d) Microinverter.

Table 1.2: Important features of traditional grid-connected PV system architectures.

Config	Power range	Advantages	Disadvantages
Central inverter	<1.6MW	Simple design, highest converter efficiency, reliable	Blocking diodes, poor MPPT performance, not flexible
String inverter	<10kW	Good MPPT efficiency, reduced DC-wiring, transformerless	High component counts, several grid control systems (1 string 1 inverter)
Multistring inverter	<500kW	Flexible/modular, high MPPT efficiency, low cost for multiple string system	Two-stage is mandatory
Microinverter	<300W	Flexible/modular, highest MPPT efficiency, easy installation	Higher losses, higher cost per watt, two-stage is mandatory

most important reasons are the lower initial cost and lower conversion losses compared with a two-stage approach. Nevertheless, recently more demanding grid-codes have been introduced, especially for large PV systems with central
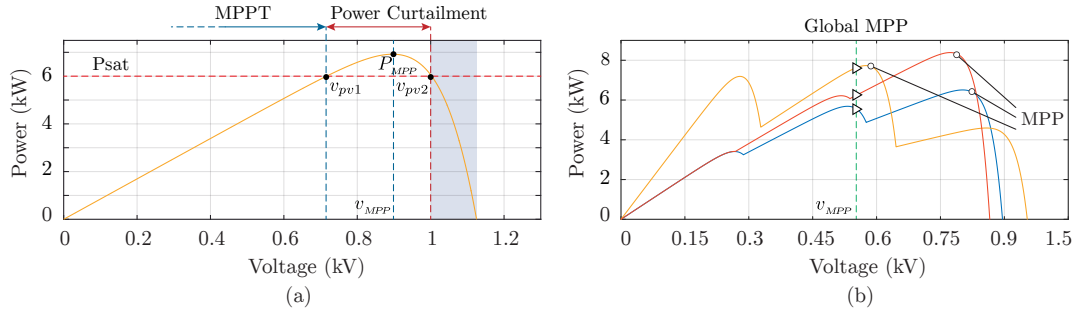
Figure 1.10: PV curves for one-stage PV systems. (a) Frequency regulation (power curtailment). (b) Operation under partial shading.

inverters. One of these regulations obligate to perform frequency regulation through curtailment, which forces the PV system to forfeit power and not operate in its maximum power point [24]. As shown in Fig. 1.10 (a), the PV system is saturated to a lower power point P_{sat} operating with a string voltage v_{pv_1} (v_{pv_2} is avoided because of the steep power slope, and there is the risk to operate at the maximum allowed PV string voltage). The power limitation is obligatory in order to have the possibility to increase the power when required according to the curtailment slope. On the other hand, v_{pv_1} must be high enough to be properly controlled by the central inverter, which requires a voltage higher than the grid peak voltage. This leaves a little room for MPPT algorithm, reducing the energy yield of the PV system. This problem becomes even more dramatic in case of partial shading (presence of clouds, dust, snow) in the individual strings of the PV array. As shown in Fig. 1.10 (b), there are three different PV characteristics for the individual strings of the PV array connected to the central inverter. In that case, the inverter operates in the global MPP in order to extract the maximum power by the PV system. However, as is depicted in the figure, this point is far from the individual maximum power points, leading a reduced energy yield. One solution to address the problem is by introducing storage from which the extra power for frequency regulation is obtained, the related problem of that solution is the incremental cost of the entire PV system.

For that reasons, two-stage power conversion systems became increasingly popular. The additional dc-stage augments the MPPT range, due to the decoupling between the inverter DC-link and the PV voltage. Moreover, for small scale applications where microinverters are installed, the DC-stage is mandatory in order to elevate the voltage and perform grid-connection [5]. In addition, the effect of partial shading is mitigated if several DC-stages are used (multistring

Table 1.3: PV system configurations depending on the number of stages and isolation requirements.
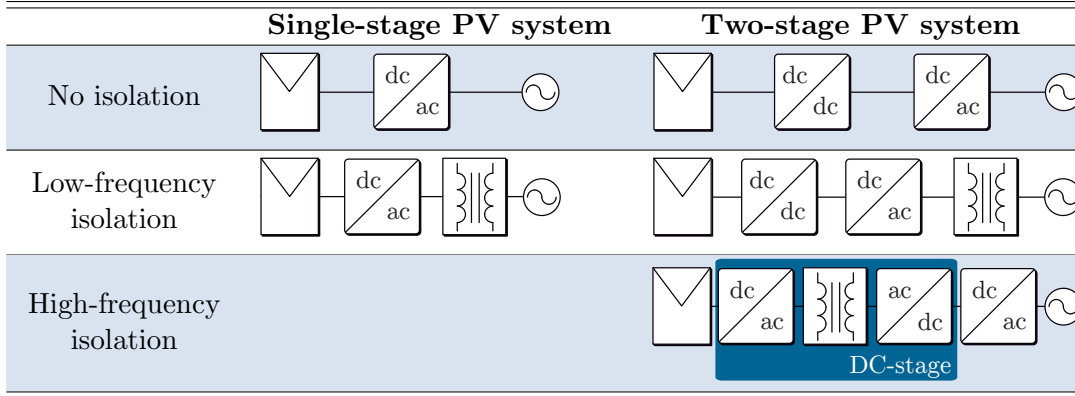
architecture), and the energy yield is increased due to the multiple independent MPPT for smaller strings or arrays [25]. This approach is changing the market share of the PV industry, where companies such as Huawei are currently leading the PV industry, by delivering high-efficiency two-stage conversion systems with up to 4 independent strings [26].

On the other hand, the additional conversion stage leads to an increase of the component counts, which is translated in an additional initial cost and more conversion losses. Furthermore, the power density seems not to be a problem for large-scale PV systems where central inverters are used, but once the two-stage approach was adopted, the reduction of the converter size and weight to $50kg$ has became important (weight limit of most labor laws admissible for two people to carry), besides it has also benefits in shipping costs.

All of these challenges motivate the development of new power conversion systems, by tackling the two main issues regarding the two-stage power conversion systems (efficiency and power density), without affecting the reliability and functionality of the PV system. Table 1.3 summarizes all the possible combinations between single and two-stage architectures, which are found in traditional PV systems depending on the isolation requirements.

1.3 Goals and Contribution of the Thesis

The work made in this thesis, relates to the study of the partial power converters (PPC) for two-stage PV inverters. The main objective of this thesis is to analyze the partial power conversion concept applied to PV energy conversion

systems, design and develop dc-dc converters for different PV applications by considering the suitable partial power converter configuration. The results are verified with simulations and experimental measurements from prototypes built in the laboratory. The contributions of the thesis are listed as follows:

- Increase the efficiency of two-stage grid connected photovoltaic energy conversion systems, by significantly reducing the amount of power processed by the dc-stage, without loss of functionality and performance.

- Analyze the different partial power converter configurations, and determine depending on the PV applications, the most suitable configuration to reduce the power ratio of the converter and increase the operation of the PV system.

- A detailed analysis of the behavior of parasitic components presented in the isolated dc-dc topologies, and its effect on the converter operation.

- Design, build and test laboratory prototypes of partial power converters for experimental validation of the presented goals.

- Obtain the conversion efficiency based on experimental measurements, and compare the increment of efficiency of the dc-stage with the isolated dc-dc converter used to create the PPC configuration.

1.4   Outline of the Thesis

The thesis is oriented to present a comprehensive analysis of the partial power converters, using as an alternative for the dc-dc converter in two-stage PV systems. Then, in order to give a motivation to investigate the PPC converters in detail, the fundamental basis and the problems found in traditional PV applications are presented in Chapter 1.

In Chapter 2 the overview of the partial power conversion concept is presented, also the solutions found in the literature and the main advantages in contrast with traditional solutions. Moreover, in the same chapter it is provided a theoretical validation of the main advantages of the partial power converters as the increment of efficiency and the power density. Moreover, the explicit model of the PV voltage is discussed in order to make further analysis in terms of operation performances.

The importance of isolation and some traditional isolated dc-dc converters, are presented in Chapter 3. Moreover, some discussions about of the challenges

working with high-frequency topologies are also found. In addition, some experimental measurements are presented in order to enhance the validation of the analysis.

The core of the thesis is presented in Chapter 4. In this chapter the theoretical analysis and the classification of the possible configurations of PPC based on isolated dc-dc topologies, are discussed. Moreover, it is also discussed the constraints, limitations and suitable PPC configurations for further evaluations based on the more practical interest in PV applications.

The detailed mathematical model for each proposed PPC configuration, as well as the implemented control schemes, are presented in Chapter 5.

Additionally, in order to make a first evaluation of the PPC configurations, some simulation results are presented in Chapter 6. The importance of this chapter is to provide a comprehensive evaluation of PPC configurations considering ideal and controlled scenarios. With this information a clear sight of the advantages working with PPC is obtained.

In order to evaluate the hypothesis and analyze the challenges found in real power systems, some laboratory prototypes were built and the results are presented in Chapter 7. Moreover, the discussion about the efficiency and the variation of partial power ratio in different operation points are also presented. Finally, the work concludes with a summary of the main remarkable conclusions and an outlook of some considerations for future research related with the partial power conversion.

Chapter 2

OVERVIEW OF PARTIAL POWER CONVERTERS

THE traditional Full Power Converter (FPC), process the entire power delivered by the source P_{pv}, because of the direct path between the PV system and the dc-ac converter as depicted in Fig. 2.1 (a). Due to the dc-power conversion losses $P_{dc,l}$, the output dc-power P_{dc} is lower than the input power, then it flows through the ac-stage leading at the grid-side an output power P_{ac} even smaller because of the ac-power conversion losses $P_{ac,l}$. The typical connection of a two-stage FPC is shown in Fig. 2.1 (a), where the dc-stage is rated to process all the power deliver by the PV system. In that case, the dc-stage is only defined by the dc-dc converter, and the conversion efficiency of the stage η_{dc_s} depends on the dc-dc converter efficiency η_{dc_c}.

$$\eta_{dc_s} = \eta_{dc_c} = \frac{P_{dc}}{P_{dc} + P_{dc,l}} = \frac{P_{dc}}{P_{pv}} \tag{2.0.1}$$

Then, the ac-stage efficiency η_{ac_s} depends on the ac-power conversion losses.

$$\eta_{ac_s} = \frac{P_{ac}}{P_{ac} + P_{ac,l}} = \frac{P_{ac}}{P_{dc}} \tag{2.0.2}$$

Relating the two-stages, the global power conversion efficiency of the PV system η_t is defined.

$$\eta_t = \frac{P_{ac}}{P_{pv}} = \eta_{dc_s} \eta_{ac_s} \tag{2.0.3}$$

It means that the total power conversion efficiency depends on the individual power conversion stages. That is the main drawback working with two-stages PV applications, so that even when the ac-stage and the dc-stage reach a high efficiency, the global conversion efficiency will be lower than any of them.
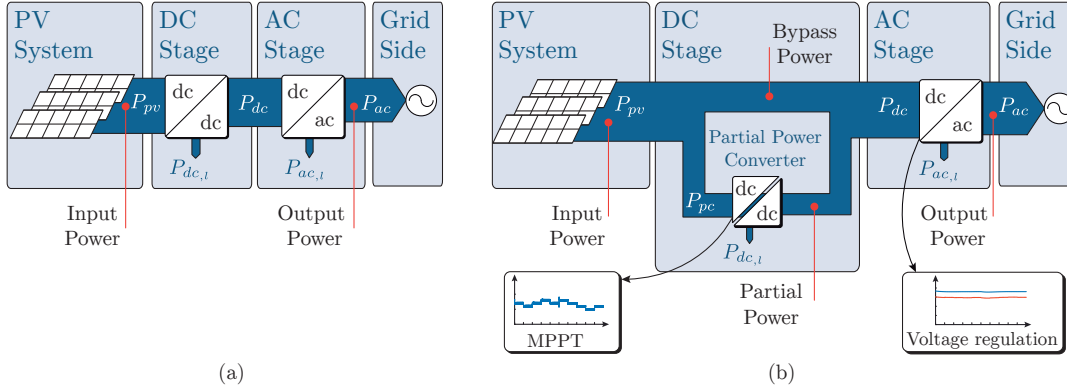
Figure 2.1: Power flow of a two-stage PV system. (a) Working with a full power converter. (b) Working with a partial power converter.

Traditionally in PV system the ac-stage reaches higher efficiencies than the dc-stage [27]. It can be even more significant working with microinverter applications or small-scale PV systems, so that is mandatory to elevate the voltage for the grid-connection. It leads to higher dc-conversion losses because of the magnetic components and high switching frequencies.

2.1 Partial Power Conversion

Among the solutions to increase the global conversion efficiency, one of them is focused on the reduction of the power processed by the conversion stage, and provide a direct path for the power flowing to the following stage [28]. This concept is known as partial power conversion and it is characterized for the power splitting, directing the power into two power paths as depicted in Fig. 2.1 (b). The dc-stage conversion efficiency η_{dc_s}, is increased if one of the paths has a higher efficiency. The operation principle is based on the power biasing, establishing a series path between the input and output side. In that case, the power handled by the converter is reduced, leading to a reduction of the conversion losses $P_{dc,l}$ in the dc-stage.

$$\eta_{dc_s} = \frac{P_{dc}}{P_{pv}} = \frac{P_{pv} - P_{pc}}{P_{pv}} + \frac{P_{pc}}{P_{pv}}\eta_{dc_c} \tag{2.1.1}$$

Simplifying the expression, the dc-stage efficiency is expressed as:

$$\eta_{dc_s} = 1 - \frac{P_{pc}}{P_{pv}}(1 - \eta_{dc_c}) \tag{2.1.2}$$

As can be seen from (2.1.2), the dc-stage efficiency does not depend only of the dc-dc converter efficiency η_{dc_c}, but also it is affected by the ratio of the power processed by the dc-stage P_{pc}/P_{pv}. This ratio is a parameter defined as *partial power ratio* K_{pr}, and it has the following features:

- A dc-dc converter works as partial power converter whereas the parameter $K_{pr} < 1$.

- The dc-stage efficiency η_{dc_s} increase when partial power ratio K_{pr} decreases.

- The partial power ratio K_{pr} only impacts over the dc-stage efficiency η_{dc_s}, whether the dc-dc converter efficiency is different than the unity $\eta_{dc_c} \neq 1$.

Then the dc-stage conversion efficiency can be expressed as:

$$\eta_{dc_s} = 1 - K_{pr}(1 - \eta_{dc_c}) \tag{2.1.3}$$

The theoretical efficiencies in a two-stage full power converter and partial power converter are depicted in the Fig. 2.2. Working with a PPC the efficiency of the dc-stage η_{dc_s}, varies depending on the partial power ratio K_{pr} (2.1.3). If the converter is designed to work with the half of the rated power $K_{pr} = 50\%$ and it has en efficiency $\eta_{dc_c} = 60\%$, the efficiency of the dc-stage $\eta_{dc_s} = 80\%$ as depicted in Fig. 2.2 (a). It means that the dc-stage efficiency increases 20% at this condition.

Moreover, the global conversion efficiency η_t also depends on the ac-stage conversion efficiency η_{ac_s}, as expressed in (2.0.3). In the case of a FPC, the result is depicted in Fig. 2.2 (b). If the dc-dc converter efficiency is $\eta_{dc_c} = 50\%$ (in that case is the same as the dc-stage efficiency η_{dc_s}), and the ac-stage efficiency is $\eta_{ac_s} = 60\%$, then the global efficiency is $\eta_t = 30\%$. It means that the total efficiency is even lower than the lower efficiency stage.

On the other hand, the same analysis is made for the PPC to contrast with the FPC. When the dc-dc converter is sized to the half of the rated power $K_{pr} = 50\%$, as depicted in Fig. 2.2 (c), the global conversion efficiency increases. If the dc-dc converter efficiency is $\eta_{dc_c} = 50\%$, and the ac-stage efficiency is $\eta_{ac_s} = 60\%$, then the global efficiency is $\eta_t = 45\%$. It means that the total efficiency increases 15% compared with the FPC.

The global conversion efficiency η_t increases if the partial power ratio K_{pr} decreases. As depicted in Fig. 2.2 (d), when the dc-dc converter is sized to handle 25% of the rated power $K_{pr} = 25\%$. If the dc-dc converter efficiency is $\eta_{dc_c} = 50\%$, and the ac-stage efficiency is $\eta_{ac_s} = 60\%$, then the global efficiency
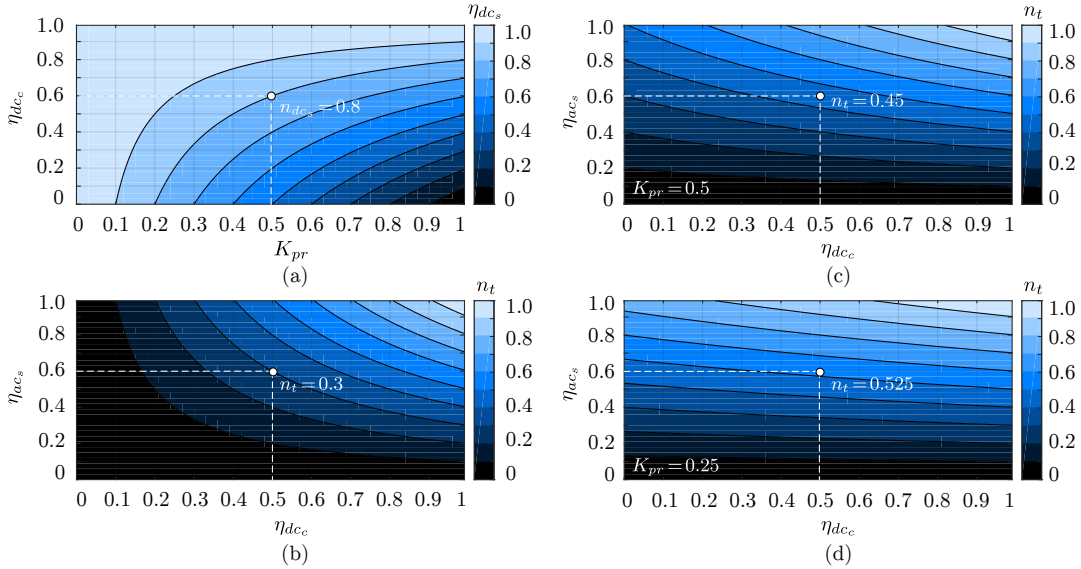
Figure 2.2: (a) Dc-stage efficiency η_{dc_s} in a PPC in terms of the partial power ratio K_{pr}. Global conversion efficiency η_t: (b) Working with a FPC. (c) Working with a PPC and $K_{pr} = 0.5$. (d) Working with a PPC and $K_{pr} = 0.25$.

is $\eta_t = 52.5\%$. It means that the total efficiency increases 22.5% compared with the FPC, and 7.5% compared with the PPC sized for handling the half of the rated power.

In general terms it is possible to realize the increased conversion efficiency by working with a PPC configuration. Moreover, it is directly associated to the power ratio handled by the converter, which can allows the reduction of the converter size.

2.1.1 Volume and power density analysis

The power conversion efficiency of the dc-stage, the volume and the power density are related with the power reduction in the dc-dc converter. The simplest approach to consider a power electronic system is modeling as a cube [29], where the power losses are dissipated by the surface area A_c which scales with the volume V of the cube as $A_c = 6V^{2/3}$, as depicted in Fig. 2.3.

Considering the dc-dc converter losses P_{dc_l}, the efficiency of the dc-dc converter η_{dc_c} in a FPC (2.0.1), can be written as:

$$\eta_{dc_c} = \frac{P_{pv} - P_{dc,l}}{P_{pv}} \tag{2.1.4}$$
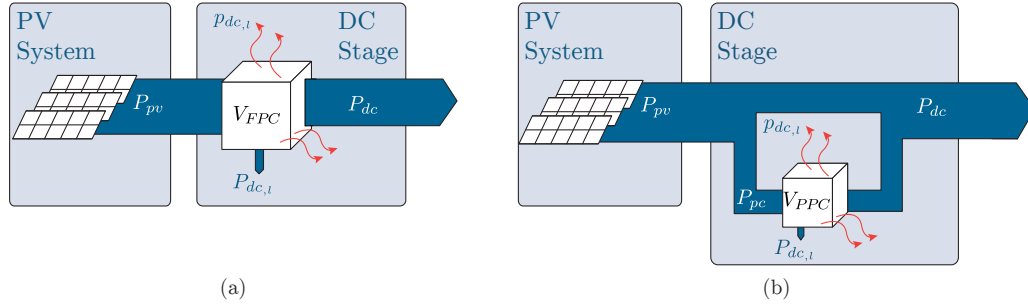
Figure 2.3: Volume of the dc-dc converter. (a) Working with a full power converter. (b) Working with a partial power converter.

Rearranging the equation, the power losses $P_{dc,l}$ working with a FPC are expressed as:

$$P_{dc,l} = P_{pv}(1 - \eta_{dc_c}) \tag{2.1.5}$$

The power losses can only be dissipated as heat over the surface area of the converter A_c, then the power losses dissipation $p_{dc,l}$ in the FPC are:

$$p_{dc,l} = \frac{P_{dc,l}}{A_c} = \frac{P_{pv}(1 - \eta_{dc_c})}{6V_{FPC}^{2/3}} \tag{2.1.6}$$

On the other hand, the power losses dissipation $p_{dc,l}$ in the PPC are:

$$p_{dc,l} = \frac{P_{dc,l}}{A_c} = \frac{P_{pc}(1 - \eta_{dc_c})}{6V_{PPC}^{2/3}} \tag{2.1.7}$$

In order to keep the identical design of the converter, holding the same dc-dc converter efficiency, the power losses dissipation $p_{dc,l}$ is considered as equal for both configurations. Then:

$$\frac{P_{pv}(1 - \eta_{dc_c})}{6V_{FPC}^{2/3}} = \frac{P_{pc}(1 - \eta_{dc_c})}{6V_{PPC}^{2/3}} \tag{2.1.8}$$

$$\frac{P_{pc}}{P_{pv}} = \frac{(1 - \eta_{dc_c})}{(1 - \eta_{dc_c})} \left(\frac{V_{PPC}}{V_{FPC}}\right)^{2/3} \tag{2.1.9}$$

Finally, it is possible to relate the volume variation V_{PPC}/V_{FPC} when the power processed by the converter K_{pr} changes. The equation is expressed as follows:

$$\frac{V_{PPC}}{V_{FPC}} = K_{pr}^{3/2} \qquad (2.1.10)$$

The result of the volume variation is depicted in Fig. 2.4 (a). It is possible to notice that the volume variation does not follow a linear trend as depicted with the dotted line. In fact, by considering the point A, if the converter is sized to handle $K_{pr} = 45\%$ of the rated power, the volume of the partial power converter is $V_{PPC} \simeq 30\% V_{FPC}$. Thus, the volume of the converter can be greatly reduced by reducing the power handled by the converter.

Moreover, the power density of the converter (ρ_{FPC}, ρ_{PPC}) is directly related with the power processed per unity of volume as:

$$\rho_{FPC} = \frac{P_{pv}}{V_{FPC}} \qquad (2.1.11)$$

$$\rho_{PPC} = \frac{P_c}{V_{PPC}} \qquad (2.1.12)$$

Using (2.1.9) in (2.1.12), the PPC power density ρ_{PPC} is expressed as:

$$\rho_{PPC} = \frac{P_c}{\left(\frac{P_c}{P_{pv}}\right)^{3/2} V_{FPC}} \qquad (2.1.13)$$

$$\rho_{PPC} = \frac{P_{pv}}{V_{FPC}} \left(\frac{P_{pv}}{P_c}\right)^{1/2} \qquad (2.1.14)$$

Using (2.1.11) in (2.1.14),

$$\rho_{PPC} = \rho_{FPC} \left(\frac{P_c}{P_{pv}}\right)^{-1/2} \qquad (2.1.15)$$

The relation between the power density working with the PPC and FPC is expressed in terms of the partial power ratio K_{pr} as:

$$\frac{\rho_{PPC}}{\rho_{FPC}} = K_{pr}^{-1/2} \qquad (2.1.16)$$

As is depicted in the Fig. 2.4 (b), the power density increases with the reduction of the power processed by the converter. Considering the point B in the solid line, the converter is sized to handle $K_{pr} = 40\%$ of the rated power, the density of the partial power converter is $\rho_{PPC} \simeq 1.58 \rho_{FPC}$.
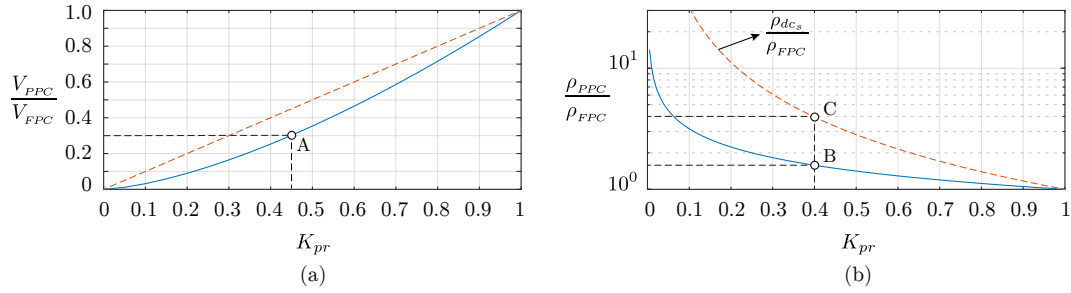
Figure 2.4: (a) Volume variation related with the partial power ratio. (b) Power density variation related with the partial power ratio.

However, the dc-stage is composed by the power processed by the converter and the bypass power, then the density of the dc-stage ρ_{dc_s} related with the FPC density ρ_{FPC} is expressed as:

$$\frac{\rho_{dc_s}}{\rho_{FPC}} = K_{pr}^{-3/2} \tag{2.1.17}$$

As is illustrated with the dotted line in the Fig. 2.4 (b), the power density highly increases with the reduction of the power processed by the converter. Considering the point C, the converter is sized to handle $K_{pr} = 40\%$ of the rated power and the density of the dc-stage is $\rho_{dc_s} \simeq 3.95\rho_{FPC}$.

The partial power processing technique allows a reduction of the converter volume, also increasing the power density. It does not depend of the converter topology, and compared with a traditional FPC , the cost could decrease because of the smaller rated semiconductors and smaller heat-sinks.

2.1.2 Review of existing partial power converter applications

The Partial Power Converter (PPC) concept has been around in other applications such as wind turbines, by using a doubly fed induction generator with an indirect four quadrant ac-dc-ac converter connected between the rotor windings [30] and the grid, and an additional direct grid connection to the stator. In this case the converter is only rated at 30% of the wind turbine power; yet it provides enough control range to perform variable speed operation and maximum power point tracking.

The same concept of handle only a portion of the total power also was expanded to the PV systems in order to curtail the power loss inherent in the two-stage configurations and improve the conversion efficiency [25]. Then, the concept was expanded and depending on the connection used for the PPC some
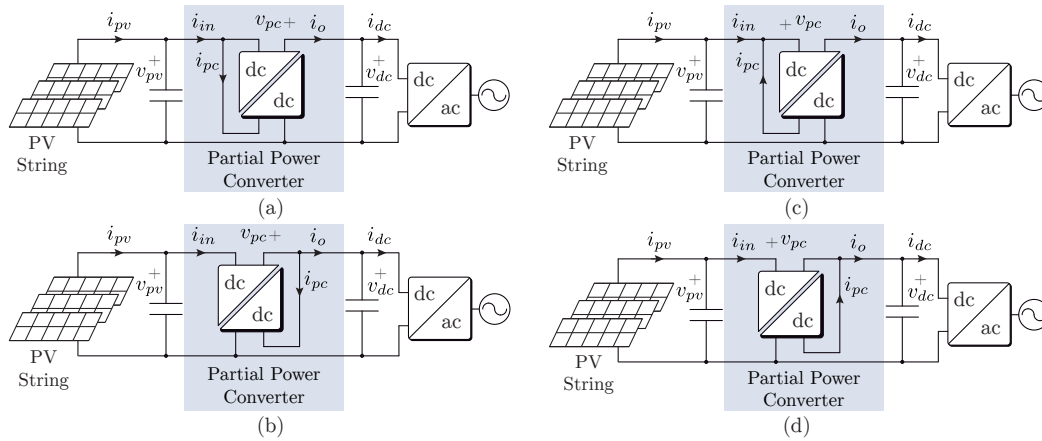
Figure 2.5: PPC configurations for two-stage PV applications. (a) Step-up converter, connection at the PV system (Step-Up I). (b) Step-up converter, connection at the the dc-link (Step-Up II). (c) Step-down converter, connection at the PV system (Step-Down I). (d) Step-down converter, connection to the dc-link (Step-Down II).

different applications were derived.

As was explained before, the configurations are based on a series voltage connection, and it can be made by using traditional isolated dc-dc topologies connected as depicted in Fig. 2.5. The PPC configuration based on the connection shown in the Fig. 2.5 (a), where a step-up operation is obtained, was introduced for a spacecraft application in order to improve the performance compared with the traditional boost converter [31]. In that work the configuration is named as series connected boost unit (SCBU), and voltage elevation is obtained because of the specific interconnection scheme. Other applications based on the same series connection are found in [32] and [33], where a $25kW$ prototype was developed. The topology chosen for the experiment was a series interconnection of four Full-bridge converters, designed to handle 30.7% of the rated power and achieving an efficiency around 96% working at $33kHz$. In [34], a Buck-Boost PPC was proposed for a $30W$ prototype. In that work the chosen topology is a Flyback converter, and the contribution of the work is the Full-bridge converter connected at the output side which changes the voltage regulation, achieving the buck-boost operation. However, for a PV application the solution is not suitable because of the reverse current obtained when the converter works in Buck operation. Among other applications, it is possible to find in [35], [36], [37], [38] the especial interest focused on the use of PPC for microinverter application. They present an improvement in the conversion efficiency,

which is commonly a problem compared with other traditional PV application due to the high voltage elevation required for the grid-connection. In [39], a non-isolated topology is used to operate as a PPC. The main advantage is the absence of a transformer to make the connection, and despite of the Buck-Boost topology the output voltage is always greater than the input voltage. Due to the absence of a transformer, the converter is not suitable for applications where a high voltage elevation is required.

It is also possible to achieve a step-up operation using the connection shown in the Fig. 2.5 (b). In [40], the PPC is named as a PV balancer so that the converter is used to compensate the voltage differences due to changes in the solar irradiation. The converter works with a Flyback topology and it reaches an experimental efficiency between around 89% ∼ 97%. The focus of [40] is the small size of the partial power converter due to the reduced power handled, and it proposes to use the converter as a replacement of the junction box of a PV module. However, the configuration has limitations on the voltage elevation as is explained in [41], where the maximum gain must be less than the double of the input voltage. Another application is found in [42], where an isolated Ćuk topology is implemented into a powered electric aircraft. The converter is rated for 26% of the $2.7kW$ generated power and it achieves an experimental efficiency above 95%.

Even though PPCs have been presented in the past, they have been focused on voltage boost operation. However, PV systems with large strings also require a voltage reduction. Then, based on the connection shown in the Fig. 2.5 (c) and (d), it is possible to create a PPC configuration working with a step-down operation. The first connection using the concept of voltage reduction was presented in [43], where the system is mainly used to charge a battery from a PV array, reaching high efficiencies due to the reduced power flowing trough the converter. However, these configurations have not yet been explored for PV applications, thus this is also one of the focus presented in this work.

As can be noticed, these configurations have received several names over the years, including Partial Capacity Converter, Partial Power Processing Converters, Series Voltage Compensation and PV Balancers. However, in essence the operating principle is to connect a series voltage between the PV system and the inverter's dc-link, since this voltage is usually smaller that the other two, it will process less power. In addition, the PPC is used to control indirectly the PV system output voltage to ensure MPPT. Therefore, among the different nomenclatures the name Partial power converter has been adopted in this work.
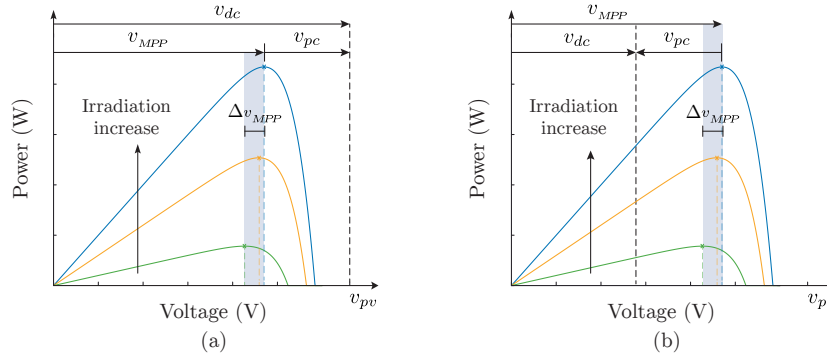
Figure 2.6: Operation in a PV system. (a) Positive series connections (step-up operation). (b) Negative series connection (step-down operation).

2.2   Classification of Partial Power Converters

Based on the different PPC configurations presented above, it is possible to notice that the connection plays an important role on the converter operation. So that, the polarity of the compensated voltage by the partial power converter is chosen by the circuit connection, and it does not depend on the dc-dc topology. This connection can be implemented either: (a) adding voltage to the PV system to reach the dc-link voltage, or (b) subtracting voltage to the PV system until reach out the dc-link voltage required for the grid-connection. The first connection is useful for microinverters, string or multistring inverters with a small string voltage ($v_{pv} < v_{dc}$). The second connection is useful for string or multistring inverters with large strings ($v_{pv} > v_{dc}$). For both connections, the operating principles of MPPT regulation are shown in Fig. 2.6. Note that the amplitude of the compensated voltage v_{pc}, can be regulated to adjust the PV system voltage v_{pv} when the dc-link voltage v_{dc} remains fixed by the inverter control.

This work explores four dimensions of the partial power converters, which are summarized in the Fig. 2.7.

- The topology of the dc-dc converter, which can be made by using an isolated or non-isolated traditional dc-dc topology (Flyback, Full-bridge, Buck-Boost, etc).

- The PPC configuration, which is related to the series connected voltage, whether it is produced from the PV side or dc-link side connection. Other sort of connection can be made based on a floating cell used to balance the PV strings. However, it is neither evaluated nor analyzed, so that it
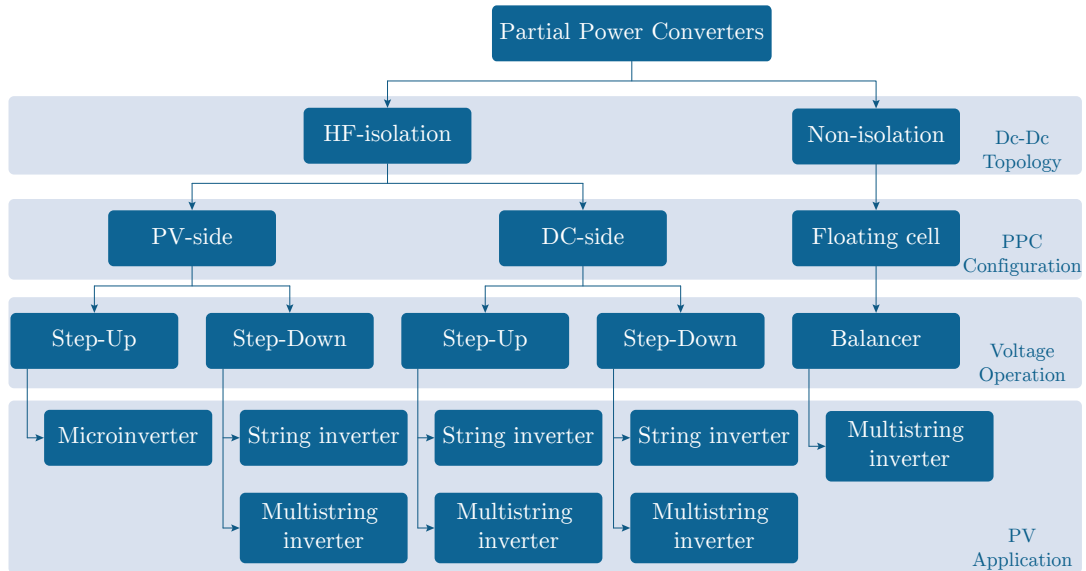
Figure 2.7: Classification of the PPC for the traditional PV application.

is out of the scope of the main contribution of the work. For more details on the subject, readers are invited to have a look on the references [44], [45].

- The voltage operation, which directly affects the PV system behavior leading to a step-up and step-down operation.

- Finally, the selection of the suitable application for the PV system, which is related with the type of configuration more than the topology.

2.3   Summary and Conclusion

From the investigation related with the partial power conversion approach, the most outstanding advantages are:

- *System conversion efficiency:* The dc-stage comprises two flowing paths, where one of them is highly efficient (direct power flow from the PV system to the ac-stage), and the another one flows trough the dc-dc converter which has a lower conversion efficiency. Then, the efficiency of the dc-stage increases whereas the power flowing through the dc-dc converter path is

reduced. It means that the ratio of the power processed by the converter determines the global conversion efficiency.

- *Volume reduction:* By the assumption that a power converter stage is a regular geometric body, and the process for designing is the same as a full power converter, the volume of the partial power converter can be reduced by reducing the power flowing through the dc-dc converter. Moreover, since components with lower current and voltage ratings can be employed, the economic cost of the converter prototype could also decrease.

- *Power density:* By considering that the density is calculated based on the power processed by the dc-dc converter per volume unit, the power density of the partial power converter increases by reducing the power flowing through the dc-dc converter. Moreover, considering that the dc-stage comprises not only the power processed by the PPC, but also the power flowing trough the direct path, it is possible to conclude that the power density of the dc-stage is highly increased compared with a traditional full power converter.

As can be realized, the advantages come from the reduction of the power handled by the dc-dc converter. However, the reduction leads some operation constraints, especially performing MPPT algorithm, which will be discussed in the following chapters of this work. Furthermore, after the entire review it is also possible to note that there are different PPC configurations used depending on the two-stage PV application. Even though the PPC has been in the focus of research for many years, there are still no general guidelines on how to select a suitable configuration for the different traditional PV applications.

Chapter 3

ISOLATED DC-DC TOPOLOGIES IN PARTIAL POWER CONVERTERS

This chapter discuss the isolation requirements in PPC configurations. Moreover, it analyzed the traditional isolated dc-dc topologies implemented in commercial PV applications, either microinverter or string inverters. In addition, the common undesirable effects by working with high-frequency isolated topologies as ringing effect, are also modeled and analyzed in this chapter. Finally, some solutions to mitigate this effect and experimental results will be given in order to validate the theoretical analysis.

3.1 Isolation requirement in PPC configurations

The dc-dc converter takes the power from the PV system and because of the connection, the series path also takes the power from the same PV system. Then, in order to avoid a short-circuit, the PPC configurations are made with isolated dc-dc topologies. In order to understand this requirement, the analysis is based on a generic structure of a non-isolated full power dc-dc converter as depicted in Fig. 3.1, where from a high-voltage input source v_{HV}, the power is regulated with a pair of semiconductors in order to get a low-voltage v_{LV} at output side. As was presented before, it is possible to create four PPC configurations as was depicted in Fig. 2.5. The connections of these four PPC configurations can be summarized into two cases:

When the PPC connection is made at the PV side (Step-Up I and Step-Down I PPCs), the generic case is shown in Fig. 3.2 (a). As can be seen, it is clear to note the conduction path which produces the short-circuit at the high-voltage side due to the connection between A-B.
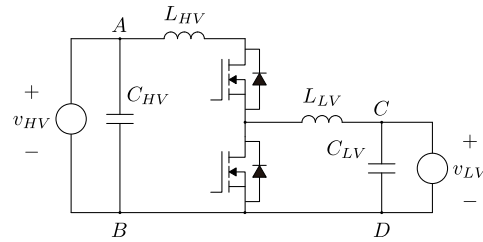
Figure 3.1: Generic structure of a non-isolated full power dc-dc converter.
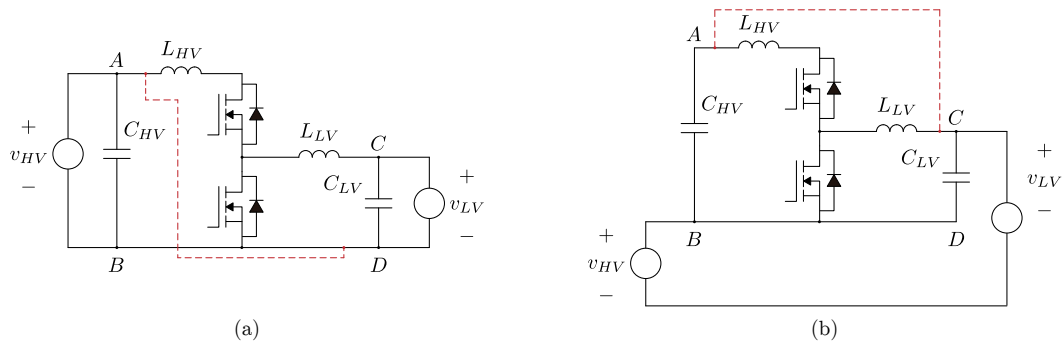
Figure 3.2: Possible connections of PPC configurations with non-isolated dc-dc converters.

On the other hand, when the PPC connection is made at the dc-side (Step-Up II and Step-Down II PPCs), the generic case is illustrated in Fig. 3.2 (b). As can be seen, it is clear to note that there is a conduction path composed by the series connection between the high-voltage source, the equivalent capacitor $(C_{HV} + C_{LV})$ and the low-voltage source. It means that the converter operation is useless so that there is not a voltage regulation, neither for the input nor the output voltage.

3.1.1 Traditional Isolated DC-DC Topologies

Flyback converter

The Flyback topology is commonly used in small power applications (20-200W) [46], and low voltage because of the simplest control. However, the active components of this topology have to support important over voltages due to the parasitic inductances of the transformer [47]. The voltage of the semiconductors which is in theory the sum of the voltage at the primary side and the voltage from the secondary side, is increased in a significant proportion. The
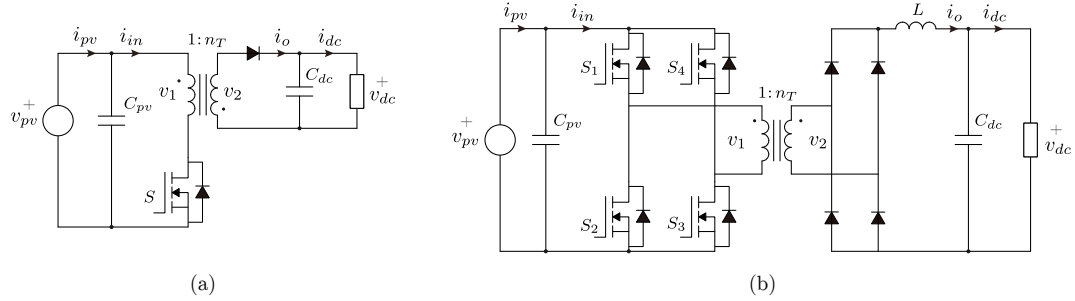
Figure 3.3: Traditional FPC. (a) Flyback topology. (b) Full-bridge topology.

topology is presented in Fig. 3.3 (a), and the principle of operation is explained by idealized waveforms of currents and voltages shown in Fig. 3.4. For more detailed information, the readers are invited to review the bibliography cited in this work.

Based on the operation in CCM in the Flyback converter, the transfer function of the voltage gain can be expressed as:

$$G_v = \frac{V_{dc}}{V_{pv}} = \frac{n_T d}{1 - d} \tag{3.1.1}$$

As can be seen, the converter presents a buck-boost operation mainly controlled by the duty cycle. Moreover, it is worth noticing that in contrast with a non-isolated topology, the transformer allows a voltage elevation changing the number of turns ratio. It is mainly helpful to design the converter for operating with a duty cycle around $d = 0.5$ for reducing the magnetic losses [48].

Full Bridge converter

The traditional Full-bridge dc-dc converter circuit is depicted in Fig. 3.3 (b). It is composed by a PWM inverter and a rectifier, which are galvanic isolated with a HF transformer. The advantage working with HF transformer is the size reduction of passive components. It will be discussed in detail in the following sections. The inverter consists of four power MOSFETs used as controllable switches, which are driven by non-overlapping voltages that are out of phase by π [rad]. The isolation transformer does not store energy, but its magnetizing inductance L_m must be larger enough to reduce the current through this inductance. On the other hand, if the magnetizing inductance increases, the transformer requires a larger number of turns which increase the physical size. The Full-bridge topology is suitable for high-power applications, usually from $0.5kW$ to several kilowatts. Compared with other traditional dc-dc topologies it
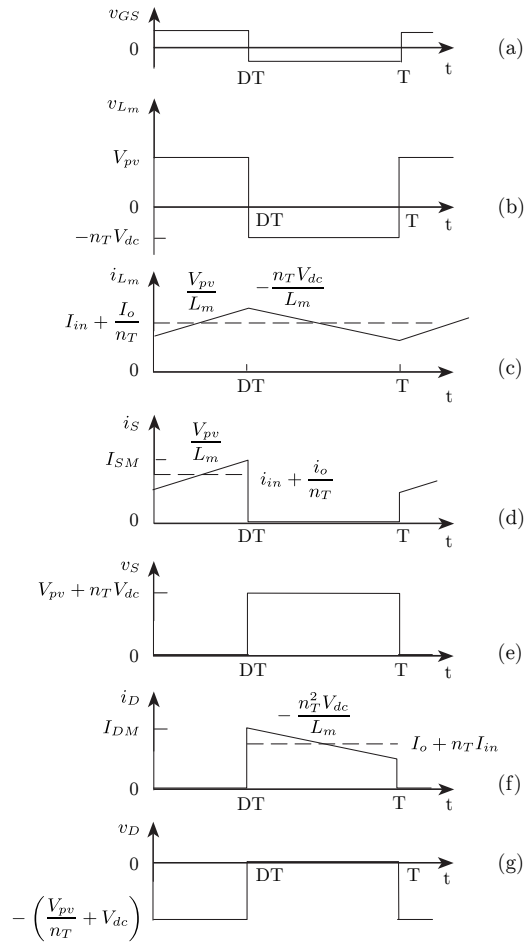
Figure 3.4: Idealized waveforms of currents and voltages in a Flyback topology. (a) Gate signal. (b) Voltage in the magnetizing inductance. (c) Current through the magnetizing inductance. (d) Current trough the MOSFET. (e) Voltage in the MOSFET. (f) Current trough the diode. (g) Voltage of the diode.

provides the highest power levels, and when the application power rate increases, the topology is commonly found the with parallel connection of MOSFETs. The principle of operation is explained by idealized waveforms of currents and voltages shown in Fig. 3.5. For more detailed information, the readers are invited to review the bibliography cited in this work.
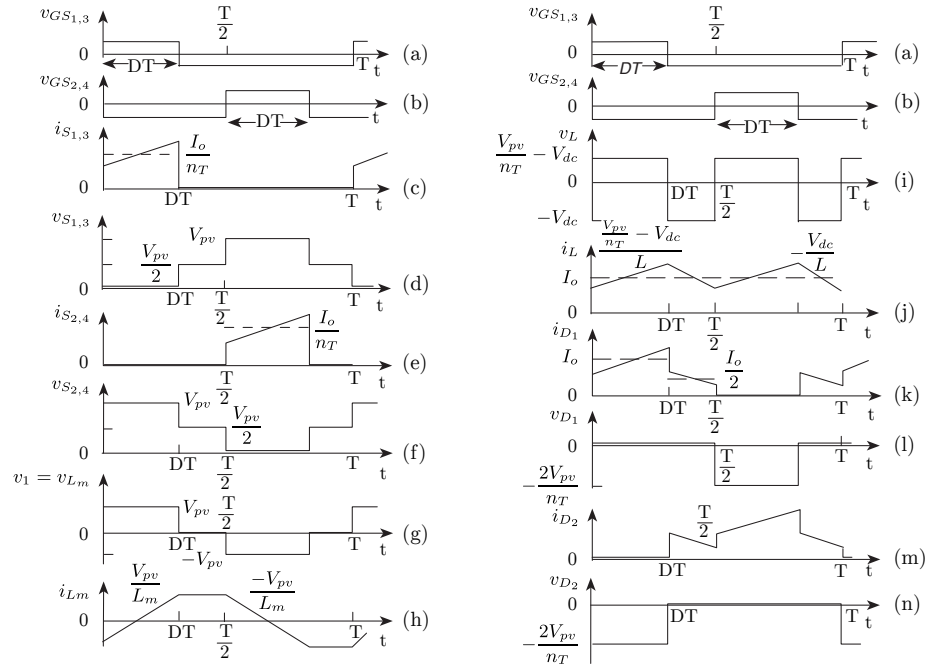
Figure 3.5: Idealized waveforms of currents and voltages in a Full-bridge topology. (a) Gate signals $S_{1,3}$. (b) Gate signals $S_{2,4}$. (c) Current through MOSFETs $S_{1,3}$. (d) Voltage of MOSFETs $S_{1,3}$. (e) Current through MOSFETs $S_{2,4}$. (f) Voltage of MOSFETs $S_{2,4}$. (g) Voltage of the magnetizing inductance. (h) Current trough the magnetizing inductance. (i) Voltage of the inductor filter. (j) Current trough the inductor filter. (k) Current through diode D_1. (l) Voltage of diode D_1. (m) Current through diode D_2. (n) Voltage of diode D_2.

3.1.2   High-frequency planar transformer model

Planar High Frequency (HF) transformers presented in Fig. 3.6, have become attractive in power electronics for applications in which both, power density and the geometry of the converter are important, such as PV microinverters, PC power supplies, etc. [49]. In order to achieve high power density supplies, the planar transformers are designed to work with high frequency power converters [50]. In PV applications, the interest on the use of planar technology begins with the high penetration of isolated dc-dc converters to adapt the low voltage range from a PV panel to the dc-bus required by the grid-tied inverter [5].

The research tends are directly toward to obtain the highest possible conversion efficiency, power density and reliability. The most common topologies used are based on the isolated dc-dc converters [51]. However, the behavior of the
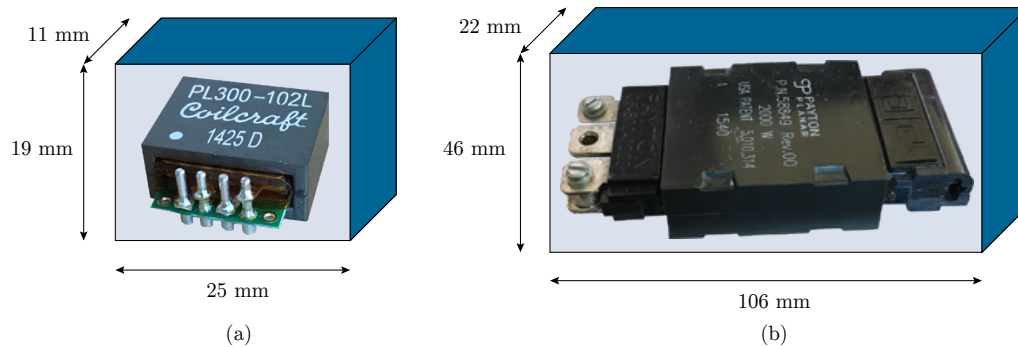
Figure 3.6: Planar transformers. (a) Coilcraft 300W. (b) PAYTON PLANAR 2000W.

transformer can not be precisely predicted by the conventional models, hence some methods have been proposed based on the geometry parameters and the parasitic electrical circuit [52].

Hard switching operation

The analysis presented in this section is made working with an isolated dc-dc Full-bridge converter as shown in Fig. 3.7. The switching performance affects the behavior of the HF power converters, which also influences on the conversion efficiency. Therefore, considerations in the selection of the power MOSFET and the design of the driver circuit, are important keys for better switching functionality. Besides, the physical location on the printed circuit board also affects its operation.

In power converters with synchronous switching configuration ($\bar{S}_a$ is the complementary signal of S_a), a ringing effect appears in the switching voltage node-(A) depicted in Fig. 3.7. It appears due to both, the resonances associated to the RLC loop formed by the parasitic elements (inductances, resistances and capacitors), and the reverse recovery of the body diode of the power MOSFET. Thus, to improve this inherent switching behavior two approaches can be considered. The first one consist on reducing the initial voltage peak of the ringing waveform to a non critical level related to the breakdown voltage of the MOSFET. The second approach consists on reducing the noise produced by the ringing oscillation. In this context, different design tips can be taken into account depending on which behavior is desired. Such as the design of PCB layout and snubber circuits (for minimize the resonance ringing oscillation), dead-time delays, turn-on and turn-off gate resistor configurations (to avoid the initial peak voltage of the total ringing waveform) [53], [54].
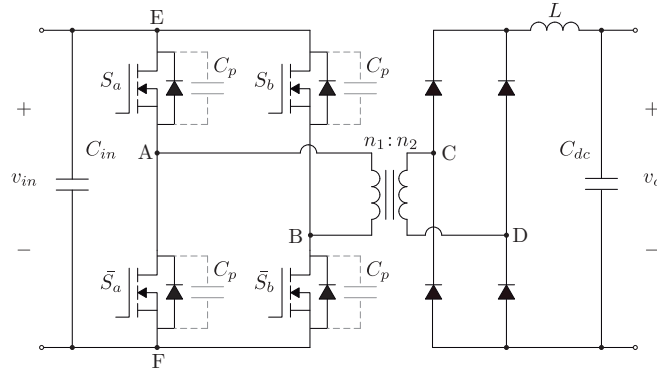
Figure 3.7: Isolated full bridge DC-DC topology showing parasitic capacitances.
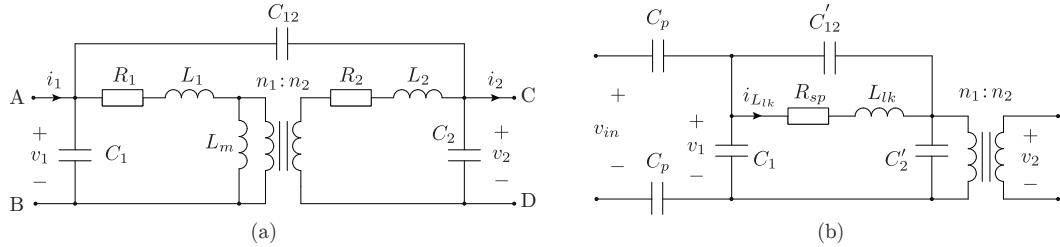
Figure 3.8: (a) Electrical circuit of the high-frequency transformer. (b) Simplified circuit model with the secondary elements reflected at the primary side.

Planar transformer model

The winding structure of a planar transformer can be modeled by an electrical circuit which considers its parasitic components [55]. As shown in Fig. 3.8 (a), the model is composed by an ideal transformer, a magnetizing inductance L_m, winding resistances R_1 and R_2, leakage inductances L_1 and L_2, intrawinding capacitances C_1 and C_2, and an interwinding capacitance C_{12}. The parasitic capacitances of the MOSFET C_p, also affect the behavior of the electrical circuit of Fig. 3.8 (a) hence, they must be considered in the model.

In order to simplify the electrical model considering only the parasitic components, a reduced electrical circuit reflected to primary side is presented, as illustrated in the Fig. 3.8 (b). Where, $R_{sp} = R_1 + n^2 R_2$, $L_{lk} = L_1 + n^2 L_2$, $C_2' = C_2/n^2$ and, $n_T = n_1/n_2$. It is possible to assume as a first instance that $C_{12}' = C_{12}$.

Depending on the input voltage v_{in}, the current $i_{L_{lk}}$ behaves as expressed in the equation:

$$\frac{I_{l_{lk}}}{V_{in}} = Ks\frac{w_o^2}{s^2 + 2\xi w_o s + w_o^2},\tag{3.1.2}$$

where $K = (C_2'C_p)/(2C_1 + 2C_2' + C_p)$.

Thus, the natural resonance frequency can be obtained from (3.1.2) which is expressed as,

$$\omega_o = \sqrt{\frac{2C_1 + 2C_2' + C_p}{L_{lk}(2C_1C_{12}' + 2C_1C_2' + 2C_{12}'C_2' + C_{12}'C_p + C_2'C_p)}},\tag{3.1.3}$$

and the expression for the damping ratio is,

$$\xi = \frac{0.5R_{sp}}{\sqrt{\dfrac{L_{lk}(2C_1 + 2C_2' + C_p)}{2C_1C_{12}' + 2C_1C_2' + 2C_{12}'C_2' + C_{12}'C_p + C_2'C_p}}}\tag{3.1.4}$$

By means of (3.1.3) and (3.1.4), its possible to calculate the parasitic effects on the converter behavior. It generates an oscillatory current, which leads to undesirable voltage effects.

3.1.3   Ringing effect, analysis and techniques to mitigate the effect

The operation of an isolated dc-dc converter is affected by the parasitic components of both, the HF transformer and power MOSFETs, combined with the fast turn-on time for the MOSFETs operation [56]. Due to the energy stored in the leakage inductance L_{lk}, a voltage spike and a superimposed ringing occur at the leading edge of the MOSFET voltage v_m at each transistor turn-off. It increases the voltage stresses and power loss resulting in a reduced conversion efficiency.

Analysis of the ringing effect

The current trough the leakage inductance L_{lk} presents a peak value $I_{L_{lkp}}$, and an oscillatory behavior which can be expressed as,

$$i_{L_{lk}}(t) = I_{L_{lkp}}e^{-\sigma t}\sin(w_d t) \tag{3.1.5a}$$

$$I_{L_{lkp}} = \frac{V_{in}Kw_o^2}{w_d} \tag{3.1.5b}$$

$$w_d = w_o\sqrt{1 - \xi^2} \tag{3.1.5c}$$

$$\sigma = \xi w_o \tag{3.1.5d}$$

The wave impedance Z_o of the electrical circuit leads to an oscillatory voltage, which can be expressed as,

$$v_{L_{lk}}(t) = Z_o I_{L_{lkp}}e^{-\sigma t}\cos(w_d t) \tag{3.1.6}$$

$$Z_o = w_o L_{lk} \tag{3.1.7}$$

The voltage obtained from (3.1.6) is added to the voltage in stationary state V_{in} hence, the MOSFET voltage v_m can be expressed as,

$$v_m = V_{in} + Z_o I_{L_{lkp}}e^{-\sigma t}\cos(w_d t), \tag{3.1.8}$$

where the peak voltage V_{mp} is,

$$V_{mp} = V_{in} + Z_o I_{L_{lkp}} \tag{3.1.9}$$

The energy stored in the leakage inductance before the MOSFET turns-off is expressed as,

$$W_{L_{lk}} = \frac{1}{2}L_{lk}I_{L_{lkp}}^2, \tag{3.1.10}$$

which results in power loss due to ringing depending on the switching frequency f_{sw},

$$P_{ring} = \frac{1}{2}L_{lk}I_{L_{lkp}}^2 f_{sw} \tag{3.1.11}$$

Considering the information shown before, it is possible to select a solution which can mitigate the ringing magnitude. They are based on, either passive snubber circuits or active clamping topologies, as presented in Fig. 3.9.
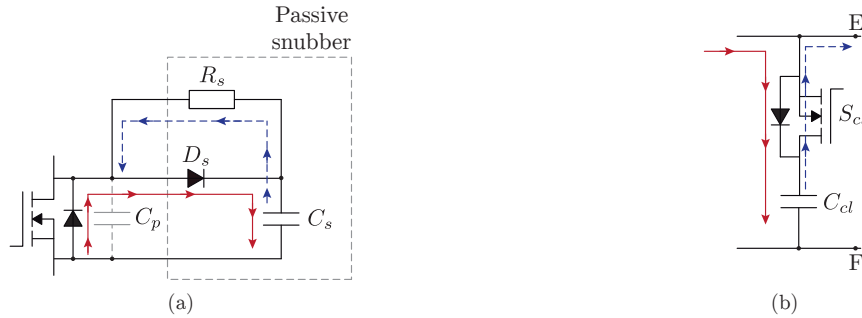
Figure 3.9: (a) Passive RCD snubber. (b) Active clamping circuit.

RCD snubber circuit

In order to reduce the ringing effect, the resistor-capacitor-diode (RCD) snubber circuit shown in Fig. 3.9 (a) is implemented, which is mainly used due to its simple design [57]. When the MOSFET turns-off, the stored energy in the leakage inductance flows trough the snubber diode D_s in order to charge the snubber capacitor C_s. When the MOSFET turns-on, the stored energy in the capacitor is dissipated trough the snubber resistance instead of the MOSFET. Therefore, it allows a reduction in the magnitude of ringing.

Some considerations related to the component sizing are: the stored energy in the leakage inductance $W_{L_{lk}}$, the snubber capacitor voltage which corresponds to the MOSFET voltage V_m, and the required time to dissipate the energy trough the snubber resistance, which is related with the switching period.

Active clamping circuit

The clamping circuit shown in Fig. 3.9 (b) is connected to the converter in order to improve the operation, and reduce the voltage overshoot during switching commutations [58]. It clamps the high voltage of switches when they are turned-off, and the capacitor C_{cl} absorbs the energy which can be regenerated by an active switch S_{cl}.

The conventional way to calculate the clamp capacitance is based on the resonant circuit formed between the clamp capacitor and the leakage inductance of the transformer. The resonance period must be greater than half of a switching period [59], and the loss of the clamp switch decreases according to the adequate clamp capacitance value. Therefore, the criteria to select a capacitor is expressed as:

Table 3.1: Experimental parameters of the planar transformer PAYTON PLA-
NAR 2000W.

Parameter	Value	Parameter	Value
V_{in}	37.0 V	C_p	257 pF
f_{sw}	50 kHz	C_s	0.1 μF
$n_1 : n_2$	3:24	R_{sp}	100 Ω
C_{12}	124.29 pF	C_{cl}	10 μF
R_2	7.51 Ω	L_2	4062.2 μH
L_1	63.01 μH		

$$C_{cl} \geq \frac{(T_s/4\pi)^2}{L_{lk}}, \tag{3.1.12}$$

where, T_s is the period of the driving signal per MOSFET, and L_{lk} is the
transformer leakage inductance reflected to the primary side.

Experimental results

A prototype of the converter is built, based on the topology shown in Fig. 3.7,
which is used to validate the previous theoretical analysis. Besides, the parasitic
components of the planar transformer are obtained using the Keysight-E5061B
Network Analyzer. As underlined in Fig. 3.10, the parameters chosen for the
model correspond to a switching frequency of $50kHz$. At this frequency, the
intrawinding capacitances C_1 and C_2, and the primary side winding resistor R_1
can be neglected. The experimental parameters of the planar transformer PAY-
TON PLANAR 2000W, and the parasitic components are listed in Table 3.1.
    In order to validate the presented model, the isolated dc-dc Full-bridge con-
verter works at hard-switching operation. Fig. 3.11 (a) shows the transformer
input voltage, where the ringing effect is observed. The figure shows the su-
perimposed overshoot and the oscillation presented in the waveform. The high-
frequency ringing at such high levels will affect transformer performances, and
may cause it to overheat. The conduction losses also increase because a MOS-
FET with higher break-down voltage and a higher on-resistance must be used.
    The theoretical results for the resonant frequency f_o and the peak voltage
across the MOSFET V_{mp} are $890.06kHz$ and $55.81V$, respectively. On the other
hand, the experimental results, corresponding to Fig. 3.11 (a), are $V_{mp} \approx 60V$
and $f_o \approx 893kHz$. Compared with the experimental results, the error is 0.31%
and 6.9% for f_o and V_{mp}, respectively. The reason of these differences, is because
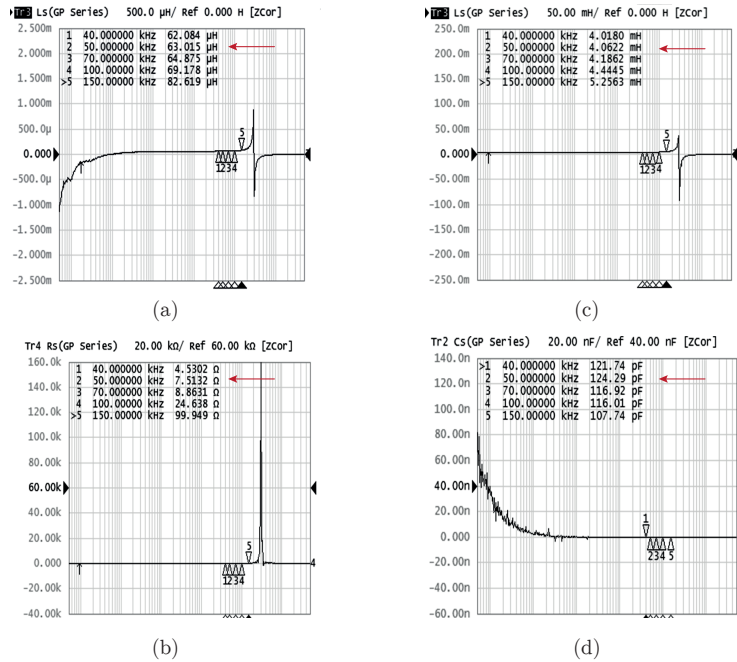
Figure 3.10: Experimental results of parasitic components in the planar transformer. (a) Leakage inductance L_1. (b) Secondary side winding resistance R_2. (c) Secondary side inductance L_2. (d) Interwinding capacitance C_{12}.
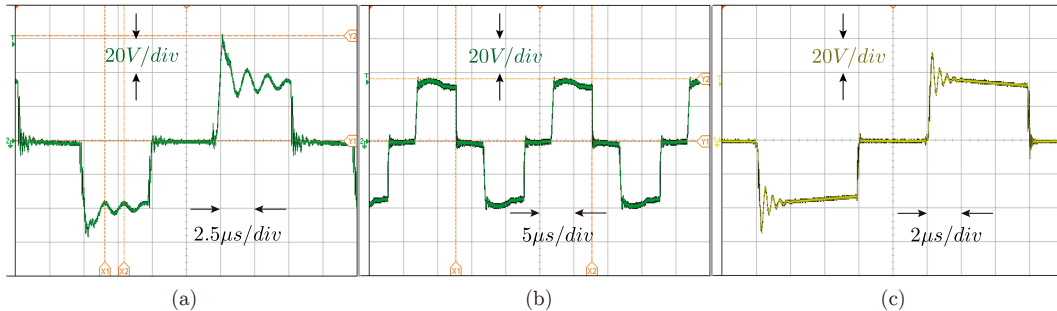
Figure 3.11: Experimental results of the transformer input voltage with: (a) Hard-switching operation. (b) RCD snubber circuit. (c) Active clamping circuit.

of the parasitic components related to the experimental Set-up and the PCB, which are not considered in the theoretical model.

Fig. 3.11 (b) shows the result using the RCD snubber circuit. It can be seen the reduction of the ringing amplitude, and the suppression of the oscillations. However, considering that the RCD snubber is a passive circuit, there are some

problems associated such as: the increase of the converter size for high power operations, and the lower efficiency compared with other solutions due to power dissipation trough the resistor.

Fig. 3.11 (c) shows the result using the active clamping circuit. It can be seen the attenuation of the oscillations, and the reduction of the ringing amplitude. Some solutions have been presented in the literature in order to achieve a better reduction of the resonance, which still remains in the waveform. They are not the central focus of the presented work, however some solutions can be found in [57], [58] and [59].

3.2   Summary and Conclusion

In this chapter it was discussed the isolation requirements in order to create the PPC configurations. It is important to note that the proposed PPC configurations require a transformer for the connection in order to obtain an isolated voltage for series connection between the PV system and the dc-link. It in reality will not provide effective galvanic isolation for the PV system. This might be seen as a drawback, but considering that the power rating of the converter is much lower than the total power, and high-frequency transformers are used, this is not a significant issue. Furthermore, the grounding of the PV system can be achieved by proper selection of the inverter stage and modulation, as with traditional transformer-less PV inverters [5].

In addition, the challenges related with the effect of parasitic components in the converters were discussed. Giving the focus around the effect of ringing, which is modeled, analyzed and some solutions are also presented, which will be considered for making the experimental test-benches.

Chapter 4

CLASSIFICATION OF PARTIAL POWER CONVERTERS

Depending on the scale of the photovoltaic system, the input source can be a single module, a string or an array. The amount of PV modules in series forming the string will define the operating voltage range. Hence, the dc-dc converter must control the input voltage to the desired MPPT voltage reference. Additionally, the dc-dc converter performs the conversion between the PV voltage and the inverter dc-link voltage. In a conventional PV system, usually the dc-link voltage is controlled by the grid-tied inverter to a value higher than the grid peak voltage. Therefore, depending on the PV source and the inverter requirements, the PV voltage must be either elevated or reduced by the dc-dc converter.

This chapter analyses and classifies the partial power converters, based on the possible connections made by the isolated dc-dc converter. Moreover, depending on the PV application, the voltage and power ratings can be very different, hence an appropriate topology selection should take advantage of each PPC configuration. In the literature it is possible to find a large number of isolated dc-dc converter topologies. However, the central scope of this work is not to evaluate all of them. Rather, the PPC configurations are analyzed depending on the type of PV application, and two mainstream dc-dc converter topologies are considered to be evaluated: the Flyback and the Full-bridge converters. All the mathematical analysis are made based on the assumption that the converters are designed to operate in continuous conduction mode (CCM).

4.1   Step-Up Partial Power Converters

In small scale PV applications, such as microinverters, the dc-dc stage is almost mandatory in order to elevate the voltage of a single PV module ($\approx 30V$) to the
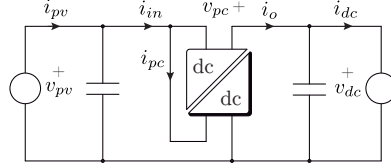
Figure 4.1: Step-Up PPC with partial connection at the PV-side (Step-Up I).

required dc-link voltage for grid-connection. Moreover, in string or multistring PV applications, the voltage elevation is a requirement when the PV voltage is not high enough for performing grid-connection, specially under partial shading conditions. In these cases, the PPC must compensate the difference adding voltage in the same polarity to the PV system until reach the dc-link voltage as depicted in Fig. 2.6 (a).

4.1.1   Step-Up I Partial Power Converter

The voltage elevation does not depend on the dc-dc topology, but it is achieved with the PPC connection. One possible solution is by the power splitting at the PV side as shown in Fig. 4.1.

Partial power ratio

In general terms, no matter the PPC configuration nor the isolated dc-dc topology, the voltage gain G_v of the dc-stage is expressed as:

$$G_v = \frac{V_{dc}}{V_{pv}} \tag{4.1.1}$$

Moreover, considering that the input and output capacitors losses are neglected, the dc-stage conversion efficiency η_{dc_s} is expressed as:

$$\eta_{dc_s} = \frac{V_{dc}I_o}{V_{pv}I_{in}} \tag{4.1.2}$$

Including (4.1.1) in (4.1.2), then the efficiency is expressed as:

$$\eta_{dc_s} = G_v \frac{I_o}{I_{in}} \tag{4.1.3}$$

By Kirchoff laws, the voltage and current shown in Fig. 4.1 are expressed as:

$$V_{dc} = V_{pv} + V_{pc} \tag{4.1.4}$$
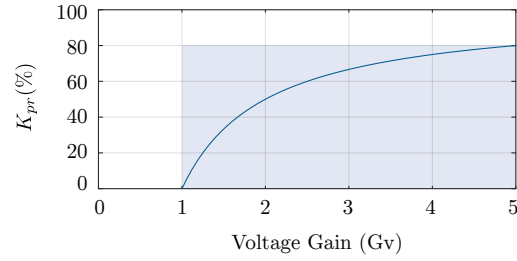
Figure 4.2: Partial power operation range of the Step-Up I PPC.

$$I_{in} = I_{pc} + I_o \tag{4.1.5}$$

In general terms, the partial power ratio K_{pr} is defined as:

$$K_{pr} = \frac{P_{pc}}{P_{pv}} \tag{4.1.6}$$

And, in order to define the operation region of the Step-Up I PPC, the partial power ratio K_{pr} is calculated as:

$$
\begin{aligned}
K_{pr} &= \frac{V_{pv} I_{pc}}{V_{pv} I_{in}} \\
K_{pr} &= \frac{I_{in} - I_o}{I_{in}} \\
K_{pr} &= 1 - \frac{I_o}{I_{in}}
\end{aligned}
\tag{4.1.7}
$$

In order to express the K_{pr} in terms of the dc-stage efficiency and voltage gain, (4.1.3) is included in (4.1.7) and the partial power ratio is finally defined as:

$$K_{pr} = 1 - \frac{\eta_{dc_s}}{G_v} \tag{4.1.8}$$

Considering that the dc-stage is highly efficiency $\eta_{dc_s} \approx 1$, the partial power ratio K_{pr} varies depending on the voltage gain G_v as illustrated in the Fig. 4.2. Where the shadowed area represents the region of partial power operation.

Analysis of topology

Commercial dc-dc converters for PV applications are based on traditional topologies. Among the criteria for the topology selection are: the complexity of the structure, the control technique, reliability and efficiency [5]. In this section the

Figure 4.3: Step-Up I Partial Power Converters. (a) Based on Flyback topology. (b) Based on Full-bridge topology.

two topologies used for the analysis are the Flyback and Full-bridge, because of the high applicability in the PV industry [60], [4].

This analysis is based on the operation range, it means that the converter must have the ability to elevate the voltage and work as a PPC within the duty cycle range $d = [0 - 1]$. Moreover, it is also analyzed the importance and dependence of the transformer turns ratio n_T in the operation range.

Working with a Flyback topology for the PPC configuration, and connecting as presented in Fig. 4.3 (a), the dc-dc converter voltage gain G_{vc} is calculated as:

$$G_{vc} = \frac{V_{pc}}{V_{pv}} = \frac{n_T d}{1 - d} \tag{4.1.9}$$

Applying (4.1.4), the equation can be expressed as:

$$\frac{V_{dc} - V_{pv}}{V_{pv}} = \frac{n_T d}{1 - d} \tag{4.1.10}$$

Rearranging and simplifying the expression, and also considering (4.1.1). Then the global voltage gain can be expressed as:

$$G_v = \frac{1 + d(n_T - 1)}{1 - d} \tag{4.1.11}$$

The voltage gain (4.1.11) depends on the duty cycle d, which is limited to [0-1], and the transformer turns ratio n_T. The operation range is depicted in Fig. 4.4 (a), where the shadowed area represents the region of partial power operation.

(a)

(b)

Figure 4.4: Operation range of the Step-Up I PPC for different transformer turns ratio n_T. (a) Based on Flyback topology. (b) Based on Full-bridge topology.

From this picture it is possible to see that using a Flyback topology for the PPC configuration, the converter operation is not limited by the voltage gain but the transformer turns ratio. For example, considering a small voltage gain (e.g $G_v < 2$), and a turns ratio $n_T = 8$, the duty cycle range is limited to $d = [0 - 0.11]$. It means that a high resolution in the control platform is needed to compensate the small variations, which is translated to a more expensive control design. Instead, with a transformer turns ratio $n_T = 1$, the duty cycle range increases to $d = [0 - 0.5]$ for the same application. The same analysis can be applied for higher voltage gains, where the best resolution is achieved by using a transformer with greater turns ratio.

Working with a Full-bridge topology for the PPC configuration, and connecting as depicted in Fig. 4.3 (b), the dc-dc converter voltage gain G_{vc} is calculated as:

$$G_{vc} = \frac{V_{pc}}{V_{pv}} = n_T(1 - d) \tag{4.1.12}$$

Applying (4.1.4), the equation can be expressed as:

$$\frac{V_{dc} - V_{pv}}{V_{pv}} = n_T(1 - d) \tag{4.1.13}$$

Rearranging and simplifying the expression, and also considering (4.1.1). Then the global voltage gain can be expressed as:

$$G_v = 1 + n_T(1 - d) \tag{4.1.14}$$

The voltage gain (4.1.14) depends on the duty cycle d and the transformer turns ratio n_T. The operation range is shown in Fig. 4.4 (b), where the shadowed area represents the region of partial power operation.

From this picture it is possible to see that with a Full-bridge there are even more limitations in terms of the operation range. The selection of the transformer turns ratio limits the maximum voltage gain. For example, considering a small voltage gain (e.g $G_v < 2$), it is only possible to use transformers with few turns ratio in order to avoid the requirement of working with control platforms with high resolutions. But the challenge design is more critical for applications with higher voltage gains, so that the operation can be only guaranteed with a selection of transformers with greater turns ratio.

For example, considering a voltage gain (e.g $G_v > 4$), it is only possible to use transformers with turns ratio higher than $n_T > 4$ to work within the operation range. However, selecting a turns ratio $n_T = 4$, the voltage gain is limited to a maximum value of $G_v = 5$ and the operation range is limited to a 25% ($d = [0 - 0.25]$). On the other hand, with a turns ratio $n_T = 5$ it is possible to reach a high voltage gain $G_v = 9$. Nevertheless, if the voltage gain is limited to the same value $G_v = 5$ chosen before, then the operation range is reduced to a 13% ($d = [0.5 - 0.63]$). It leads a trade-off between the voltage gain and the operation range, which mainly depends on the design of the PV application.

Discussion and commentaries

The global voltage gain is not only related to the converters considered in this analysis, they are also found in other traditional isolated dc-dc converters (Forward, Ćuk, Half-Bridge, etc.) [46]. However, the central focus of this work is not the selection of the optimal isolated dc-dc converter, but the same procedure of the analysis can be applied for other topologies found in the literature.

A typical PV application where voltage elevation is required is the microinverters. These PV applications require a high voltage step-up ratio, since they are used for a single PV module ($\approx$30V) [61]. Moreover, the nominal power for some commercial PV modules are found around $300W$. Therefore, the Step-Up I PPC shown in Fig. 4.3 (a) is the most appropriate option for this application, since the partial power operation is not limited by the voltage gain. Besides, regarding with the topology selection the traditional Flyback converter is chosen not only due to its simple structure, but also because its operation features. The same advantages of an interleaved operation with two dc-dc converters can be obtained with a single PPC choosing appropriate parameters. This is further discussed in the Chapters 6 and 7.

As an example, some feasible parameters for one PV module are an input voltage $V_{pv} = 30V$, with a single-phase inverter and a dc-link voltage of $V_{dc} = 180V$, used for a grid connection of $V_g = 110V_{rms}$, a possible solution is to
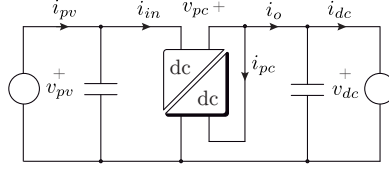
Figure 4.5: Step-Up PPC with partial connection at the dc-link side (Step-Up II).

select a transformer with $n_T = 5$ turn ratio in order to work with a duty cycle around $d = 0.5$ reducing the magnetic losses [48]. In that case, the partial ratio varies around $K_{pr} \approx 83\%$, which means that the converter power rating can be reduced around $\sim 17\%$. This result can be improved using different techniques and connections of the PPCs, for example with input-parallel output-series (IPOS) connections, which will lead in a reduction of the voltage gain.

4.1.2   Step-Up II Partial Power Converter

Another option to achieve a voltage elevation is through the PPC configuration illustrated in Fig. 4.5, where the power splitting is made at the dc-side.

Partial power ratio

Based on the circuit connection presented in Fig. 4.5, the voltage and current are expressed as:

$$V_{dc} = V_{pv} + V_{pc} \tag{4.1.15}$$

$$I_{in} = I_{pc} + I_o \tag{4.1.16}$$

In order to define the operation region of the Step-Up II PPC, the partial power ratio K_{pr} (4.1.6), is calculated as:

$$
\begin{aligned}
K_{pr} &= \frac{V_{dc} I_{pc}}{V_{pv} I_{in}} \\
K_{pr} &= \frac{V_{dc}(I_{in} - I_o)}{V_{pv} I_{in}} \\
K_{pr} &= \frac{V_{dc}}{V_{pv}} - \frac{V_{dc} I_o}{V_{pv} I_{in}}
\end{aligned}
\tag{4.1.17}
$$

In order to express the K_{pr} in terms of the dc-stage efficiency and voltage gain, (4.1.3) is included in (4.1.17) and the partial power ratio is finally defined as:

$$K_{pr} = G_v - \eta_{dc_s} \tag{4.1.18}$$

Figure 4.6: Partial power operation range of the Step-Up II PPC.
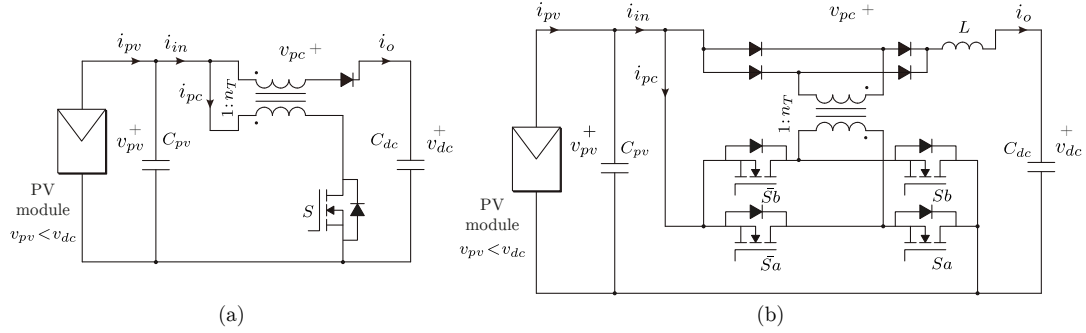

(a)   (b)
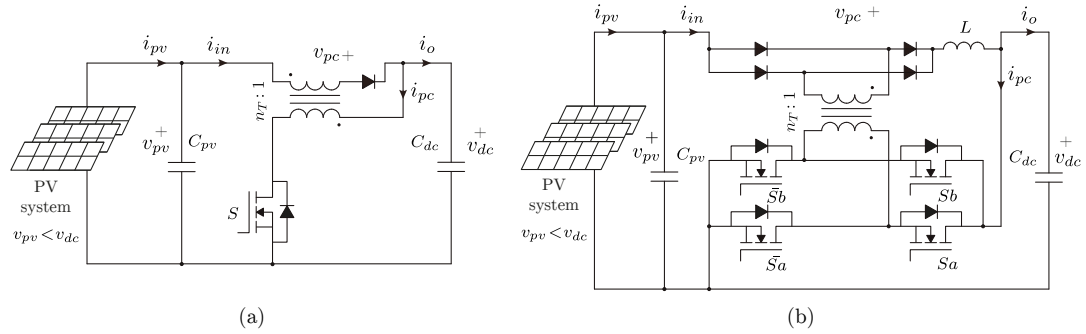
Figure 4.7: Step-Up II Partial Power Converters. (a) Based on Flyback topology. (b) Based on Full-bridge topology.

Considering that the dc-stage is highly efficiency $\eta_{dc_s} \approx 1$, the partial power ratio K_{pr} varies depending on the voltage gain G_v as depicted in the Fig. 4.6. Where the shadowed area represents the region of partial power operation. Notice that in contrast with the Step-Up I PPC configuration, this partial ratio is limited by the voltage gain. As can be seen in the figure the maximum value is limited to the double of the input voltage. This limitation does not allow the use of this configuration in PV applications as microinverters, where the input voltage must be highly elevated.

Analysis of topology

Working with a Flyback topology for the PPC configuration, and connecting as shown in Fig. 4.7 (a), the dc-dc converter voltage gain G_{vc} is calculated as:

$$G_{vc} = \frac{V_{pc}}{V_{dc}} = \frac{d}{n_T(1-d)} \qquad (4.1.19)$$
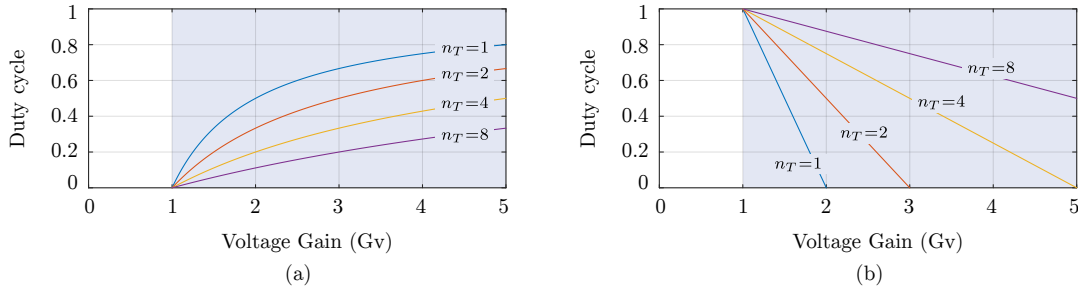
(a)

(b)
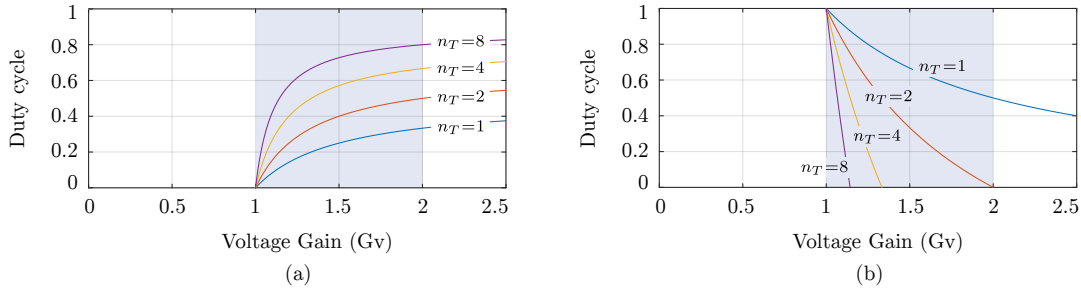
Figure 4.8: Operation range of the Step-Up II PPC for different transformer turns ratio n_T. (a) Based on Flyback topology. (b) Based on Full-bridge topology.

Applying (4.1.15), the equation can be expressed as:

$$\frac{V_{dc} - V_{pv}}{V_{dc}} = \frac{d}{n_T(1 - d)} \tag{4.1.20}$$

Rearranging and simplifying the expression, and also considering (4.1.1). Then the global voltage gain can be expressed as:

$$G_v = \frac{n_T(1 - d)}{n_T(1 - d) - d} \tag{4.1.21}$$

The voltage gain (4.1.21) depends on the duty cycle d, which is limited to [0-1], and the transformer turns ratio n_T. The operation range is illustrated in Fig. 4.8 (a), where the shadowed area represents the region of partial power operation.

From this picture it is possible to see that using a Flyback topology for the PPC configuration, the converter operation is neither limited by the voltage gain, nor the transformer turns ratio. However, depending on the design considerations, assuming a operation around the duty cycle $d = 0.5$, a solution can be to design a transformer with $n_T = 3$ for a partial power ratio $K_{pr} = 50\%$.

Working with a Full-bridge topology for the PPC configuration, and connecting as presented in Fig. 4.7 (b), the dc-dc converter voltage gain G_{vc} is calculated as:

$$G_{vc} = \frac{V_{pc}}{V_{dc}} = \frac{(1 - d)}{n_T} \tag{4.1.22}$$

Applying (4.1.15), the equation can be expressed as:

$$\frac{V_{dc} - V_{pv}}{V_{dc}} = \frac{(1 - d)}{n_T} \tag{4.1.23}$$

Rearranging and simplifying the expression, and also considering (4.1.1). Then the global voltage gain can be expressed as:

$$G_v = \frac{n_T}{n_T - 1 + d} \tag{4.1.24}$$

The voltage gain (4.1.24) depends on the duty cycle d and the transformer turns ratio n_T. The operation range is depicted in Fig. 4.8 (b), where the shadowed area represents the region of partial power operation.

From this picture it is possible to see that working with a Full-bridge the voltage gain is limited by the turns ratio selection. Nevertheless, with a transformer turns ratio $n_T = 2$, the complete partial power operation range is fulfilled.

For example, considering a voltage gain (e.g $G_v < 1.5$), it is only possible to use transformers with turns ratio fewer than $n_T < 2$ to work within the whole operation range. However, selecting a turns ratio $n_T = 1$, the operation range is limited to a 33% ($d = [0.67 - 1.0]$). On the other hand, with a turns ratio $n_T = 2$ it is possible to increase the operation range to 67% ($d = [0.33 - 1.0]$), which is translated to a more flexible control platform requirements.

Discussion and commentaries

Commonly in string and multistring inverters, the voltage elevation gain is not the main limitation due to the flexibility to connect in series the PV modules. Moreover, when the PV system is designed with a voltage elevation $G_v < 2$, the Step-Up II PPC becomes an alternate solution due to the use of the operation range. However, considering that the string and multistring inverters, are commonly used for medium power applications ($P_{pv} > 1kW$), the Flyback topology is not a practical solution. The main disadvantages come from the less efficiently use of the core, and the higher voltage stress on the switch during the turn-off operation [46]. For that reasons the isolated Full-bridge topologies become the most practical solution reaching higher efficiencies in high power applications.

As an example using a Full-bridge topology, some feasible parameters for a PV string are a series connection made with 8 PV modules $V_{pv} = 240V$, and a single phase inverter $V_{dc} = 360V$ for a grid of $V_g = 220V_{rms}$, the voltage gain is $G_v = 1.5$. It is possible to see that the maximum duty cycle range is not limited when a transformer with $n_T = 3$ is used. In that case, the partial ratio varies around $K_{pr} \approx 50\%$, which means that the converter power rating can be reduced around $\sim 50\%$. But it does not limit to include more PV modules connected in series with a higher transformer turns ratio, in order to reduced the partial power ratio.
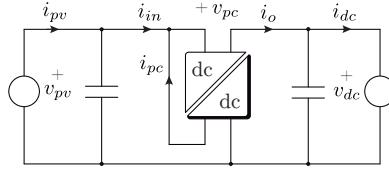
Figure 4.9: Step-Down PPC with partial connection at the PV-side (Step-Down I).

4.2 Step-Down Partial Power Converters

In large-scale solar systems the PV modules are connected forming an array. It is common to find larger strings to reach higher voltages, and several strings connected in parallel to increase the power. Currently the most widely available string voltages are designed for operation under 1000V open-circuit voltage (800-900V typically), due to the voltage insulation limits of the PV modules. However, latest PV module development reaches 1500V [62], while the inverter grid side voltage is usually 690V. For single-stage PV systems it will require the inverter to work with smaller duty cycles in buck operation forcing the converter to work in ratings where it is not very efficient. This has become an issue in desert areas with large temperature fluctuations, with colder mornings and evenings, in which the PV string voltage is highest. Furthermore, the semiconductors of the inverter must be rated to operate at such high voltage level. This is why the two-stage solutions are becoming popular, also considering the increased MPPT capability.

4.2.1 Step-Down I Partial Power Converter

Based on the PPC configuration shown in Fig. 4.9 a step-down operation can be achieved. This connection splits the power at the PV-side, which allows a voltage reduction at the input side of the dc-dc converter. Then the semiconductor is sized to commute with this reduced voltage.

Partial power ratio

Based on the circuit connection illustrated in Fig. 4.9, the voltage and current are expressed as:

$$V_{dc} = V_{pv} - V_{pc} \tag{4.2.1}$$

$$I_{in} = I_o - I_{pc} \tag{4.2.2}$$

In order to define the operation region of the Step-Down II PPC, the partial

Figure 4.10: Partial power operation range of the Step-Down I PPC.

power ratio K_{pr} (4.1.6), is calculated as:

$$K_{pr} = \frac{V_{pc}I_o}{V_{pv}I_{in}}$$

$$K_{pr} = \frac{(V_{pv} - V_{dc})I_o}{V_{pv}I_{in}} \tag{4.2.3}$$

$$K_{pr} = \frac{I_o}{I_{in}} - \frac{V_{dc}I_o}{V_{pv}I_{in}}$$

In order to express the K_{pr} in terms of the voltage gain, (4.1.3) is included in (4.2.3) and the partial power ratio is finally defined as:
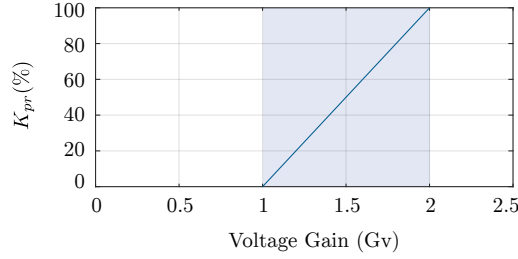
$$K_{pr} = \eta_{dc_s}\left(\frac{1}{G_v} - 1\right) \tag{4.2.4}$$

Considering that the dc-stage is highly efficiency $\eta_{dc_s} \approx 1$, the partial power ratio K_{pr} varies depending on the voltage gain G_v as presented in the Fig. 4.10. Where the shadowed area represents the region of partial power operation. Notice that in contrast with the Step-Down I PPC configuration, this partial ratio is limited by the voltage gain, as can be seen in the figure the minimum value is limited to the half of the input voltage. It might be seen as a drawback, but considering that the PV design is considered to work within a low partial power region and due to variations on solar irradiation, the PV voltage will vary around the dc-link voltage.

Analysis of topology

Working with a Flyback topology for the PPC configuration, and connecting as depicted in Fig. 4.11 (a), the dc-dc converter voltage gain G_{vc} is calculated as:

$$G_{vc} = \frac{V_{pv}}{V_{pc}} = \frac{n_T d}{1 - d} \tag{4.2.5}$$
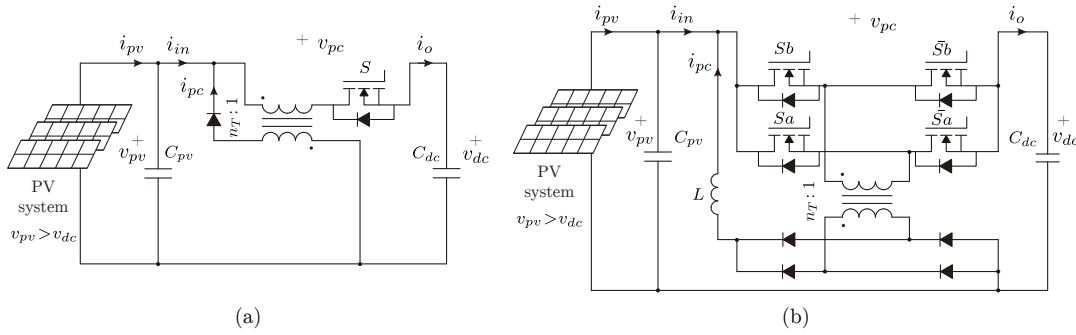
Figure 4.11: Step-Down I Partial Power Converters. (a) Based on Flyback topology. (b) Based on Full-bridge topology.

Applying (4.2.1), the equation can be expressed as:

$$\frac{V_{pv}}{V_{pv} - V_{dc}} = \frac{n_T d}{1 - d} \tag{4.2.6}$$

Rearranging and simplifying the expression, and also considering (4.1.1). Then the global voltage gain can be expressed as:

$$G_v = \frac{d(n_T + 1) - 1}{n_T d} \tag{4.2.7}$$

The voltage gain (4.2.7) depends on the duty cycle d, which is limited to [0-1], and the transformer turns ratio n_T. The operation range is shown in Fig. 4.12 (a), where the shadowed area represents the region of partial power operation.

From this picture it is possible to see that using a Flyback topology for the PPC configuration, the converter operation does not present limitations in terms of duty cycle and voltage reduction. However, the limitation comes from the partial power region which does not allow a reduction lower than the half of the input voltage. Nevertheless, using a transformer with fewer turns ratio (e.g $n_T < 2$) the duty cycle range is limited less than the 50%. On the other hand, transformers with greater turns ratio allows a wider region of operation for the duty cycle.

Working with a Full-bridge topology for the PPC configuration, and connecting as illustrated in Fig. 4.11 (b), the dc-dc converter voltage gain G_{vc} is calculated as:

$$G_{vc} = \frac{V_{pv}}{V_{pc}} = n_T(1 - d) \tag{4.2.8}$$

Figure 4.12: Operation range of the Step-Down I PPC for different transformer turns ratio n_T. (a) Based on Flyback topology. (b) Based on Full-bridge topology.

Applying (4.2.1), the equation can be expressed as:

$$\frac{V_{pv}}{V_{pv} - V_{dc}} = n_T(1 - d) \tag{4.2.9}$$

Rearranging and simplifying the expression, and also considering (4.1.1). Then the global voltage gain can be expressed as:

$$G_v = \frac{n_T(1 - d) - 1}{n_T(1 - d)} \tag{4.2.10}$$

The voltage gain (4.2.10) depends on the duty cycle d and the transformer turns ratio n_T. The operation range is presented in Fig. 4.12 (b), where the shadowed area represents the region of partial power operation.

From this picture it is possible to see that working with a Full-bridge the voltage gain is limited by the turns ratio selection, being more critical than working with a Flyback topology. Also depending on the PV application, different advantages can be taken from the configuration.

For example, considering a voltage gain (e.g $G_v > 0.8$), the greater turns ratio allows the proper operation ($n_T \geq 8$). It means that whereas the partial power ratio is reduced (PV voltage closer to the dc-link voltage), then the transformer turns ratio must be increased in order to guarantee the operation with a wider range of duty cycle.

Discussion and commentaries

When modern high voltage insulated modules are used in larger strings, the operation in buck mode is required to perform grid connection. Considering that these architectures are oriented to medium and high power applications,
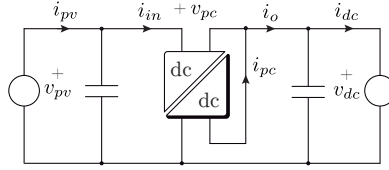
Figure 4.13: Step-Down PPC with partial connection at the dc-link (Step-Down II).

the isolated Full-bridge topology becomes the most practical solution for making the PPC configuration. Moreover, considering that due to the atmospheric fluctuations such as the reduction of the solar irradiation, the PV voltage gets closer to the dc-link voltage. It also leads to the reduction of the partial power ratio, which is translated in an increment of the conversion efficiency.

As an example with Full-bridge topology, some feasible parameters for a PV string are a series connection made with 15 PV modules $V_{pv} = 450V$, and a single phase inverter $V_{dc} = 360V$ for a grid of $V_g = 220V_{rms}$, the voltage gain is $G_v = 0.8$ and the partial ratio varies around $K_{pr} \approx 25\%$. It is possible to see that the maximum voltage gain will be $G_v = 0.93$ if a transformer with $n_T = 16$ is used. It shows that in order to increase the voltage gain ratio and reduce the partial ratio, a transformer with greater turns ratio is required.

4.2.2 Step-Down II Partial Power Converter

Another connection allowed to achieve a voltage reduction is through the PPC configuration depicted in Fig. 4.13, where the power splitting is made at the dc-link side. With this connection the voltage at the input side of the dc-dc converter is reduced, then the semiconductor is sized to commutate with this reduced voltage.

Partial power ratio

Based on the circuit connection shown in Fig. 4.13, the voltage and current are expressed as:

$$V_{dc} = V_{pv} - V_{pc} \tag{4.2.11}$$

$$I_{in} = I_o - I_{pc} \tag{4.2.12}$$

In order to define the operation region of the Step-Down II PPC, the partial
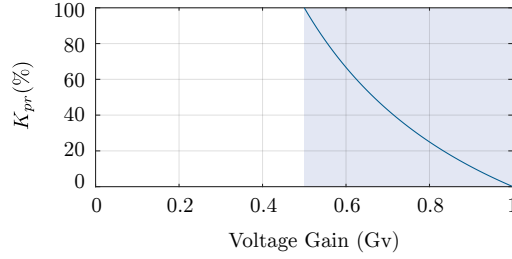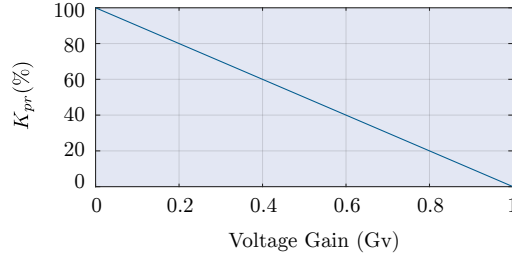
Figure 4.14: Partial power operation range of the Step-Down II PPC.

power ratio K_{pr} (4.1.6), is calculated as:

$$
\begin{aligned}
K_{pr} &= \frac{V_{pc}I_{in}}{V_{pv}I_{in}} \\
K_{pr} &= \frac{V_{pv} - V_{dc}}{V_{pv}} \\
K_{pr} &= 1 - \frac{V_{dc}}{V_{pv}}
\end{aligned}
\tag{4.2.13}
$$

In order to express the K_{pr} in terms of the voltage gain, (4.1.3) is included in (4.2.13) and the partial power ratio is finally defined as:

$$
K_{pr} = 1 - G_v
\tag{4.2.14}
$$

In that case, the input current I_{in} is the same for the PV system and the current trough the dc-dc converter. That is the reason why the term of the dc-stage efficiency does not appear in (4.2.14). The partial power ratio K_{pr} varies linearly, depending on the voltage gain G_v as illustrated in the Fig. 4.14. Where the shadowed area represents the region of partial power operation.

Analysis of topology

Working with a Flyback topology for the PPC configuration, and connecting as presented in Fig. 4.15 (a), the dc-dc converter voltage gain G_{vc} is calculated as:

$$
G_{vc} = \frac{V_{dc}}{V_{pc}} = \frac{n_T d}{1 - d}
\tag{4.2.15}
$$

Applying (4.2.11), the equation can be expressed as:

$$
\frac{V_{dc}}{V_{pv} - V_{dc}} = \frac{n_T d}{1 - d}
\tag{4.2.16}
$$
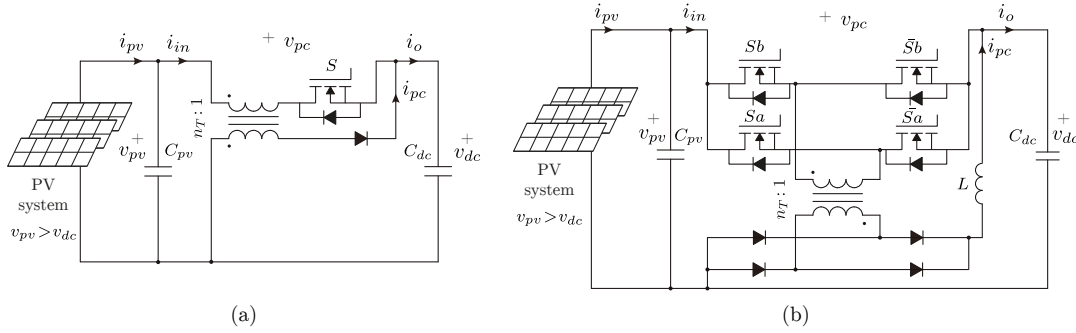
Figure 4.15: Step-Down II Partial Power Converters. (a) Based on Flyback topology. (b) Based on Full-bridge topology.

Rearranging and simplifying the expression, and also considering (4.1.1). Then the global voltage gain can be expressed as:

$$G_v = \frac{n_T d}{1 + d(n_T - 1)} \tag{4.2.17}$$

The voltage gain (4.2.17) depends on the duty cycle d, which is limited to [0-1], and the transformer turns ratio n_T. The operation range is depicted in Fig. 4.16 (a), where the shadowed area represents the region of partial power operation.

From this picture it is possible to see that using a Flyback topology for the PPC configuration, the converter operation is neither limited by the voltage gain, nor the transformer turns ratio. However, depending on the design requirements, the selection criteria about the transformer turns ratio must be considered. In cases where the voltage gain is closer to the unity (reduced K_{pr}), the appropriate solution would be a transformer with greater turns ratio in order to have a higher operation range of the duty cycle. On the other hand, if the application requires a deeper voltage reduction (higher K_{pr}), the solution would be a transformer with fewer turns ratio in order to increase the duty cycle range.

Working with a Full-bridge topology for the PPC configuration, and connecting as shown in Fig. 4.15 (b), the dc-dc converter voltage gain G_{vc} is calculated as:

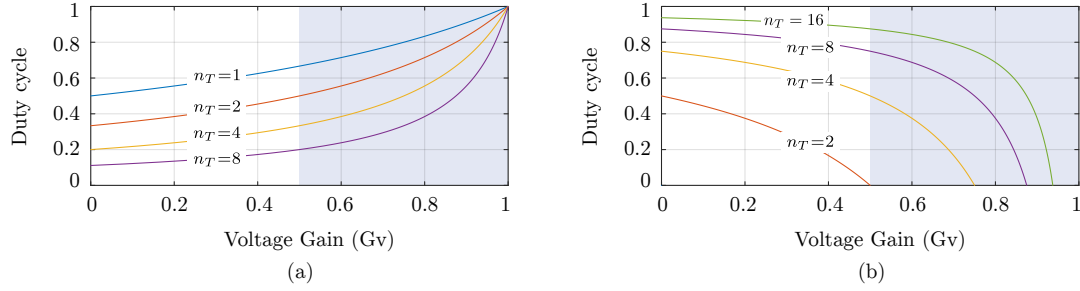$$G_{vc} = \frac{V_{dc}}{V_{pc}} = n_T(1 - d) \tag{4.2.18}$$
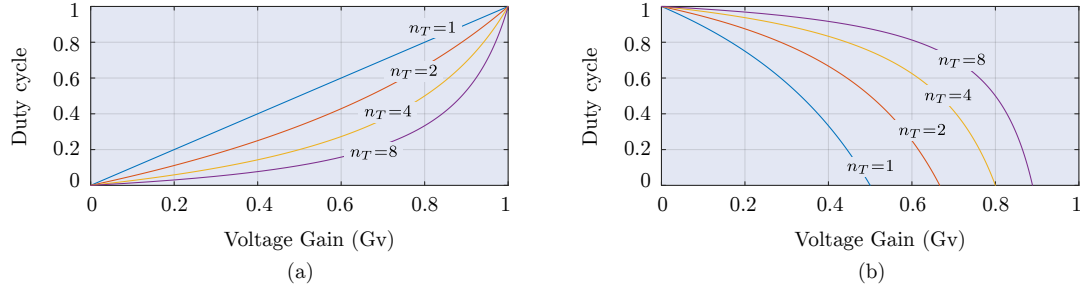
Figure 4.16: Operation range of the Step-Down II PPC for different transformer turns ratio n_T. (a) Based on Flyback topology. (b) Based on Full-bridge topology.

Applying (4.2.11), the equation can be expressed as:

$$\frac{V_{dc}}{V_{pv} - V_{dc}} = n_T(1 - d) \tag{4.2.19}$$

Rearranging and simplifying the expression, and also considering (4.1.1). Then the global voltage gain can be expressed as:

$$G_v = \frac{n_T(1 - d)}{n_T(1 - d) + 1} \tag{4.2.20}$$

The voltage gain (4.2.20) depends on the duty cycle d and the transformer turns ratio n_T. The operation range is illustrated in Fig. 4.16 (b), where the shadowed area represents the region of partial power operation.

From this picture it is possible to see that working with a Full-bridge the voltage gain is limited by the turns ratio selection. Also depending on the PV application, different advantages can be taken from the configuration.

For example, considering a voltage gain (e.g $G_v > 0.5$), the greater turns ratio allows a higher voltage gain. It means that the PV system is designed to operate close to the dc-link voltage, then the partial power ratio is reduced. Considering a design where the converter is sized to handle the 40% of the nominal power as a maximum value, the voltage reduction will be as much the 60% of the input voltage. In that case the appropriate solution is using a transformer with $n = 8$ turn ratio, in order to work with a voltage range to track the maximum power point between 60%-90% of the input voltage.

Discussion and commentaries

Another option to reduce the voltage with a PPC configuration is presented in this section. Due to the flexibility to connect in series the PV modules,

Table 4.1: PV system parameters for a grid connection of $V_g = 220V_{rms}$.

PV Parameters	PV module	PV string 1	PV string 2
PV voltage (V)	30	300	450
Dc-link voltage (V)	360	360	360
PV current (A)	8	8	8
PV power (W)	240	2400	3600
Voltage gain (G_v)	12	1.2	0.8

the PV system voltage can be sized to operate closer than the dc-link voltage, reducing the partial ratio. Moreover, the solar irradiation changes can even reduce the input voltage allowing an operation closer to the dc-link voltage. This kind of configurations are oriented to high power applications, which means that the Flyback topology is not a practical solution for this PPC configuration.

As an example using a Full-bridge topology, some feasible parameters for a PV string are a series connection made with 16 PV modules $V_{pv} = 480V$, and a single phase inverter $V_{dc} = 360V$ for a grid of $V_g = 220V_{rms}$, the voltage gain is $G_v = 0.75$. It is possible to see that whether a transformer with greater turns ratio is used, the range of the voltage gain increases allowing a reduction of the partial power ratio ($K_{pr} < 25\%$). It is the appropriate option for this kind of application, so that the PV voltage can be reduced due to the variation of solar irradiation.

4.3 Summary and Conclusion

This section provided a comprehensive comparison between the different PPC configurations for PV systems. As was analyzed, each configuration presents different advantages and disadvantages depending on the PV application. In order to summarize the principal features of the PPC configurations analyzed in this chapter, a case of study is shown in the Table 4.1. The characteristics are summarized in Table 4.2, only considering the topologies which have more practical interest for PV systems.

Table 4.2: Comparison between different partial power configurations.

	Step-Up I	Step-Up II	Step-Down I	Step-Down II
PV application	Microinverter & String inverter ($v_{pv} < v_{dc}$)	String inverter ($V_{dc}/2 < V_{pv} < V_{dc}$)	String inverter ($V_{pv}/2 < V_{dc} < V_{pv}$)	String inverter ($V_{pv} > V_{dc}$)
Practical topology	Flyback (Microinverter) Full-bridge (String)	Full-bridge	Full-bridge	Full-bridge
PV system	PV module	PV string 1	PV string 2	PV string 2
Partial power ratio (%)	> 91.67	> 20	< 25	< 20
Power processed (W)	220	480	900	720
Turns ratio (n_T)	10	3	16	16
Advantages	• High range of G_v operating as PPC • Mosfet commutes a low current • Diode blocking reduced voltage	• Wide duty cycle operation range	• Partial ratio reduction in case of atmospheric changes	• High range of G_v operating as PPC • Partial ratio reduction in case of atmospheric changes • Mosfets blocking reduced voltage • Diodes conducting low current
Disadvantages	• High partial ratio due to the voltage elevation	• Partial ratio limited by G_v • Diodes conducting high current • Mosfets blocking high voltage	• Partial ratio limited by G_v • Maximum voltage gain is limited by the transformer turns ratio	• Maximum voltage gain is limited by the transformer turns ratio

Chapter 5

MATHEMATICAL MODEL AND CONTROL STRATEGY

This chapter presents the mathematical models for the proposed PPC configurations, which will be tested in the laboratory. They are based on state variables using traditional Flyback and Full-bridge dc-dc converters for the PPC configurations. In addition, the proposed control scheme is discussed, which will be implemented even in simulation and experimental evaluations. Also it is presented the modulation scheme used in the experimental platform. All the mathematical analysis are made based on the assumption that the converters are designed to operate in continuous conduction mode (CCM).

5.1 Mathematical model

The mathematical model is derived from Fig. 5.1. The PPC configurations are modeled through state variables, and they are used to find the parameters for the controllers. Moreover, the dc-dc converters are modulated with a high frequency carrier signal, therefore it is possible to assume that duty cycle d is a continuous signal. It takes values from $[0-1]$. The assumption of this model is that the converter works around the maximum power point, therefore the maximum power is expressed as $(P_{pv} = v_{pv}i_{pv})$ and the power is considered as a parameter obtained from the information of the PV system.

5.1.1 Step-Up I Flyback based PPC model using variables of state

Considering the Fig. 5.1 (a), the dynamic equation for the current in the magnetized inductance can be derived as:

$$v_{pv}d - v_{L_m}d + v_{pv}(1-d) - v_{pc}(1-d) - v_{dc}(1-d) = 0$$
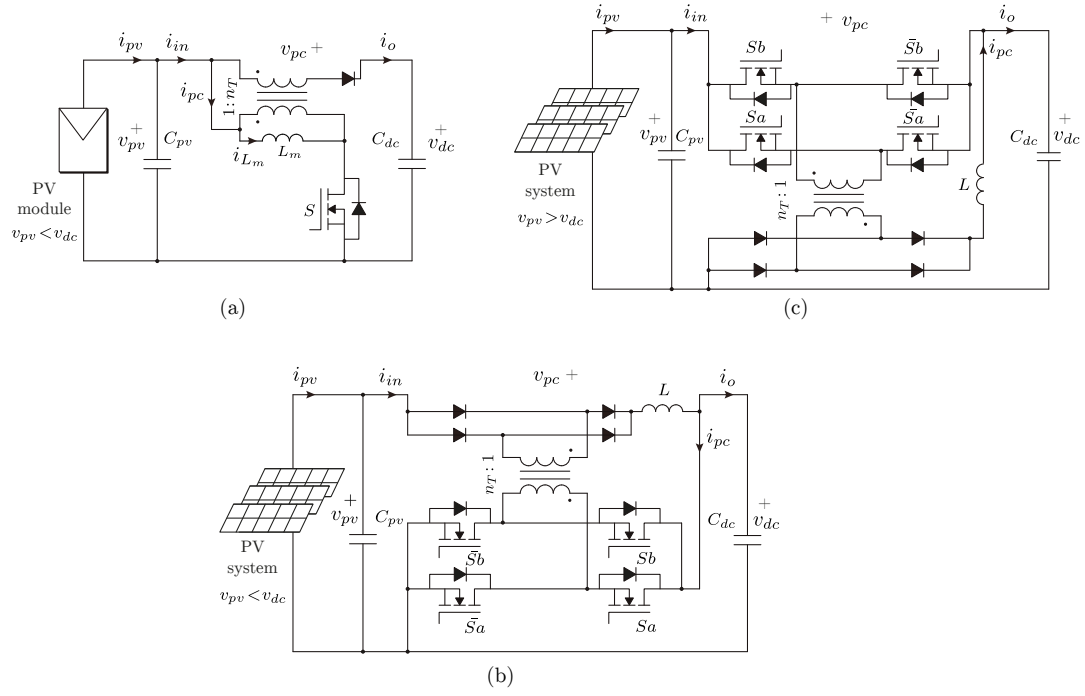
Figure 5.1: Topologies selected for simulation. (a) Step-Up I Flyback based PPC. (b) Step-Up II Full-bridge based PPC. (c) Step-Down I Full-bridge based PPC.

$$v_{L_m} = v_{pv}\frac{1 - n_T d}{d} - v_{dc}\frac{1 - d}{d}$$

$$\frac{di_{L_m}}{dt} = \frac{1}{L_m d}(v_{pv}(1 - n_T d) - v_{dc}(1 - d)) \tag{5.1.1}$$

Moreover, the dynamic equation for the input voltage in the capacitor C_{pv} is calculated by:

$$i_{pv} - i_{in} - i_{C_{pv}} = 0$$

$$i_{C_{pv}} = i_{pv} - i_{L_m} - i_o\left(\frac{n_T d}{1 - d}\right)$$

$$\frac{dv_{pv}}{dt} = \frac{1}{C_{pv}}\left(\frac{P_{pv}}{v_{pv}} - i_{L_m} - \frac{P_{pv}}{v_{dc}}\left(\frac{n_T d}{1 - d}\right)\right) \tag{5.1.2}$$

In order to express in variables of state, it is possible to consider the following representations:

$$u = d$$
$$p = v_{dc}$$

$$x = \begin{bmatrix} x_1 = i_{Lm} \\ x_2 = v_{pv} \end{bmatrix}$$

$$\dot{x} = f_{(x,u,p)}$$

$$\dot{x} = \begin{bmatrix} \dot{x}_1 \\ \dot{x}_2 \end{bmatrix} = \begin{bmatrix} \frac{1}{L_m u}(x_2(1 - n_T u) - p(1 - u)) \\ \frac{1}{C_{pv}} \left(\frac{P_{pv}}{x_2} - x_1 - \frac{P_{pv}}{p} \left(\frac{n_T u}{1-u} \right) \right) \end{bmatrix}$$

$$y = h_{(x,u,p)}$$

$$\dot{x} = \begin{bmatrix} f_1 = \frac{1}{L_m u}(x_2(1 - n_T u) - p(1 - u)) \\ f_2 = \frac{1}{C_{pv}} \left(\frac{P_{pv}}{x_2} - x_1 - \frac{P_{pv}}{p} \left(\frac{n_T u}{1-u} \right) \right) \end{bmatrix} \tag{5.1.3}$$

The equation shown in (5.1.3) represents a non-linear model because there are multiplications between the inputs with the state variables. Therefore, the following analysis is performed to obtain a linear model.

$$\Delta \dot{x} = \mathbf{A} \Delta x + \mathbf{B} \Delta u + \mathbf{E} \Delta p \tag{5.1.4}$$

$$\Delta y = \mathbf{C} \Delta x + \mathbf{D} \Delta u + \mathbf{F} \Delta p \tag{5.1.5}$$

$$\mathbf{A} = \begin{bmatrix} \frac{\partial f_1}{\partial x_1} & \frac{\partial f_1}{\partial x_2} \\ \frac{\partial f_2}{\partial x_1} & \frac{\partial f_2}{\partial x_2} \end{bmatrix} \Bigg|_{\substack{x = x_0 \\ u = u_0 \\ p = p_0}} = \begin{bmatrix} 0 & \frac{1}{L_m} \left(\frac{1 - n_T u_0}{u_0} \right) \\ -\frac{1}{C_{pv}} & -\frac{P_{pv}}{C_{pv} x_{20}^2} \end{bmatrix}$$

$$\mathbf{B} = \begin{bmatrix} \frac{\partial f_1}{\partial u} \\ \frac{\partial f_2}{\partial u} \end{bmatrix} \Bigg|_{\substack{x = x_0 \\ u = u_0 \\ p = p_0}} = \begin{bmatrix} -\frac{1}{u_0^2 L_m}(x_{20} - p_0) \\ -\frac{1}{(1-u_0)^2 C_{pv}} \left(\frac{n_T P_{pv}}{p_0} \right) \end{bmatrix}$$

$$\mathbf{E} = \begin{bmatrix} \frac{\partial f_1}{\partial p} \\ \frac{\partial f_2}{\partial p} \end{bmatrix} \Bigg|_{\substack{x = x_0 \\ u = u_0 \\ p = p_0}} = \begin{bmatrix} -\frac{1}{L_m} \left(\frac{1 - u_0}{u_0} \right) \\ \frac{P_{pv}}{C_{pv} p_0^2} \left(\frac{n_T u_0}{1 - u_0} \right) \end{bmatrix}$$

With the obtained matrix is possible to solve the linearized equations around an operating point as shown below.

$$s \cdot \Delta x = \mathbf{A} \Delta x + \mathbf{B} \Delta u \tag{5.1.6}$$

$$\Delta y = \mathbf{C} \Delta x \tag{5.1.7}$$

$$\frac{\Delta y}{\Delta u} = \mathbf{C} \cdot (s\mathbf{I} - \mathbf{A})^{-1} \cdot \mathbf{B} \tag{5.1.8}$$

This model is given for a generic variable, hence it can be expressed for current and the duty cycle by:

$$\begin{bmatrix} \Delta y = \Delta i_{L_m} \\ C = \begin{bmatrix} 1 & 0 \end{bmatrix} \end{bmatrix}$$

On the other hand, in can be expressed for input voltage and the duty cycle by:

$$\begin{bmatrix} \Delta y = \Delta v_{pv} \\ C = \begin{bmatrix} 0 & 1 \end{bmatrix} \end{bmatrix}$$

5.1.2   Step-Up II Full-bridge based PPC model using variables of state

Considering the Fig. 5.1 (b), the dynamic equation for the current in the inductance can be derived as:

$$v_{pv} + v_{dc}\frac{1-d}{n_T} - v_L - v_{dc} = 0$$

$$v_L = v_{pv} + v_{dc}\left(\frac{1-d}{n_T} - 1\right)$$

$$\frac{di_L}{dt} = \frac{1}{L}\left(v_{pv} + v_{dc}\left(\frac{1-d}{n_T} - 1\right)\right) \tag{5.1.9}$$

Moreover, the dynamic equation for the input voltage in the capacitor C_{pv} is calculated by:

$$i_{pv} - i_{in} - i_{C_{pv}} = 0$$

$$i_{C_{pv}} = i_{pv} - i_{in}$$

$$\frac{dv_{pv}}{dt} = \frac{1}{C_{pv}}\left(\frac{P_{pv}}{v_{pv}} - i_{in}\right) \tag{5.1.10}$$

In order to express in variables of state, it is possible to consider the following representations:

$$x = \begin{bmatrix} x_1 = i_L \\ x_2 = v_{pv} \end{bmatrix}$$

$$u = d$$
$$p = v_{dc}$$

$$\dot{x} = \begin{bmatrix} \dot{x}_1 \\ \dot{x}_2 \end{bmatrix} = \begin{bmatrix} \frac{1}{L}\left(x_2 + p\left(\frac{1-u-n_T}{n_T}\right)\right) \\ \frac{1}{C_{pv}}\left(\frac{P_{pv}}{x_2} - x_1\right) \end{bmatrix}$$

$$\dot{x} = f_{(x,u,p)}$$

$$y = h_{(x,u,p)}$$

$$\dot{x} = \begin{bmatrix} f_1 = \frac{1}{L}\left(x_2 + p\left(\frac{1-u-n_T}{n_T}\right)\right) \\ f_2 = \frac{1}{C_{pv}}\left(\frac{P_{pv}}{x_2} - x_1\right) \end{bmatrix} \tag{5.1.11}$$

The equation shown in (5.1.11) represents a non-linear model because there are multiplications between the inputs with the state variables. Therefore, the following analysis is derived to obtain a linear model.

$$\Delta\dot{x} = \mathbf{A}\Delta x + \mathbf{B}\Delta u + \mathbf{E}\Delta p \tag{5.1.12}$$

$$\Delta y = \mathbf{C}\Delta x + \mathbf{D}\Delta u + \mathbf{F}\Delta p \tag{5.1.13}$$

$$\mathbf{A} = \begin{bmatrix} \frac{\partial f_1}{\partial x_1} & \frac{\partial f_1}{\partial x_2} \\ \frac{\partial f_2}{\partial x_1} & \frac{\partial f_2}{\partial x_2} \end{bmatrix}\Bigg|_{\substack{x=x_0 \\ u=u_0 \\ p=p_0}} = \begin{bmatrix} 0 & \frac{1}{L} \\ -\frac{1}{C_{pv}} & -\frac{P_{pv}}{C_{pv}x_{20}^2} \end{bmatrix}$$

$$\mathbf{B} = \begin{bmatrix} \frac{\partial f_1}{\partial u} \\ \frac{\partial f_2}{\partial u} \end{bmatrix}\Bigg|_{\substack{x=x_0 \\ u=u_0 \\ p=p_0}} = \begin{bmatrix} -\frac{p_0}{Ln_T} \\ 0 \end{bmatrix}$$

$$\mathbf{E} = \begin{bmatrix} \frac{\partial f_1}{\partial p} \\ \frac{\partial f_2}{\partial p} \end{bmatrix}\Bigg|_{\substack{x=x_0 \\ u=u_0 \\ p=p_0}} = \begin{bmatrix} \frac{1}{L}\left(\frac{1-u_0-n_T}{n_T}\right) \\ 0 \end{bmatrix}$$

With the obtained matrix is possible to solve the linearized equations around an operating point as shown below.

$$s \cdot \Delta x = \mathbf{A}\Delta x + \mathbf{B}\Delta u \tag{5.1.14}$$

$$\Delta y = \mathbf{C}\Delta x \tag{5.1.15}$$

$$\frac{\Delta y}{\Delta u} = \mathbf{C} \cdot (s\mathbf{I} - \mathbf{A})^{-1} \cdot \mathbf{B} \tag{5.1.16}$$

This model is given for a generic variable, hence it can be expressed for current and the duty cycle by:

$$\begin{bmatrix} \Delta y = \Delta i_L \\ C = [1 \quad 0] \end{bmatrix}$$

On the other hand, in can be expressed for input voltage and the duty cycle by:

$$\begin{bmatrix} \Delta y = \Delta v_{pv} \\ C = [0 \quad 1] \end{bmatrix}$$

5.1.3   Step-Down II Full-bridge based PPC model using variables of state

Considering the Fig. 5.1 (c), the dynamic equation for the current in the inductance can be derived as:

$$(v_{pv} - v_{dc})n_T(1 - d) - v_L - v_{dc} = 0$$

$$v_L = v_{pv}n_T(1 - d) - v_{dc}(n_T(1 - d) + 1)$$

$$\frac{di_L}{dt} = \frac{1}{L}(v_{pv}n_T(1 - d) - v_{dc}(n_T(1 - d) + 1)) \qquad (5.1.17)$$

Moreover, the dynamic equation for the input voltage in the capacitor C_{pv} is calculated by:

$$i_{pv} - i_{in} - i_{C_{pv}} = 0$$

$$i_{C_{pv}} = i_{pv} - i_{in}$$

$$\frac{dv_{pv}}{dt} = \frac{1}{C_{pv}}\left(\frac{P_{pv}}{v_{pv}} - \frac{P_{pv}}{v_{dc}} + i_L\right) \qquad (5.1.18)$$

In order to express in variables of state, it is possible to consider the following representations:

$$x = \begin{bmatrix} x_1 = i_L \\ x_2 = v_{pv} \end{bmatrix} \qquad \begin{matrix} u = d \\ p = v_{dc} \end{matrix}$$

$$\dot{x} = \begin{bmatrix} \dot{x}_1 \\ \dot{x}_2 \end{bmatrix} = \begin{bmatrix} \frac{1}{L}(x_2 n_T(1 - u) - p(n_T(1 - u) + 1)) \\ \frac{1}{C_{pv}}\left(\frac{P_{pv}}{x_2} - \frac{P_{pv}}{p} + x_1\right) \end{bmatrix} \qquad \begin{matrix} \dot{x} = f_{(x,u,p)} \\ \\ y = h_{(x,u,p)} \end{matrix}$$

$$\dot{x} = \begin{bmatrix} f_1 = \frac{1}{L}(x_2 n_T(1 - u) - p(n_T(1 - u) + 1)) \\ f_2 = \frac{1}{C_{pv}}\left(\frac{P_{pv}}{x_2} - \frac{P_{pv}}{p} + x_1\right) \end{bmatrix} \qquad (5.1.19)$$

The equation shown in (5.1.19) represents a non-linear model because there are multiplications between the inputs with the state variables. Therefore, the following analysis is performed to obtain a linear model.

$$\Delta\dot{x} = \mathbf{A}\Delta x + \mathbf{B}\Delta u + \mathbf{E}\Delta p \qquad (5.1.20)$$

$$\Delta y = \mathbf{C}\Delta x + \mathbf{D}\Delta u + \mathbf{F}\Delta p \qquad (5.1.21)$$

$$\mathbf{A} = \begin{bmatrix} \frac{\partial f_1}{\partial x_1} & \frac{\partial f_1}{\partial x_2} \\ \frac{\partial f_2}{\partial x_1} & \frac{\partial f_2}{\partial x_2} \end{bmatrix} \Bigg|_{\substack{x = x_0 \\ u = u_0 \\ p = p_0}} = \begin{bmatrix} 0 & \frac{1}{L} n_T (1 - u_0) \\ \frac{1}{C_{pv}} & -\frac{P_{pv}}{C_{pv} x_{20}^2} \end{bmatrix}$$

$$\mathbf{B} = \begin{bmatrix} \frac{\partial f_1}{\partial u} \\ \frac{\partial f_2}{\partial u} \end{bmatrix} \Bigg|_{\substack{x = x_0 \\ u = u_0 \\ p = p_0}} = \begin{bmatrix} -\frac{n_T}{L}(x_{20} - p_0) \\ 0 \end{bmatrix}$$

$$\mathbf{E} = \begin{bmatrix} \frac{\partial f_1}{\partial p} \\ \frac{\partial f_2}{\partial p} \end{bmatrix} \Bigg|_{\substack{x = x_0 \\ u = u_0 \\ p = p_0}} = \begin{bmatrix} -\frac{1}{L}\left(n_T(1 - u_0) + 1\right) \\ \frac{P_{pv}}{C_{pv} p_0^2} \end{bmatrix}$$

With the obtained matrix is possible to solve the linearized equations around an operating point as shown below.

$$s \cdot \Delta x = \mathbf{A} \Delta x + \mathbf{B} \Delta u \tag{5.1.22}$$

$$\Delta y = \mathbf{C} \Delta x \tag{5.1.23}$$

$$\frac{\Delta y}{\Delta u} = \mathbf{C} \cdot (s\mathbf{I} - \mathbf{A})^{-1} \cdot \mathbf{B} \tag{5.1.24}$$

This model is given for a generic variable, hence it can be expressed for current and the duty cycle by:

$$\begin{bmatrix} \Delta y = \Delta i_L \\ C = \begin{bmatrix} 1 & 0 \end{bmatrix} \end{bmatrix}$$

On the other hand, in can be expressed for input voltage and the duty cycle by:

$$\begin{bmatrix} \Delta y = \Delta v_{pv} \\ C = \begin{bmatrix} 0 & 1 \end{bmatrix} \end{bmatrix}$$

5.2   Control Strategy

The control scheme implemented for the partial power converters, is based on cascaded control loops working with linear PI controllers as depicted in Fig. 5.2 (a). In addition, Fig. 5.2 (b) depicts the gate signals when Flyback topology is used. It also includes the signal for the clamping circuit S_c. Finally, Fig. 5.2 (c) shows the gate signals working with a Full-bridge topology, where the signal for the clamping circuit is also considered.
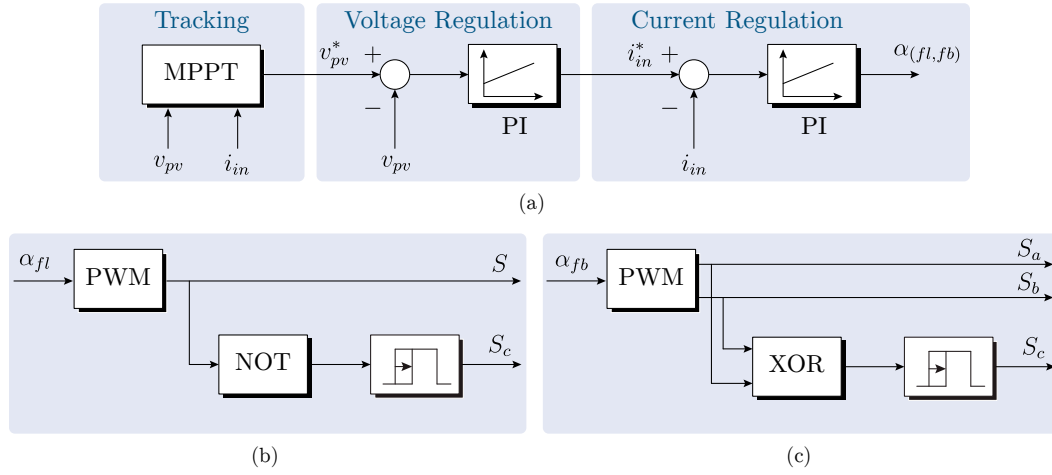
Figure 5.2: Control scheme implemented in the experimental test-bench. (a) General control loops. (b) Gate signal generation for the PPC Flyback based. (c) Gate signal generation for the PPC Full-bridge based.

The procedure of the control design is the same for all the PPC configurations. In this section, an specific case of study will be developed for providing a better understanding of the controllers design by using graphical simulation tools.

5.2.1   Maximum Power Point Algorithm

In order to extract the maximum power from the PV system, a MPPT algorithm is implemented to get the voltage reference. For this purpose, the classical perturb and observe (P&O) algorithm was implemented, due to the simple implementation and effective tracking of the MPP [63]. The flow diagram is shown in Fig. 5.3, it starts taking the measurements of voltage and current of the PV module. The power is compared with the last measurement, in order to know whether the power decreased, which means that the operation point is far from the MPP. In that case the algorithm changes the voltage reference by increasing the value, if the last iteration reduced it, or vise-versa. On the other hand, if the measurement of power is higher than the last iteration, then the operation point is closer to the MPP. It means that the voltage reference will continue in the same direction in order to reach the MPP.

As can be seen, this iteration is always changing the voltage reference in order to obtain observations about the power behavior. It is more clear when a temperature change is made, where the voltage reference is highly affected
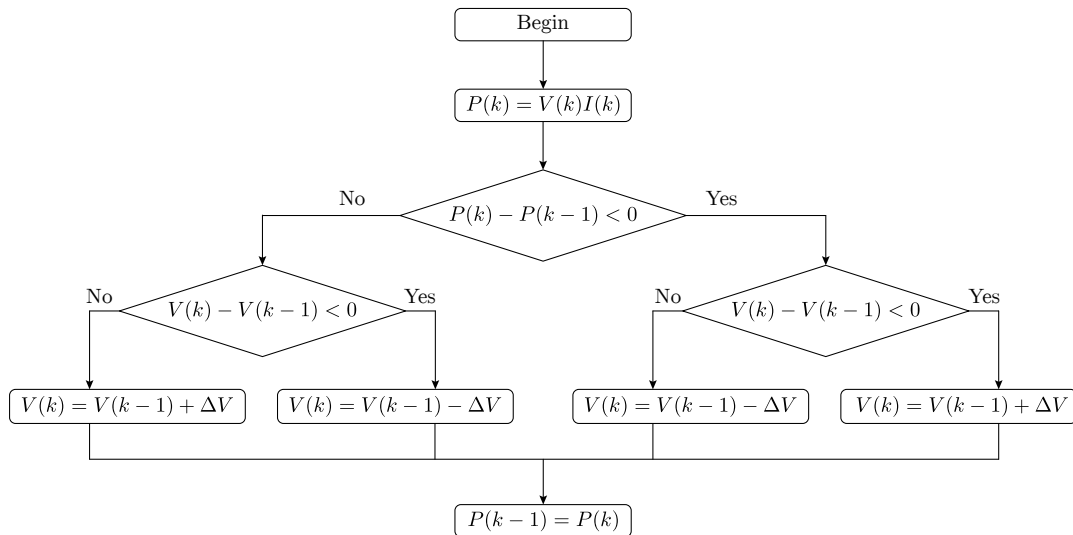
Figure 5.3: Flow diagram of the P&O MPPT algorithm.
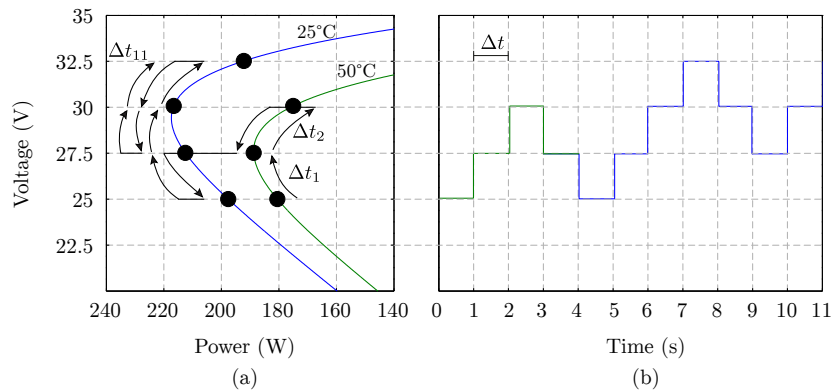
Figure 5.4: P&O MPPT algorithm in front of temperature changes. (a) V-P curve depicting the voltage changes. (b) Voltage changes of the input voltage in temporal domain.

as illustrated in Fig. 5.4 (a). For that reason, the algorithm will produce three levels oscillating around the MPP as presented in Fig. 5.4 (b), which in terms of efficiency is not the optimal solution under highly solar irradiation changes. However, the simplicity has become this algorithm in an attractive and useful solution.

5.2.2   Linear Control Loop

After to get the voltage reference from the MPPT algorithm, the PV voltage is regulated with a linear PI controller. This is the external loop to be designed, because it has a slower dynamic compared with the controlled current. The design of this regulator considers the dynamic of the input capacitance, so that this passive component will be the responsible to regulate the input voltage by changing its current. Therefore, the output signal of the controller is the input current. In order to design the controller it is necessary to firstly obtain the transfer function between the current and the duty cycle. In order to do that it is required to use the expressions derived from the mathematical model. This inner control loop has a faster dynamic compared with the voltage loop, for that reason this controller is designed and tuned firstly solving the expressions (5.1.8, 5.1.16, 5.1.24). The actuator signal is the reference of the duty cycle, which then will be modulated obtaining the gate signals.

To provide a better understanding of the controllers design, an evaluation case is considered for the Step-Down II Full-bridge based PPC. At the beginning the inner control loop is designed. Based on the model in (5.1.24) the transfer function is obtained for the following initial conditions which are taken from the stationary state: $x_{10} = 1.4A$, $x_{20} = 231.7V$, $u_0 = 0.69$, $p_0 = 165.3V$ and PV power $P_{pv} = 1240W$. These results were obtained by experimental measurements. Moreover, from the experimental test-bench the parameters acquired are: transformer turns ratio: $n_T = 8$, input capacitance $C_{pv} = 330\mu F$, output capacitance $C_{dc} = 330\mu F$ and inductance $L = 2.2mH$. The transfer function is:

$$\frac{\Delta I_L}{\Delta d} = \frac{-2.42e^5 s - 1.69e^7}{s^2 + 69.99s - 3.42e^6} \tag{5.2.1}$$

A PI controller is selected for ensuring zero error in stationary state, and to improve the dynamic performance even for the current and voltage control. In order to design the controller, the graphic method based on Matlab$^{\text{®}}$ (rltool) is used for this purpose. The first step is to define the parameters settings, the damping ratio $\zeta = 0.707$, depicted in Fig. 5.5 (a), is selected because it offers a good compromise between rise time and settling time. Then, the cut-off frequency is $f0 = 4kHz$, shown in Fig. 5.5 (b), it is because the switching frequency is $f_{sw} = 80kHz$ and with a decade below the response is good enough in terms of settling time $t_s = 4.3e^{-4}s$, and overshoot $M_p = 20\%$ as illustrated

(a)   (b)   (c)
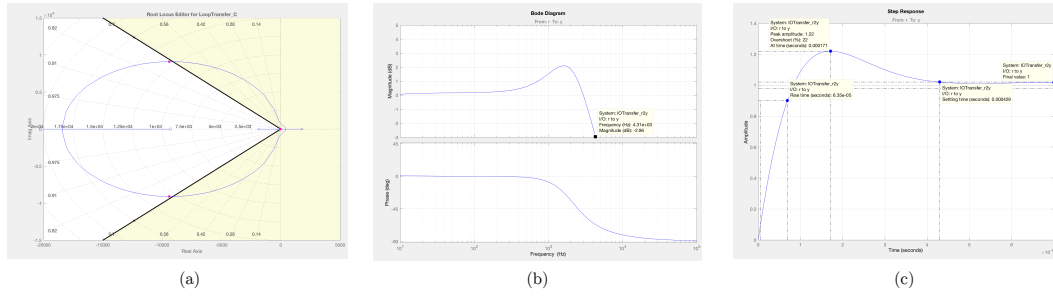
Figure 5.5: Results of the current control design. (a) Root Locus with $\zeta = 0.707$. (b) Closed loop bode diagram. (c) Step response for the closed loop system.

(a)   (b)   (c)
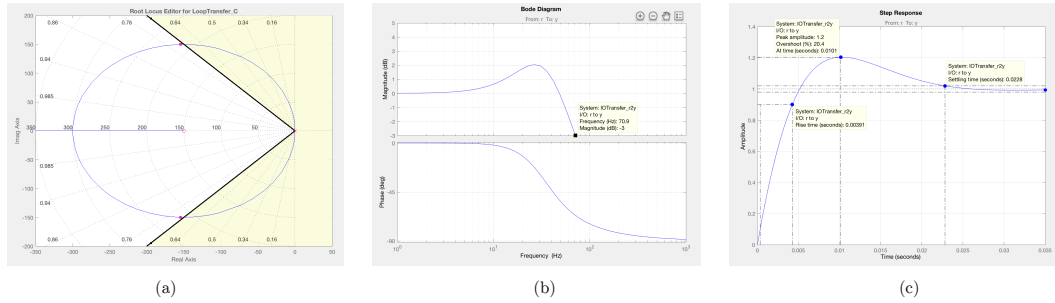
Figure 5.6: Results of the voltage control design. (a) Root Locus with $\zeta = 0.707$. (b) Closed loop bode diagram. (c) Step response for the closed loop system.

in Fig. 5.5 (c). With these criteria, the current controller is:

$$C_{I_L}(s) = -0.09331\frac{s + 7769}{s} \tag{5.2.2}$$

After that, the voltage control loop is design based on the same methodology. In this case the transfer function is obtained as the relation between the input PV voltage, and the current trough the input capacitance. Then a feed forward is implemented in order to obtain the current trough the inductance.

$$\frac{\Delta V_{pv}}{\Delta I_c} = \frac{1}{3.3e^{-4}s} \tag{5.2.3}$$

The same criteria is used for the voltage control loop, only considering that its bandwidth is lower than the current control loop. For that reason the selected cutoff frequency is $f_0 = 71Hz$, which is faster enough for performing the MPPT algorithm ($t \approx 2S$). The results are presented in Fig. 5.6.

With these criteria, the voltage controller is:

$$C_{V_{pv}}(s) = 0.10198\frac{s+150}{s} \tag{5.2.4}$$

This is a classical methodology for designing PI controllers using variables of state. However, the reviewers are also invited to read [64], where Model Predictive Control (MPC) is implemented for dc-dc converters. This can also be an interesting solution for controlling the PPC configurations.

5.3   Summary and Conclusion

In this chapter the mathematical models for the proposed PPC configurations, which will be tested in the laboratory, are presented. They are based on state variables using traditional Flyback and Full-bridge dc-dc converters for the PPC configurations. In addition, the proposed control scheme is discussed, which will be implemented even in simulation and experimental evaluations. Also it is included the discussion of the modulation scheme used in the experimental platform.

Chapter 6

SIMULATION RESULTS

The simulation validation of the different PPC configurations, is made based on traditional PV applications. On each of them, the more practical topologies are chosen which are depicted in Fig. 5.1, and they work with the most appropriate design values in order to take advantage of the configurations. The validation of the PPC configurations, and the control schemes are performed in software PLECS®.

6.1 Step-Up I Flyback based Partial Power Converter

In order to analyze the operation of the Step-Up I Flyback based PPC, the parameters listed in Table 6.1 are implemented in the simulation software. In order to perform the evaluations, some general considerations are made: (a) The PV application is a microinverter connected to a single-phase grid ($V_{rms} = 220V, 50Hz$ and $V_{dc} = 360V$). (b) A solar irradiation change from $1000W/m^2$ to $500W/m^2$ is made at time $t = 0.6s$.

The implemented MPPT algorithm is the traditional $P\&O$. For that reason, it is possible to note from the results shown in Fig. 6.1 (a), the classical three

Table 6.1: Simulation parameters of the Step-Up I Flyback based PPC.

Parameter	Symbol	Value	Parameter	Symbol	Value
PV power	P_{pv}	$300W$	Voltage Kp	K_{pv}	0.01
PV voltage	$V_{pv_{mp}}$	$32V$	Voltage Ki	K_{iv}	200
PV side capacitance	C_{pv}	$10\mu F$	Current Kp	K_{pi}	0.1515
Dc side capacitance	C_{dc}	$1000\mu F$	Current Ki	K_{ii}	500
Transformer turns ratio	n_T	1	Voltage step	Δ_v	0.5
Switching frequency	f_{sw}	$200kHz$	Time step	Δ_t	1.0
Resistive load	R_{dc}	9Ω			

76
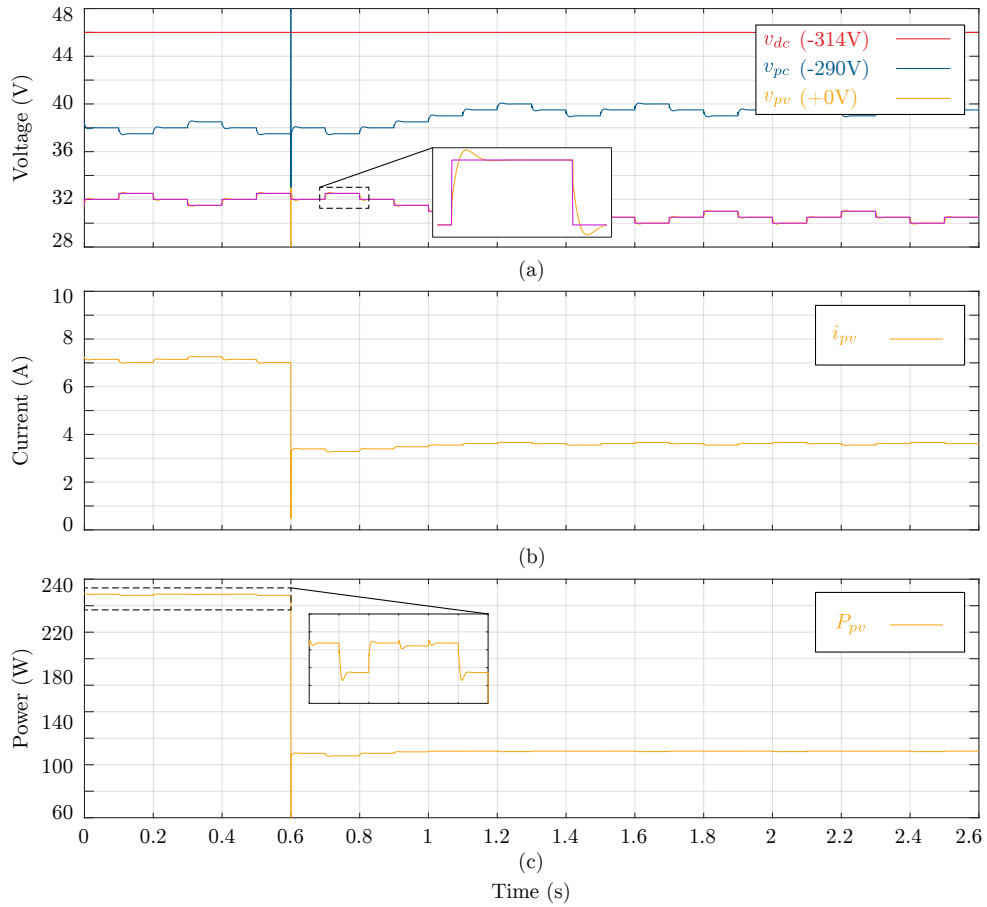
Figure 6.1: Results of the MPPT algorithm of the Step-Up I Flyback based PPC. (a) Voltage results. (b) PV current. (c) PV power.

voltage levels when the system is operating under uniform solar irradiation. Notice that the results are not placed using the same reference value, it was made for presentation purposes. The reference value for each signal is included in each figure. For example, in the voltage waveforms, the dc-link voltage reference is $v_{dc_0} = 314V$, which gives a result of $v_{dc} = 360V$. The same operation is made for all the results illustrated in the following sections. In addition, when a solar irradiation change is made, the PV current decrease enough as presented in Fig. 6.1 (b) also reducing the input PV power as depicted in Fig. 6.1 (c). For that reason, the PV voltage decreases until reach the new MPP, and oscillate around the $v_{pv_{mp}}$ given by the tracking algorithm. As also can be seen from the figure, it shows the voltage at the dc-link side v_{dc}, the PV side v_{pv} and the
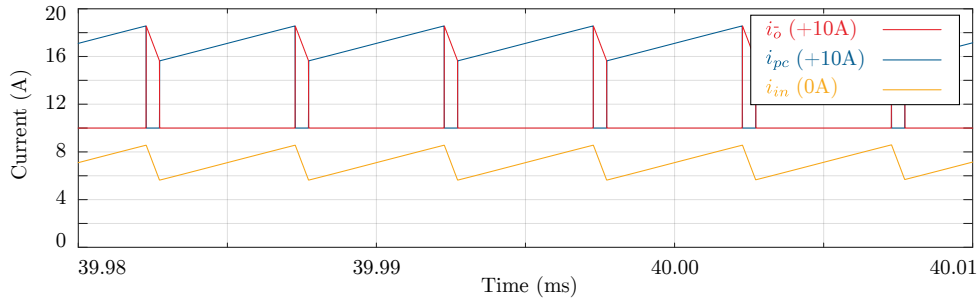
Figure 6.2: Currents in the Step-Up I Flyback based PPC with $D = 0.89$.

compensated by the converter v_{pc}. In order to show them in the same figure with an appropriate resolution of scale, an offset value was included. As can be seen, v_{dc} is the addition between the v_{pc} and v_{pv}, which means that the voltage elevation required to reach the value for the grid-connection is lower than in a traditional FPC $v_{pc} \approx 330V$. On the other hand, when the irradiation change is produced, the voltage decrease in order to reach the new MPP and it produced an increment on v_{pc} which is translated to a higher converter voltage gain.

Another of the advantage working with a Step-Up I Flyback based PPC is shown in Fig. 6.2. Due to the connection used to make the PPC configuration, the input current i_{in} is the addition between the output current i_o and the current flowing trough the dc-dc converter i_{pc}. Moreover, it is possible to note that i_{pc} and i_o present complementary behaviors, it means that when the Mosfet is turned-on the Diode is turned-off and vice-versa. For that reason, the input current presents a continuous waveform and not the traditional switched one, as in the traditional Flyback topology. It is translated in a lower capacitor stress for the PV side, and a reduced sized of this one.

The power waveforms are illustrated in Fig. 6.3 (a), it is possible to note that the converter is handling a lower power ($P_{pc} < P_{pv}$). Although a solar irradiation change is made, the converter stills handling lower than the input power. In Fig. 6.3 (b) the partial power ratio K_{pr} is presented. Notice that after the solar irradiation change, K_{pr} increase but without getting handle the entire input power. Based on this results it is worth concluding that the converter can be designed to operate at nominal values, so that despite of the increment on the K_{pr} value caused by the irradiation changes, it will not handle more than the rated power.

It is worth noticing that solar irradiation variations change the voltage at maximum power point. In order to obtain the PV voltage variation at different irradiation values, the explicit photovoltaic voltage expression explained in the
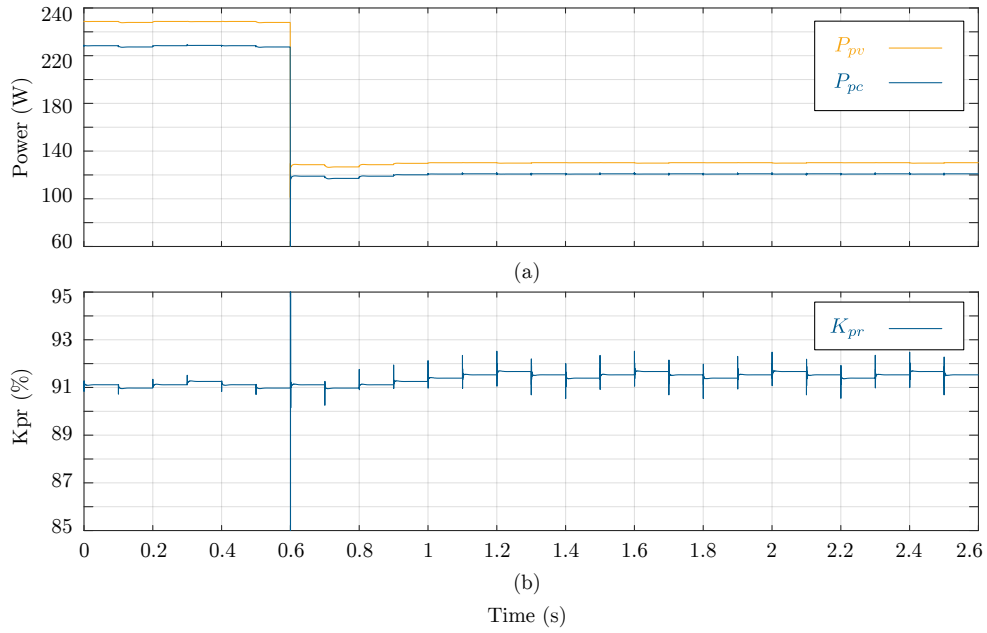
Figure 6.3: (a) PV power and power processed by the converter under solar irradiation changes. (b) Partial power ratio K_{pr} under solar irradiation changes.
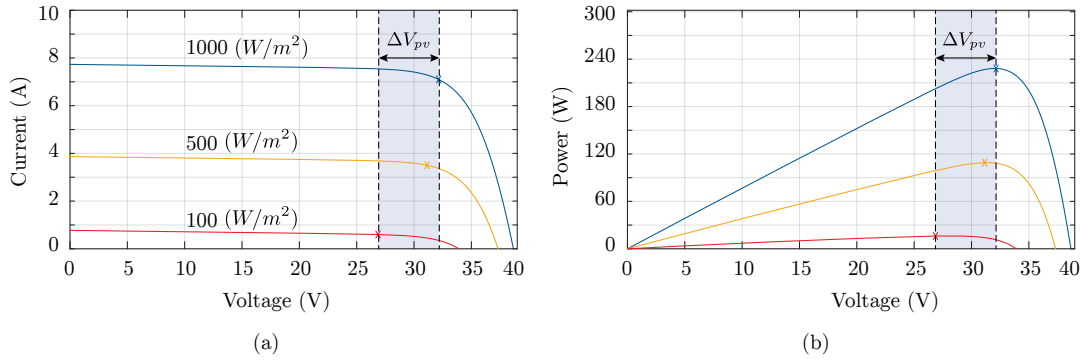
Figure 6.4: PV curves obtained with explicit expression using Lambert's function. (a) I-V PV curve. (b) P-V PV curve.

Subsection 1.1.2 is implemented. As can be seen in (1.1.14), the PV voltage can be expressed as a explicit function of the PV current using Lambert's function. Working with a traditional PV module, the parameters are listed in Table 1.1, and the results are depicted in Fig. 6.4. As can be seen from the figures, the solar irradiation and the current i_{sc} present an almost linear dependence. On

the other hand, the voltage v_{oc} does not change as much as the current. In that evaluation case, the voltage variation from $(1000 - 500W/m^2)$ corresponds to $\Delta V_{pv} = 0.8V$ and $K_{pr} = 91.33\%$. That is the reason to explain the small variation in the $\Delta K_{pr} = 0.22\%$ parameter.

Finally, in order to evaluate the the maximum variation of the partial power ratio, a irradiation change between $(1000 - 50W/m^2)$ is made. In that case, the voltage changes $\Delta V_{pv} = 6.7V$ from the v_{pv} at STC. Moreover, when the irradiation decrease the partial power ratio increases to $K_{pr_{max}} = 93\%$. It shows that the Step-Up I PPC keeps the PPC operation despite of the variations of the solar irradiation.

6.2   Step-Up II Full-bridge based Partial Power Converter

In order to analyze the operation of the Step-Up II Full-bridge based PPC, the parameters listed in Table 6.2 are implemented in the simulation software. In order to perform the evaluations, some general considerations are made: (a) The PV application is a two-stage string inverter made with 10 PV modules in series, and then connected to a single-phase grid ($V_{rms} = 220V, 50Hz$ and $V_{dc} = 360V$). (b) A solar irradiation change from $1000W/m^2$ to $500W/m^2$ is made at time $t = 0.6s$.

Due to the MPPT algorithm ($P\&O$), it is possible to note from the results shown in Fig. 6.5 (a), the classical three voltage levels when the system is operating under uniform solar irradiation. As can be seen, when a solar irradiation change is made, the PV current decrease enough as illustrated in Fig. 6.5 (b) also reducing the input PV power as presented in Fig. 6.5 (c). For that reason, the PV voltage varies until reach the new MPP, and oscillate around the $v_{pv_{mp}}$ given by the tracking algorithm. As also can be seen from the figure, it shows

Table 6.2: Simulation parameters of the Step-Up II Full-bridge based PPC.

Parameter	Symbol	Value	Parameter	Symbol	Value
PV power	P_{pv}	$3000W$	Voltage Kp	K_{pv}	0.009018
PV voltage	$V_{pv_{mp}}$	$320V$	Voltage Ki	K_{iv}	425.6
PV side capacitance	C_{pv}	$330\mu F$	Current Kp	K_{pi}	-0.0504
Dc side capacitance	C_{dc}	$330\mu F$	Current Ki	K_{ii}	1000
Transformer turns ratio	n_T	3	Voltage step	Δ_v	5
Switching frequency	f_{sw}	$80kHz$	Time step	Δ_t	1.0
Resistive load	R_{dc}	20Ω	Inductance	L	$270\mu H$
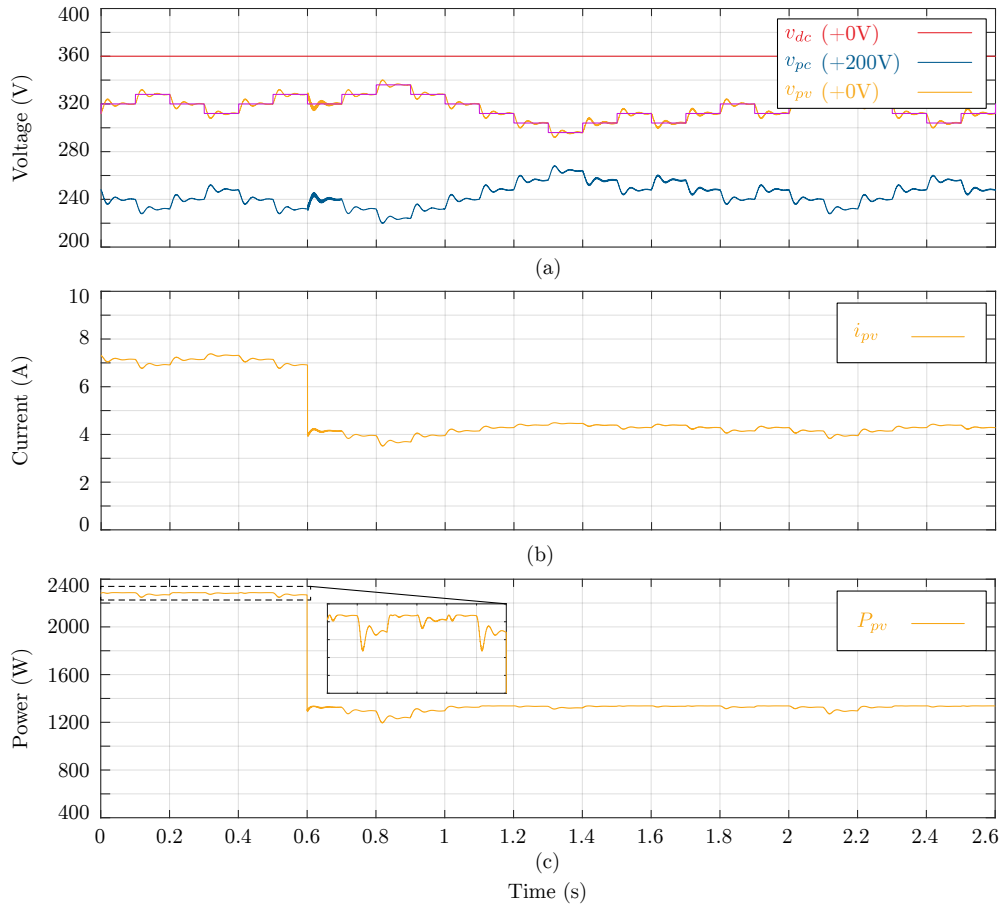
Figure 6.5: Results of the MPPT algorithm of the Step-Up II Full-bridge based PPC. (a) Voltage results. (b) PV current. (c) PV power.

the voltage at the dc-link side v_{dc}, the PV side v_{pv} and the compensated by the converter v_{pc}. In order to show them in the same figure with an appropriate resolution of scale, an offset value was included. As can be seen, v_{dc} is the addition between the v_{pc} and v_{pv}, which means that the voltage elevation required to reach the value for the grid-connection is lower than in a traditional FPC $v_{pc} \approx 40V$. On the other hand, when the irradiation change is produced, the voltage decrease in order to reach the new MPP and it produced an increment on v_{pc} which is translated to a higher converter voltage gain.

Another of the advantage working with a Step-Up II Full-bridge based PPC is depicted in Fig. 6.6. Due to the connection used to make the PPC configuration, the input current i_{in} is the addition between the output current i_o
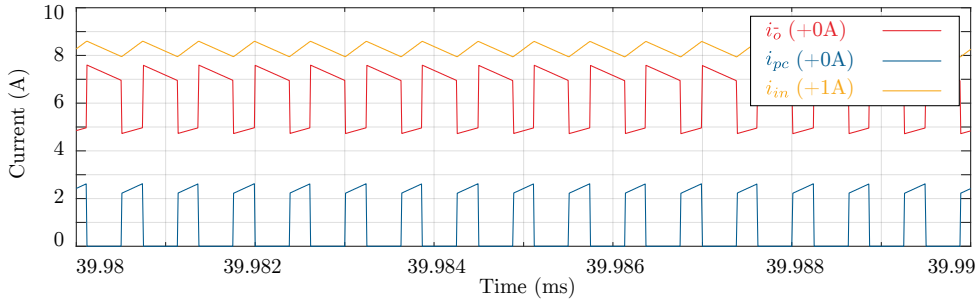
Figure 6.6: Currents in the Step-Up II Full-bridge based PPC with $D = 0.67$.

and the current flowing trough the dc-dc converter i_{pc}. Moreover, it is possible to note that despite the current flowing at the Mosfet bridge i_{pc} is switched, the input current i_{in} is continuous due to the inductor filter connected at the output of the Diodes bridge. It is translated in a lower capacitor stress for the PV side C_{pv}, and a reduced sized of this one.

The power waveforms are shown in Fig. 6.7 (a), it is possible to note that the converter is handling a lower power ($P_{pc} < P_{pv}$). Although a solar irradiation change is made, the converter stills handling lower than the input power. In Fig. 6.7 (b) the partial power ratio K_{pr} is illustrated. Notice that after the solar irradiation change, K_{pr} increase but without getting handle the entire input power. Based on this results it is worth concluding that the converter can be designed to operate at nominal values, so that despite of the increment on the K_{pr} value caused by the irradiation changes, it will not handle more than the rated power.

In order to obtain the PV voltage variation at different irradiation values, the explicit PV voltage expression is implemented. As can be seen in (1.1.14), the PV voltage can be expressed as a explicit function of the PV current using Lambert's function. Working with a traditional PV module, the parameters are listed in Table 1.1, and the results are presented in Fig. 6.8 for the PV string. As can be seen from the figures, the solar irradiation and the current i_{sc} present an almost linear dependence. On the other hand, the voltage v_{oc} does not change as much as the current. In that evaluation case, the voltage variation from $(1000 - 500W/m^2)$ corresponds to $\Delta V_{pv} = 8V$ and $K_{pr} = 15.38\%$. That is the reason to explain the small variation in the $\Delta K_{pr} = 2.88\%$ parameter.

Finally, in order to evaluate the the maximum variation of the partial power ratio, a irradiation change between $(1000 - 50W/m^2)$ is made as depicted in Fig. 6.8. In that case, the voltage changes $\Delta V_{pv} = 67V$ from the v_{pv} at STC. Moreover, when the irradiation decrease the partial power ratio increases to

Figure 6.7: (a) PV power and power processed by the converter under solar irradiation changes. (b) Partial power ratio K_{pr} under solar irradiation changes.
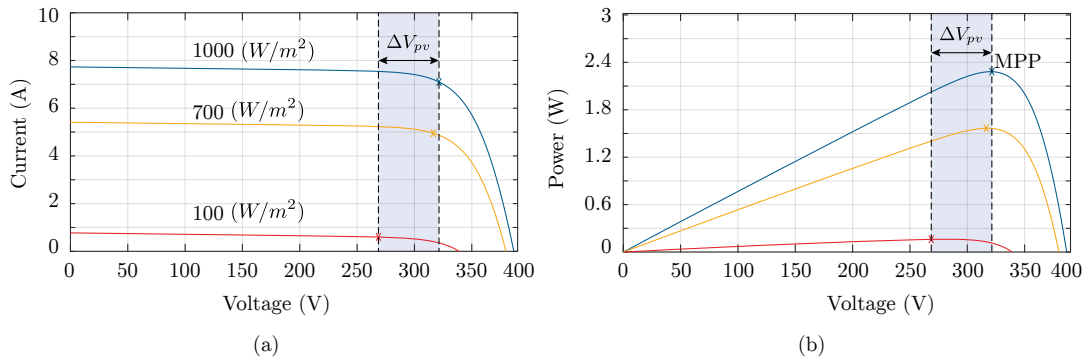
Figure 6.8: PV curves obtained with explicit expression using Lambert's function. (a) I-V PV curve. (b) P-V PV curve.

$K_{pr_{max}} = 42.29\%$. It shows that the Step-Up II PPC keeps the PPC operation under the 50% of the total power, despite of the variations of the solar irradiation.

6.3 Step-Down II Full-bridge based Partial Power Converter

In order to analyze the operation of the Step-Down II Full-bridge based PPC, the parameters listed in Table 6.3 are implemented in the simulation software. In order to perform the evaluations, some general considerations are made: (a) The PV application is a two-stage string inverter made with 15 PV modules in series, and then connected to a single-phase grid ($V_{rms} = 220V, 50Hz$ and $V_{dc} = 360V$). (b) A solar irradiation change from $1000W/m^2$ to $500W/m^2$ is made at time $t = 0.6s$.

Due to the MPPT algorithm ($P\&O$), it is possible to note from the results shown in Fig. 6.9 (a), the classical three voltage levels when the system is operating under uniform solar irradiation. As can be seen, when a solar irradiation change is made, the PV current decrease enough as illustrated in Fig. 6.9 (b) also reducing the input PV power as presented in Fig. 6.9 (c). For that reason, the PV voltage decreases until reach the new MPP, and oscillate around the $v_{pv_{mp}}$ given by the tracking algorithm. As also can be seen from the figure, it shows the voltage at the dc-link side v_{dc}, the PV side v_{pv} and the compensated by the converter v_{pc} in Fig. 6.9 (a). In order to show them in the same figure with an appropriate resolution of scale, an offset value was included. As can be seen, v_{pv} is the addition between the v_{pc} and v_{dc}, which means that a voltage reduction is required to reach the value for the grid-connection, which is lower than in a traditional FPC $v_{pc} \approx 120V$. On the other hand, when the irradiation change is produced, the voltage decrease in order to reach the new MPP and it produced a reduction of v_{pc} which is translated to a lower converter voltage gain.

In contrast with the Step-Up configurations, the input current does not present a ripple reduction. It is because the input current I_{in} is the difference between the output current I_o, and the current flowing trough the diodes I_{pc}.

Table 6.3: Simulation parameters of the Step-Down II Full-bridge based PPC.

Parameter	Symbol	Value	Parameter	Symbol	Value
PV power	P_{pv}	$4500W$	Voltage Kp	K_{pv}	0.05104
PV voltage	$V_{pv_{mp}}$	$480V$	Voltage Ki	K_{iv}	750.9
PV side capacitance	C_{pv}	$330\mu F$	Current Kp	K_{pi}	-0.01504
Dc side capacitance	C_{dc}	$330\mu F$	Current Ki	K_{ii}	5010.9
Transformer turns ratio	n_T	8	Voltage step	Δ_v	7.5
Switching frequency	f_{sw}	$80kHz$	Time step	Δ_t	1.0
Resistive load	R_{dc}	20Ω	Inductance	L	$1\mu H$
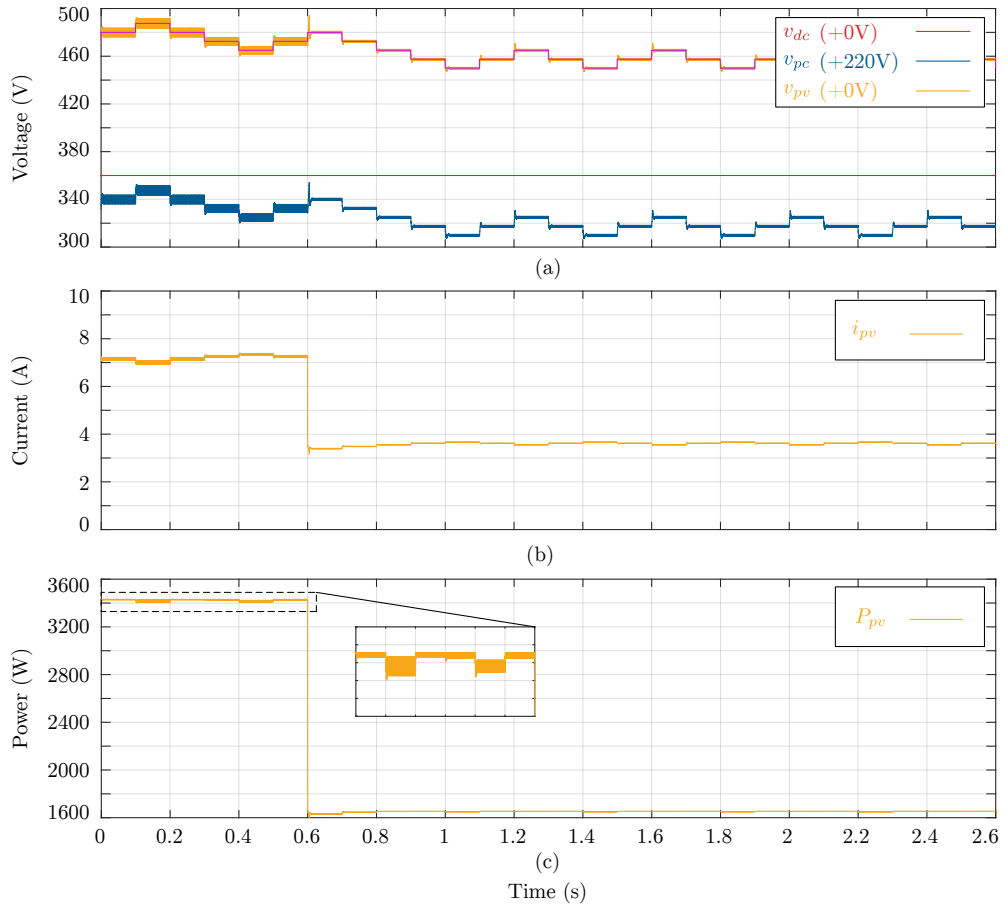
Figure 6.9: Results of the MPPT algorithm of the Step-Down II Full-bridge based PPC. (a) Voltage results. (b) PV current. (c) PV power.

As can be observed in Fig. 6.10, the current i_{pc} presents a continuous waveform due to the presence of the inductor connected with the diodes. Considering that the input current i_{in} is commutated, then the output current also presents the same commuted waveform. In that case it is possible to see that the current flowing through the diodes and the inductor is the lowest i_{pc}, it leads to the advantage to reduce the filter size and also the current rating of the diodes bridge.

The power waveforms are depicted in Fig. 6.11 (a), it is possible to note that the converter is handling a lower power ($P_{pc} < P_{pv}$). Although a solar irradiation change is made, the converter stills handling lower than the input power. In Fig. 6.11 (b) the partial power ratio K_{pr} is shown. Notice that after
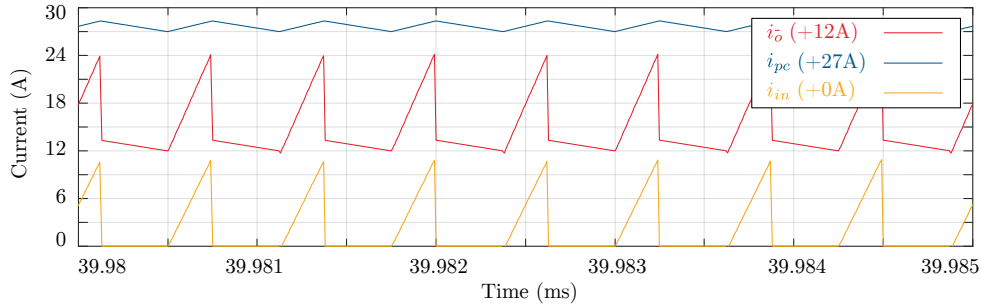
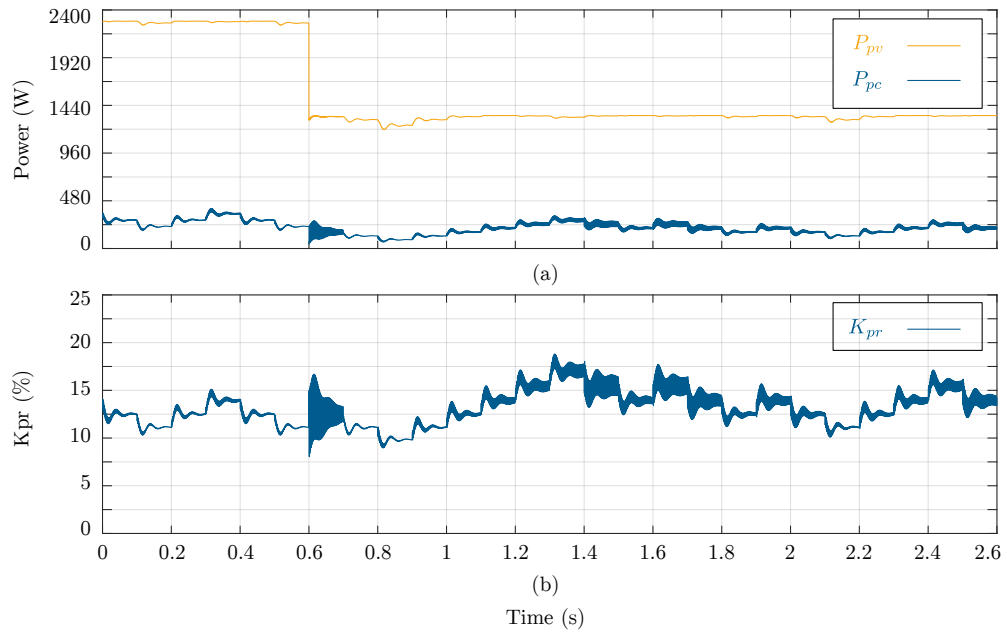Figure 6.10: Currents in the Step-Down II Full-bridge based PPC with $D = 0.63$.
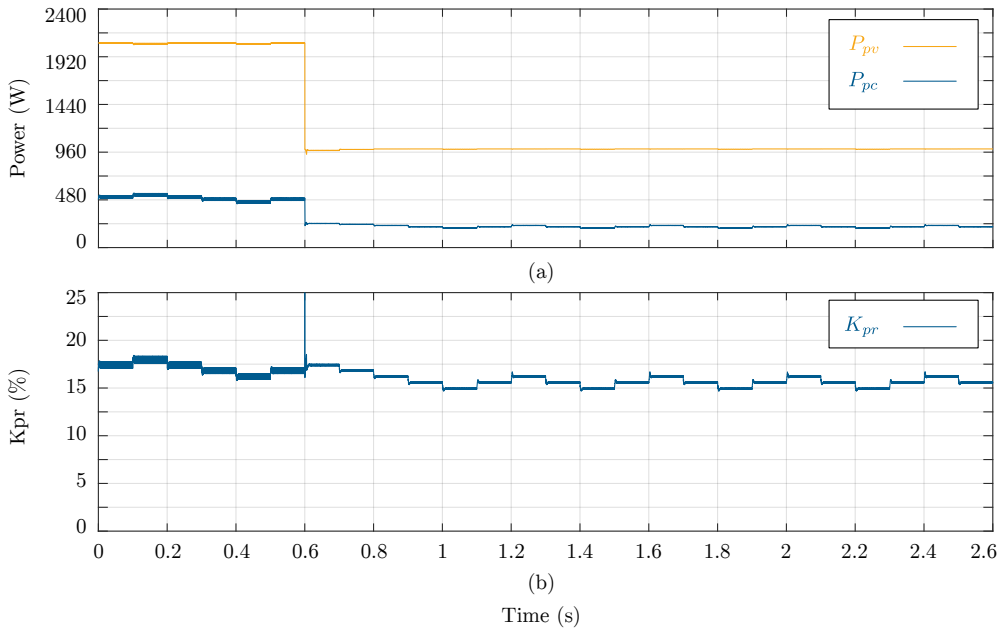
Figure 6.11: (a) PV power and power processed by the converter under solar irradiation changes. (b) Partial power ratio K_{pr} under solar irradiation changes.

the solar irradiation change, K_{pr} increase but without getting handle the entire input power. Based on this results it is worth concluding that the converter can be designed to operate at nominal values, so that despite of the increment on the K_{pr} value caused by the irradiation changes, it will not handle more than the rated power.

In order to obtain the PV voltage variation at different irradiation values, the explicit PV voltage expression is implemented. As can be seen in (1.1.14), the PV voltage can be expressed as a explicit function of the PV current using
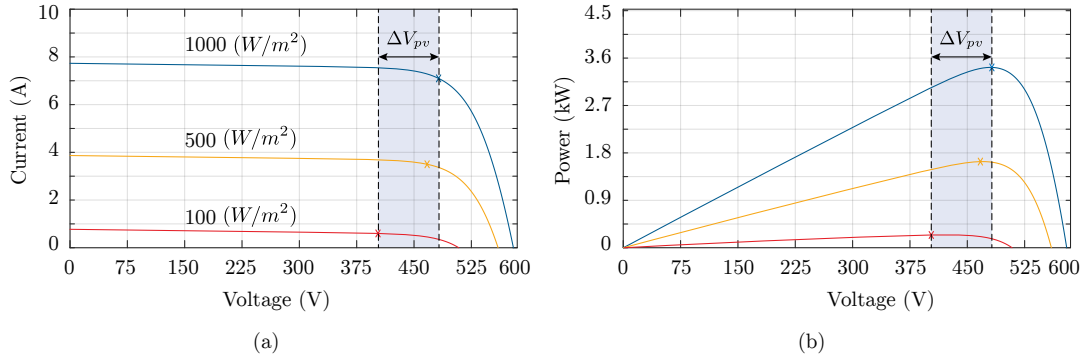
Figure 6.12: PV curves obtained with explicit expression using Lambert's function. (a) I-V PV curve. (b) P-V PV curve.

Lambert's function. Working with a traditional PV module, the parameters are listed in Table 1.1, and the results are illustrated in Fig. 6.12 for the PV string. In that evaluation case, the voltage variation from $(1000 - 500W/m^2)$ corresponds to $\Delta V_{pv} = 12V$ and $K_{pr} = 15.5\%$. That is the reason to explain the small variation in the $\Delta K_{pr} = 2\%$ parameter.

Finally, in order to evaluate the the maximum variation of the partial power ratio, a irradiation change between $(1000 - 50W/m^2)$ is made as presented in Fig. 6.12. In that case, the voltage changes $\Delta V_{pv} = 100.5V$ from the v_{pv} at STC. Moreover, when the irradiation decrease the partial power ratio decreases to $K_{pr} = 5.4\%$. However, with this design the converter cannot work because it requires a duty cycle lower than 0 to reduce the voltage. For that reason in order to achieve this level of reduction, a higher turns ratio is needed. The more deep reduction is needed, the more higher turns ratio is required. Without changing the parameters, the minimum $K_{pr_{min}} = 12\%$ to keep the control performances over the converter. Nevertheless, it shows that in difference with the Step-Up configurations, the Step-Up II PPC allows a reduction of the K_{pr} when solar irradiation decreases.

6.4   Summary and Conclusion

In this chapter some simulation results were presented using different PPC configurations. They were evaluated in some standard PV applications in order to make a first approach about the scope of the presented work. From the results depicted in this chapter, it is possible to highlight the PPC operation were only a fraction of the power is processed. The PPC configurations are evalu-

ated in different scenarios in order to show the control performance in terms of MPPT algorithm. Moreover, the improvement of the input current is also shown when Step-Up PPC are used, which can extend the lifespan of capacitors. When the solar irradiation changes, it is worth noticing the variation of the ratio of power handled by the converter. In the case of Step-Up PPC configurations, the higher voltage gain the higher power is processed by the converter. On the other hand, when Step-Down PPC are used the partial ratio decreases when solar irradiation also decreases.

In addition, the voltage explicit model of the PV current using Lambert's function is used, for evaluating the limits of the partial power ratio in terms of solar irradiation variations. Working with a commercial PV module (SunModule Sw 285) the maximum voltage variation is around the $\Delta V_{pv_{max}} = 20\%$, and a reduction of the 50% of solar irradiation produces a voltage variation around the $\Delta V_{pv} = 2.5\%$ of the nominal V_{pv} at STC. From the results the conclusion is that the PPC configurations are able to operate in partial mode in a wide voltage range. It demonstrates that the converters do not losses the PPC merits despite of variations in the PV system.

Chapter 7

EXPERIMENTAL VALIDATION

The experimental validation of the different PPC configurations comprises: the correct operation of the power topology used for the construction of the PPC, the functionally of converter evaluating the MPPT algorithm, the analysis of partial operation and the conversion efficiency. Among the PPC configurations analyzed and presented in the theoretical sections, only three converters are selected to be built and tested in the laboratory. The selection criteria was based on the ones which present more practical interest for PV systems.

It is worth noticing that the voltage and power ratings have been scaled from typical applications values to laboratory and components availability. The main reason is that the available HF transformers deprive of choosing traditional ratings for power and turn-ratio for the corresponding PV applications. Nevertheless, the theoretical analysis and validation still holds, because they are evaluated as power ratios, voltage gains and duty cycles.

The PV system, is emulated with the programmable dc-Power Supply Chroma 62050H-600S with Solar Array Simulator (600V/5kW). The Flyback based PPC is chosen to validate the Step-Up I PPC configuration, and two Full-bridge based PPCs are made to validate the Step-Up II and Step-Down II configurations. The control platform is composed by a dSPACE 1103 controlling the dc-dc converters, a FPGA Spartan-3E generating the HF PWM signals, and an interface board between the dSPACE and the FPGA as depicted in Fig. 7.1. The PPC is used to perform MPPT algorithm controlling the input voltage, and the output voltage is fixed by the dc-Power Supply Agilent N8762A Technologies (600V/8.5A). The power delivered by the PV system is dissipated in a resistive load. The differential voltage measuring probe used in the test-bench is the Keysight N2790A, 100MHz. Finally, the currents are measured using the probe Keysight N2783B, 100MHz.
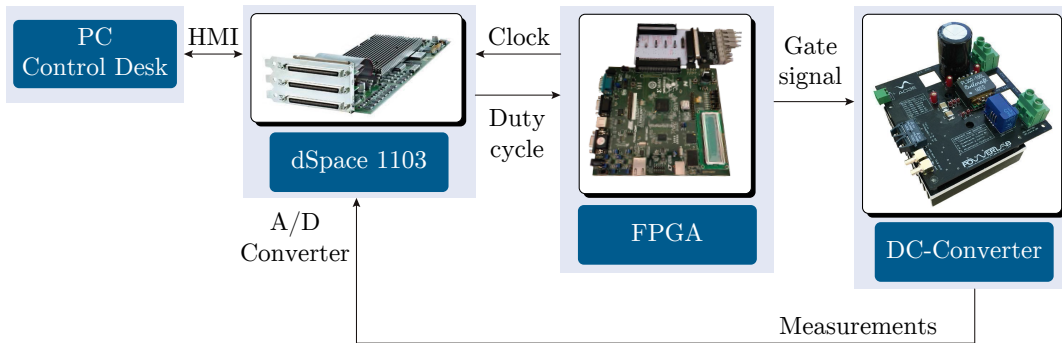
Figure 7.1: Communication diagram and control platform of the experimental test-bench.

7.1   Step-Up I Flyback based Partial Power Converter

The Flyback topology is widely used in applications handling small power ($< 300W$), for that reason it is commonly found in microinverter systems [5]. Moreover, some commercial microinverters like Enphase Energy [60], currently commercialized by Siemens, work with interleaved connections at input and output side. Interleaved converters are widely used among power electronic applications. Such configurations can be adopted for different reasons in view of the features and benefits of the interleaved scheme. The two main advantages are:

- Distribution of the power among several converters, then allowing to reduce the power rating of the individual converters;

- Ripple reduction at the input and/or output of the converter when phase shifted carriers are used in the modulation, then allowing reduction in the filters size.

An additional advantage is the possibility of obtaining higher conversion ratio if input-parallel output-series (IPOS) or input-series output-parallel (ISOP) schemes are adopted [65]. On the other hand, the main drawback is the increase in number of the power converters required in interleaved configurations. Similar features as the classical interleaved operation of two converters are obtained working with a single Step-Up I Flyback based PPC. More precisely, it operates as the input-parallel output-series (IPOS) configuration, reducing the current ripple at the input of the system and dividing the individual converters power rating.
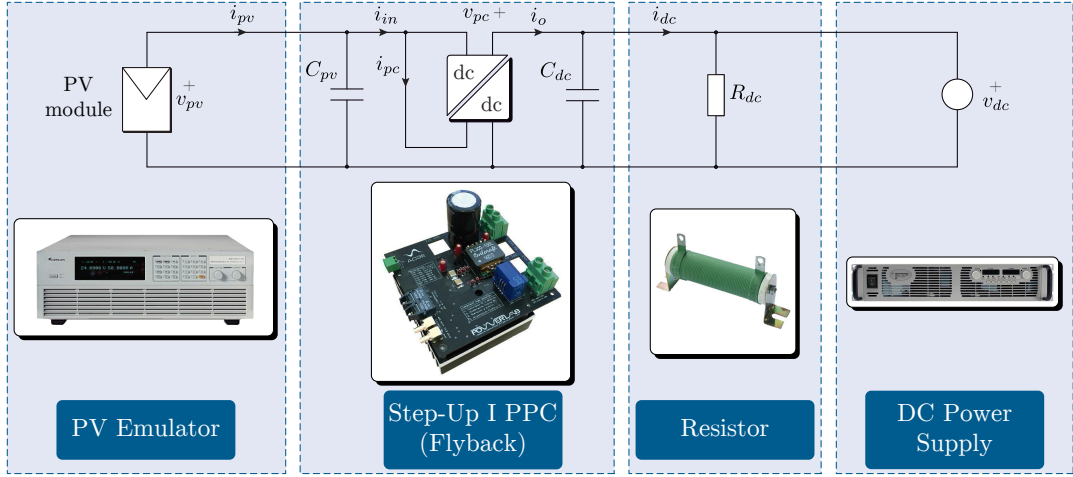
Figure 7.2: Circuit diagram of the experimental test-bench for the Step-Up I Flyback based PPC.

The experimental test-bench, built to validate the configuration, is shown in Fig. 7.2. The topology used for the PPC is the Flyback converter, which is illustrated in Fig. 7.3. The parameters of the experimental test-bench are listed in Table 7.1.

Firstly, the Step-Up I Flyback based PPC was tested without the clamping circuit. Measured currents are shown in Fig. 7.4 for the converter working with a duty cycle $D = 0.48$. In this figure, it can be seen that the resulting input current i_{in} shows a continuous waveform with reduced ripple. It comes from the connection used for making the PPC configuration so that, both the current flowing by the Mosfet and the diode are commutated, but they are also

Table 7.1: Parameters of the Step-Up I Flyback based PPC.

Parameter	Symbol	Value
PV power	P_{pv}	$110W$
PV voltage	V_{pv}	$28V$
PV side capacitance	C_{pv}	$10\mu F$
Clamping capacitance	C_c	$5\mu F$
Dc side capacitance	C_{dc}	$1000\mu F$
Transformer turns ratio	n_T	1
Switching frequency	f_{sw}	$200kHz$
Resistive load	R_{dc}	9Ω
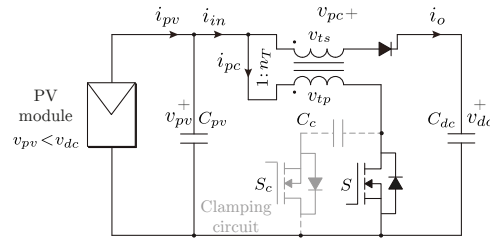
Figure 7.3: Configuration of the experimental Step-Up I Flyback based PPC.
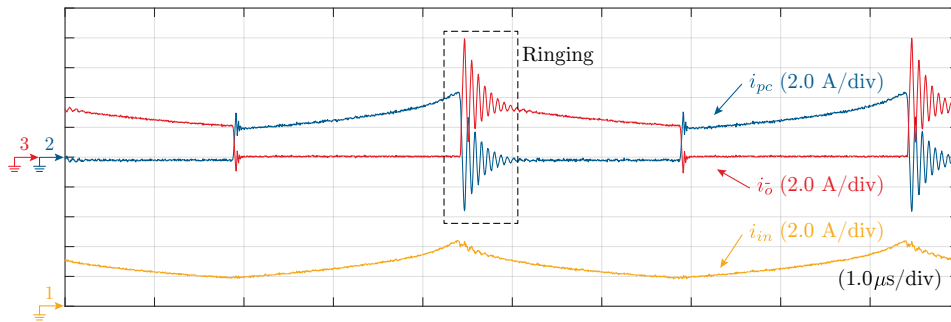
Figure 7.4: Current measurements in the Step-Up I Flyback based PPC without the clamping circuit and $D = 0.48$.

opposites each other which allows this mitigation of the commutation effect.

It can be considered as an advantage so that the input capacitor is also reduced, allowing the using of ceramic capacitors and leading into a small circuit board. However, in the figure it can also been observed the presence of an important ringing effect when the main switch turns off. This effect is due to the presence of parasitic elements in the circuit, combined with the fast rise and fall times of the devices working at the frequency $f_{sw} = 200kHz$. Such phenomenon is not desirable since it implies high stress in the devices resulting in higher losses.

In order to mitigate the ringing effect, a clamping circuit as represented in Fig. 7.3 is used. Moreover, the converter has also been verified for a duty cycle $D = 0.28$, as presented in Fig. 7.5. As the figure shows, the input current i_{in} is continuous despite of the effect of adding the clamping circuit. And this is the major advantage in contrast to the traditional IPOS configuration operating with a duty cycle lower than 0.5. So that in the traditional IPOS configuration made with Flyback converters, the input current i_{in} is discontinuous for duty cycle lower than 0.5.
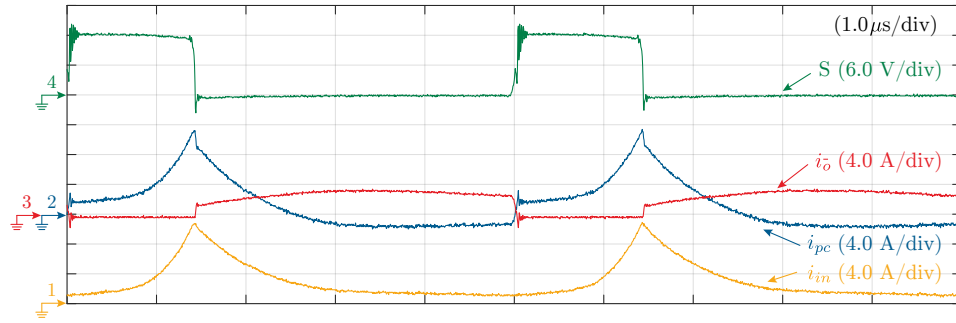
Figure 7.5: Current measurements in the Step-Up I Flyback based PPC with the clamping circuit and $D = 0.28$.
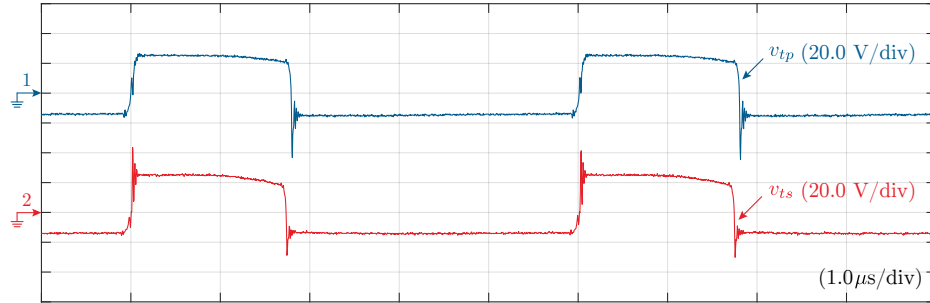
Figure 7.6: Transformer voltages in the Step-Up I Flyback based PPC.

In order to eliminate the effect of the discontinuity and ripple mitigation in the input current i_{in}, the transformer turns ratio must have the same value for the primary and secondary side $n_T = 1$. The waveform is depicted in Fig. 7.6, where it is possible to see that both the voltage at the primary and secondary side are the same.

Under constant solar irradiation the parameters evaluated are the voltage and current in the system. The voltages are shown in Fig. 7.6, where the P&O MPPT algorithm presents the classical three levels. In traditional PV applications the voltage at the dc-link v_{dc} is fixed by the inverter, then due to the series connection of the PPC, the converter voltage v_{pc} is the difference between v_{dc} and v_{pv}.

In the case of the currents it is worth to notice that the waveform also varies depending on the MPPT algorithm as illustrated in Fig. 7.8. The current oscillates around the maximum power but, when the voltage increase looking for the mpp, the current decrease considerably. It is because the operation point
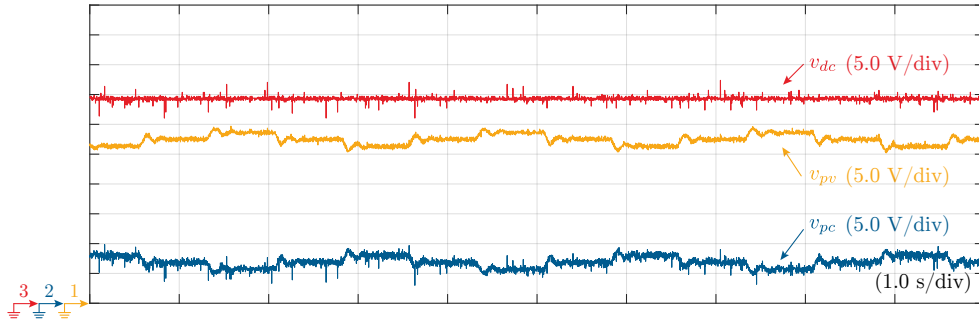
Figure 7.7: Voltage waveforms in the Step-Up I Flyback based PPC under constant solar irradiation.
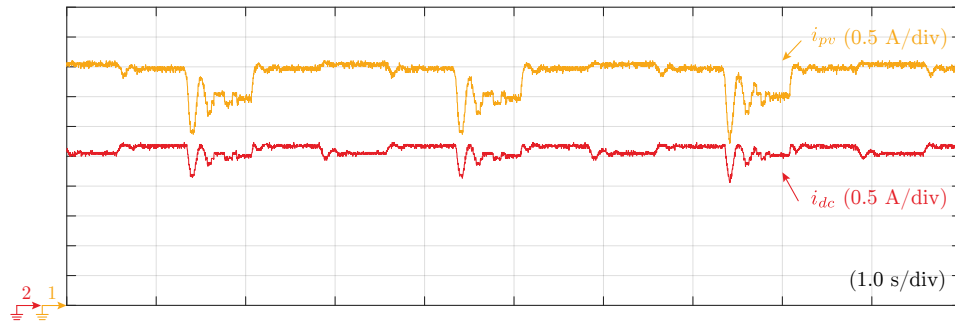
Figure 7.8: Current waveforms in the Step-Up I Flyback based PPC under constant solar irradiation.

is located on the PV region where the small variations on voltage correspond to high variations on the current.

Moreover, in order to evaluate the performance of the MPPT algorithm, it is made an irradiation reduction to the 60% of the rated value. The result is presented in Fig. 7.9 and it is possible to see the current reduction when the change is made. Moreover, due to the implemented MPPT algorithm, the PV voltage decreases in order to find the maximum power point.

7.2 Step-Up II Full-bridge based Partial Power Converter

The experimental test-bench built to validate the Step-Up II PPC configuration is depicted in Fig. 7.10, and the topology used to evaluate the concept is shown in Fig. 7.11. It is based on an isolated Full-bridge topology, including an active clamping circuit to mitigate the ringing effect. The design is based on the
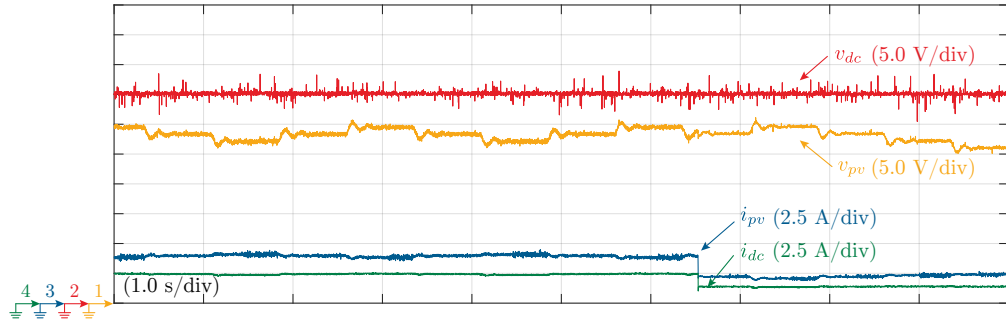
Figure 7.9: Voltage and current waveforms in the Step-Up I Flyback based PPC under a reduction of the solar irradiation.
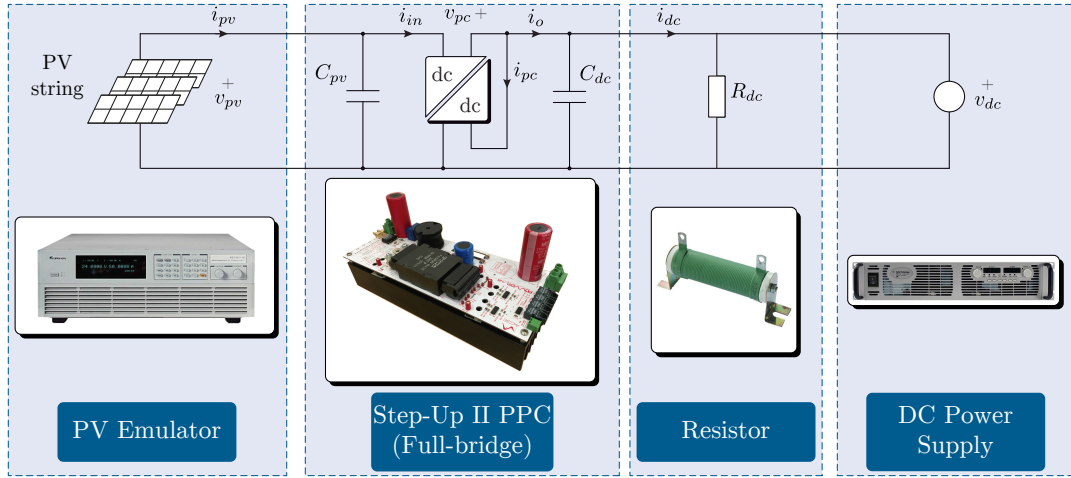
Figure 7.10: Circuit diagram of the experimental test-bench for the Step-Up II Full-bridge based PPC.

nominal values of the commercial high-frequency Payton Planar Transformer (60V/30A) at the primary side, turns ratio $n_1 : n_2 = 3 : 24$. The primary side of the transformer (Low Voltage LV) is connected to the diodes, and the secondary side (High Voltage HV) is connected to the Mosfet bridge. The parameters of the experimental test-bench are listed in Table 7.2.

One of the advantages working with the presented configuration is the reduction of the current ripple at the input side i_{in} because of the connection. Considering that the current flowing through the Diodes bridge is filtered by the inductance, and this is the sum between the converter current i_{pc} and the output current i_o. Then both currents present complementary waveforms further,
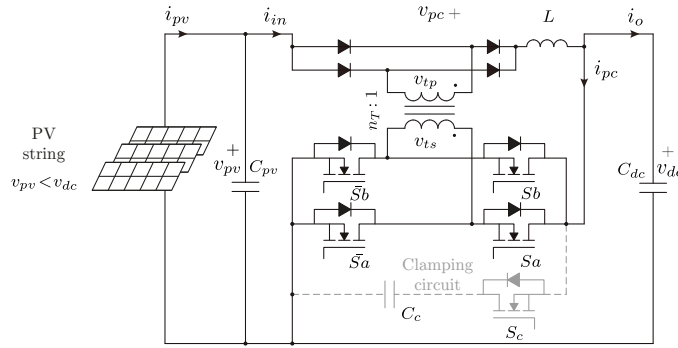
Figure 7.11: Configuration of the experimental Step-Up II Full-bridge based PPC.

the semiconductors can be sized for a lower current value so that for an input current $I_{in} = 5.2A$, the current flowing trough the Mosfets bridge is around $I_{pc} = 1.5A$. These results can be observed in Fig. 7.12, where the input current presents a ripple reduction if this is compared with a traditional Full-bridge full power converter, and the mean value is the lowest one.

The voltages at the transformer input and output side are illustrated in Fig. 7.13. In that case it is possible to see the similar waveforms with the ratio $V_{ts}/V_{tp} = 8$, which is given by the transformer turns ratio. However, it is worth to notice that the ringing at the Mosfet side HV is lower compared with the primary side LV. It is justified because the clamping circuit was placed in parallel with this bridge, and the filter inductance is series connected with the diodes.

Under constant solar irradiation the parameters evaluated are the voltage and current in the system. The voltages are presented in Fig. 7.13, where

Table 7.2: Parameters of the Step-Up II Full-bridge based PPC.

Parameter	Symbol	Value
PV power	P_{pv}	$1kW$
PV voltage	V_{pv}	$192V$
PV side capacitance	C_{pv}	$330\mu F$
Clamping capacitance	C_c	$47\mu F$
Dc side capacitance	C_{dc}	$330\mu F$
Transformer turns ratio	n_T	8
Switching frequency	f_{sw}	$80kHz$
Resistive load	R_{dc}	35Ω
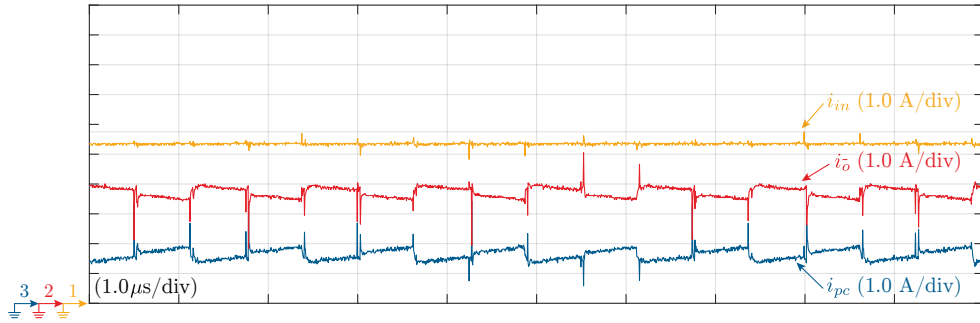
Figure 7.12: Current measurements in the Step-Up II Full-bridge based PPC with the clamping circuit and $D = 0.48$.
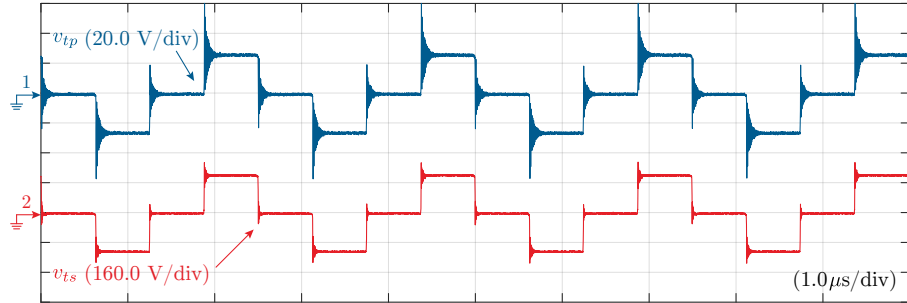
Figure 7.13: Transformer voltages in the Step-Up II Full-bridge based PPC.

the P&O MPPT algorithm presents the classical three levels. In traditional PV applications the voltage at the dc-link v_{dc} is fixed by the inverter, then due to the series connection of the PPC, the converter voltage v_{pc} is the difference between v_{dc} and v_{pv}. Note the step-up operation where the output voltage $V_{dc} = 200V$ is higher than the input voltage $V_{pv} = 190V$. Due to the connection, the partial converter voltage is $V_{pc} = 10V$, which is the voltage blocked by the diodes, and it is lower than the voltage blocked in a traditional FPC. These values represent the average value of the waveforms depicted in the figure.

In the case of the currents it is worth to notice that the waveform also varies depending on the MPPT algorithm as shown in Fig. 7.15. However, compared with the configuration presented before, the current oscillates around the maximum power but, it is not enough considerably. It is because the voltage steps are smaller compared with the rated PV voltage, it means that this variations are also small in the PV current. As is illustrated in the figure, the mean value of the currents are $I_{pv} = 5.5A$ and the output current $I_{dc} = 4.5A$.
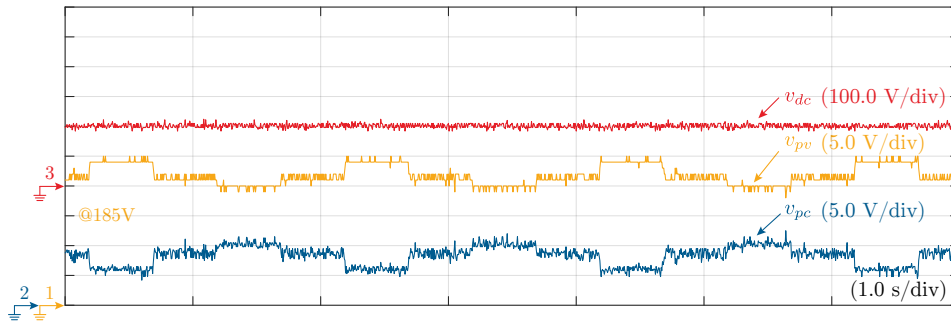
Figure 7.14: Voltage waveforms in the Step-Up II Full-bridge based PPC under constant solar irradiation.
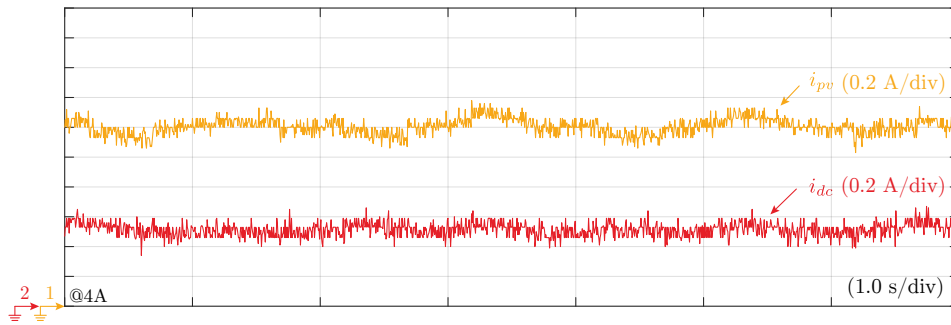
Figure 7.15: Current waveforms in the Step-Up II Full-bridge based PPC under constant solar irradiation.

Moreover, in order to evaluate the performance of the MPPT algorithm, it is made an irradiation reduction to the 55% of the rated value. The result is presented in Fig. 7.16 and it is possible to see the current reduction when the change is made. Moreover, due to the implemented MPPT algorithm, the PV voltage start decreasing the value in order to find the maximum power point.

7.3 Step-Down II Full-bridge based Partial Power Converter

The experimental test-bench built to validate the Step-Down II PPC configuration is depicted in Fig. 7.17, and the topology used to evaluate the concept is shown in Fig. 7.18. It is based on an isolated Full-bridge topology, including an active clamping circuit to mitigate the ringing effect. The design is based on the nominal values of the commercial high-frequency Payton Planar Trans-
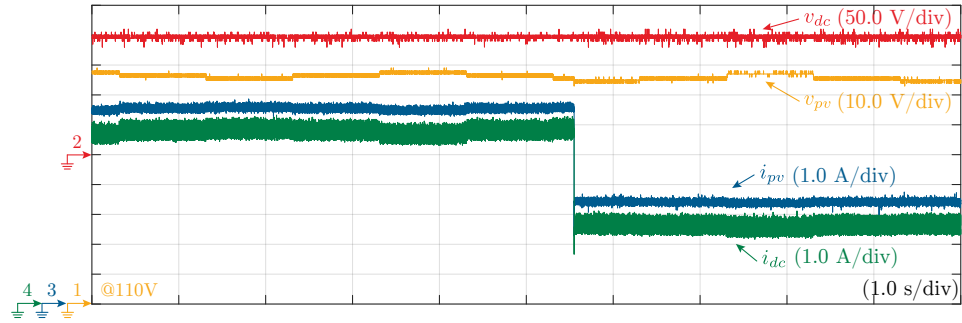
Figure 7.16: Voltage and current waveforms in the Step-Up II Full-bridge based PPC under a reduction of the solar irradiation.
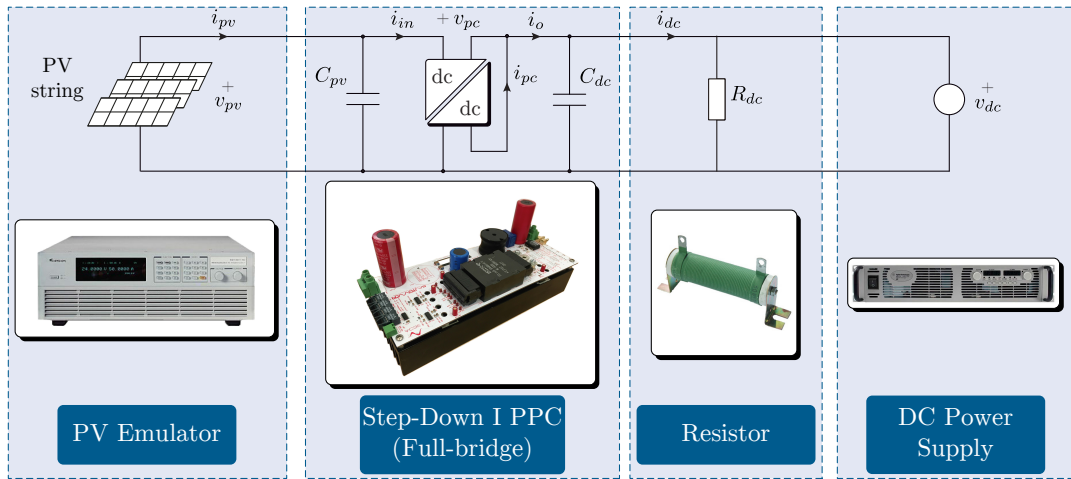
Figure 7.17: Circuit diagram of the experimental test-bench for the Step-Down II Full-bridge based PPC.

former (60V/30A) at the LV side, turns ratio $n_1 : n_2 = 3 : 24$. In that case, the LV side is connected to the Mosfet bridge, and the HV side is connected to the Diodes. The parameters of the experimental test-bench are listed in Table 7.2.

In contrast with the Step-Up configurations, the input current does not present a ripple reduction. It is because the input current $I_{in} = 5.78$ is the difference between the output current $I_o = 6.9$, and the current flowing trough the diodes $I_{pc} = 1.12$. As can be observed in Fig. 7.19, the current i_{pc} presents a continuous waveform due to the presence of the inductor connected with the diodes. Considering that the input current i_{in} is commutated, then the output current also presents the same commuted waveform. In that case it is possible
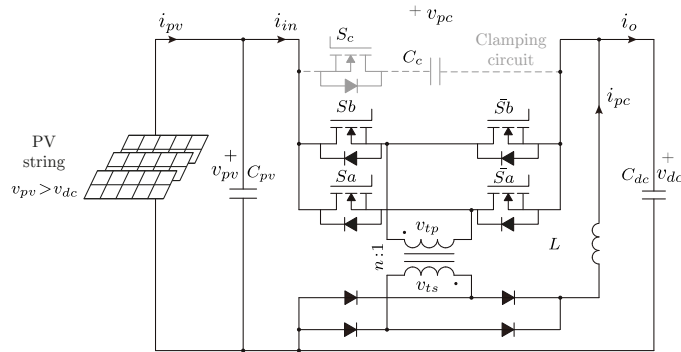
Figure 7.18: Configuration of the experimental Step-Down II Full-bridge based PPC.

to see that the current flowing through the diodes and the inductor is the lowest i_{pc}, it leads to the reduction of the filter size and also the current rating of the diodes bridge.

The voltages at the transformer input and output side are illustrated in Fig. 7.20. In that case it is possible to see the similar waveforms with the ratio $V_{ts}/V_{tp} = 8$, which is given by the transformer turns ratio. However, it is worth to notice that the ringing at the Mosfet side LV is lower compared with the secondary side HV. It is justified because the clamping circuit was placed in parallel with this bridge, and the filter inductance is series connected with the diodes.

Under constant solar irradiation the parameters evaluated are the voltage and current in the system. The voltages are presented in Fig. 7.20, where the P&O MPPT algorithm presents the classical three levels. In traditional PV applications the voltage at the dc-link v_{dc} is fixed by the inverter, then due

Table 7.3: Parameters of the Step-Down II Full-bridge based PPC.

Parameter	Symbol	Value
PV power	P_{pv}	$1.2kW$
PV voltage	V_{pv}	$230V$
PV side capacitance	C_{pv}	$330\mu F$
Clamping capacitance	C_c	$47\mu F$
Dc side capacitance	C_{dc}	$330\mu F$
Transformer turns ratio	n_T	8
Switching frequency	f_{sw}	$80kHz$
Resistive load	R_{dc}	28Ω
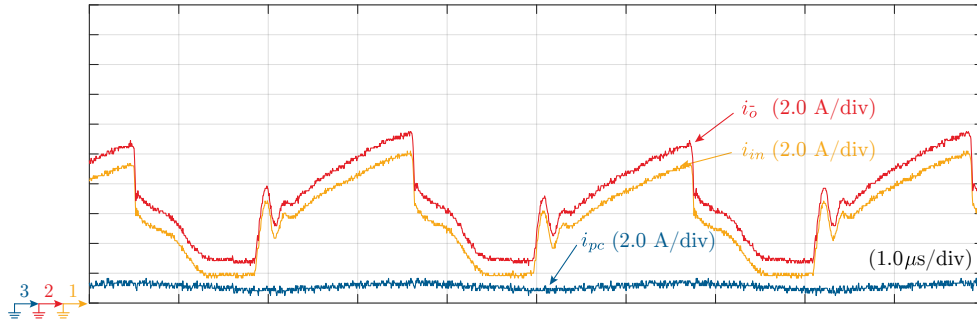
Figure 7.19: Current measurements in the Step-Down II Full-bridge based PPC with the clamping circuit and $D = 0.6$.
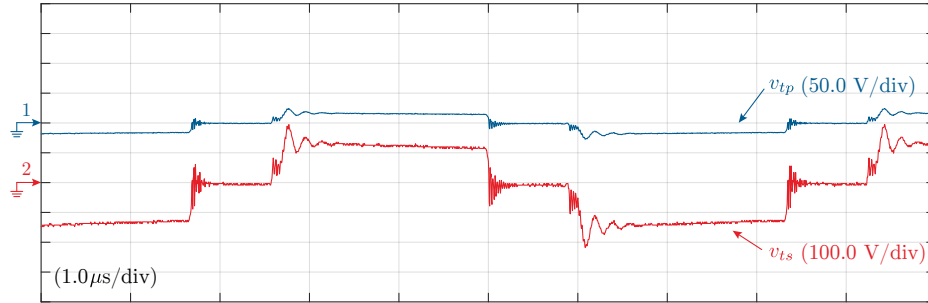
Figure 7.20: Transformer voltages in the Step-Down II Full-bridge based PPC.

to the series connection of the PPC, the converter voltage v_{pc} is the difference between v_{pv} and v_{dc}. In that case the step-down operation is noted by the measurements, where the output voltage $V_{dc} = 167V$ is lower than the input voltage $V_{pv} = 230V$. Due to the connection, the partial converter voltage is $V_{pc} = 63V$, which is the blocking voltage withstood by the Mosfets, and it is lower than in the case of traditional FPC. These values represent the average value of the waveforms depicted in the figure.

In the case of the currents it is worth to notice that the waveform also varies depending on the MPPT algorithm as shown in Fig. 7.22. However, compared with the Step-Up I PPC configuration, the current oscillates around the maximum power but, it is not enough considerably. It is because the voltage steps are smaller compared with the rated PV voltage, it means that this variations are also small in the PV current. The important feature is that for the same design used also in the Step-Up II PPC , the input current presents a higher ripple. The reason is that this PPC configuration does not present the advantage
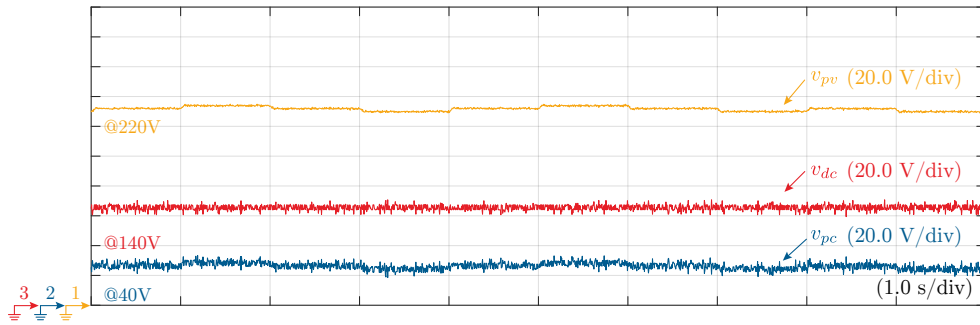
Figure 7.21: Voltage waveforms in the Step-Down II Full-bridge based PPC under constant solar irradiation.
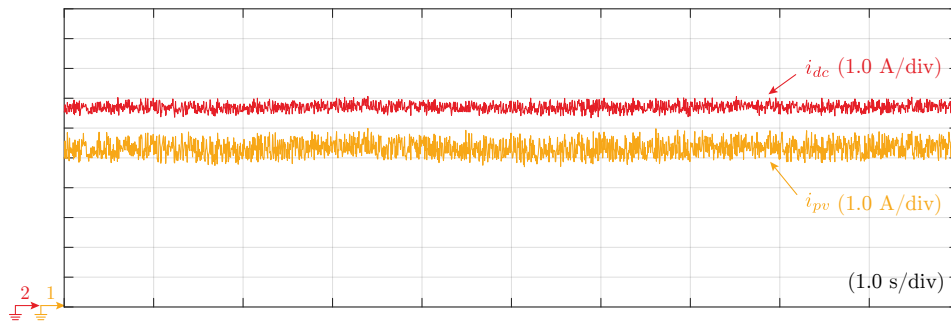
Figure 7.22: Current waveforms in the Step-Down II Full-bridge based PPC under constant solar irradiation.

of input current ripple reduction as was explained before. Regarding with the measurements, the mean value of the currents are $I_{pv} = 5.3A$ and the output current $I_{dc} = 7A$.

Moreover, in order to evaluate the performance of the MPPT algorithm, it is made an irradiation reduction to the 67% of the rated value. The result is illustrated in Fig. 7.23 where it is possible to see the current reduction when the change is made. Moreover, due to the implemented MPPT algorithm, the PV voltage start decreasing the value in order to find the maximum power point. The stationary value is around $V_{pv} = 225V$.

7.4 Analysis of Efficiency

In order to obtain the experimental efficiency, the power is calculated using the modulated and sampled values of voltage and current (neglecting the high-
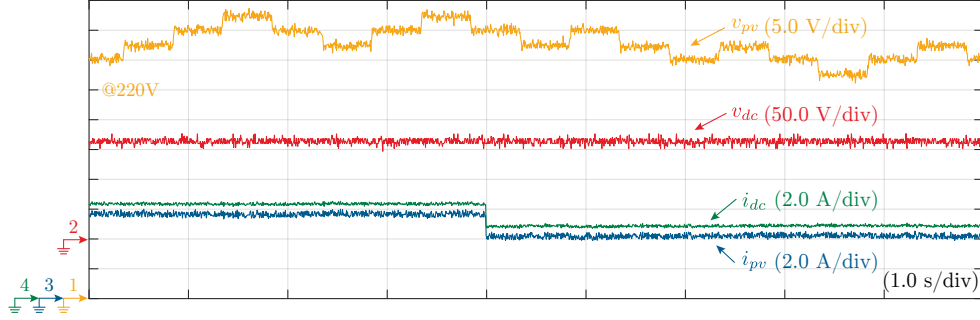
Figure 7.23: Voltage and current waveforms in the Step-Down II Full-bridge based PPC under a reduction of the solar irradiation.

frequency of commutation). The measurements are taken from the whole power conversion system (PPC configuration), and the isolated dc-dc converter used to make the configuration (Flyback and Full-bridge). These measurements are made for the Step-Up and Step-Down configurations.

Step-Up I Flyback based PPC

Considering the Step-Up I configuration, the experimental efficiency waveforms are presented in Fig. 7.24. The global conversion efficiency of the dc-stage, based on the measurements at the output side (I_o, V_{dc}) and the input side (I_{pv}, V_{pv}), is obtained under different power and partial power ratios K_{pr}. When the converter is operating below $K_{pr} \leq 80\%$ of the total power, the global conversion efficiency varies between $70\% \sim 90\%$, as depicted in Fig. 7.24 (a). On

Table 7.4: Experimental evaluation points

Parameters	Step-Up I	Step-Up II	Step-Down II
System Power (W)	99	821	822
Dc-dc Power (W)	19.8	52.5	110.1
$K_{pr}(\%)$	20	6.4	13.4
PV voltage (V)	27.9	190.4	182
Dc-link voltage (V)	32.7	200	153
Converter voltage (V)	4.8	9.6	47
Global Voltage gain G_v	1.17	1.05	0.84
Dc-dc Voltage gain G_{vc}	0.15	20.83	0.31
Dc-stage efficiency η_{dc_s} (%)	90	98.5	97.5
Dc-dc efficiency $\eta_{dc_c}(\%)$	59	82	78.9

(a)

(b)

Figure 7.24: Curve of experimental efficiency: (a) Total power conversion system. (b) Isolated dc-dc converter in the Step-Up I Flyback based PPC.

the other hand, the conversion efficiency of the dc-dc converter varies between $35\% \sim 77\%$, as shown in Fig. 7.24 (b) where it is possible to note the experimental points obtained from measurements and the curve fitting. This can be understood in the sense that the Flyback converter is handling a low power, in comparison for which it was designed. Moreover, considering that the configuration is oriented to microinverter applications, the total voltage gain will be high because of the low PV voltage. It leads to understand that in that case, the global conversion efficiency is highly dependent of the dc-dc converter efficiency.

Nevertheless, in order to enhance the analysis of efficiency, Table 7.4 illustrates an experimental operating point for the configuration. As can be seen, the PV system is rated at $P_{pv} = 99W$ but it is handling a $K_{pr} = 20\%$ of the total power. The partial power ratio K_{pr} is related to the global voltage gain, which is $G_v = 1.17$. However, due to the series connection, the voltage at converter side is very small $V_{pc} = 4.8V$, which leads to a high voltage gain for the isolated Flyback dc-dc converter $G_{vc} = 0.15$. That is the reason because of the low efficiencies reached with the Flyback converter. However, from the point of view of the whole system it is not a problem when the partial ratio is low, because the dc-dc converter is handling a low power. Therefore, the power loss related to the dc-dc conversion is $P_{dc,l} = 8.12W$, which represents the 8.2% of the global system losses.

Moreover, as can be realized the dc-dc converter works as buck converter

Figure 7.25: Curve of experimental efficiency: (a) Total power conversion system. (b) Isolated dc-dc converter in the Step-Up II Full-bridge based PPC.

despite of the step-up operation. It means that the topology operation does not define the operation of the PPC configuration. For that reason, for this application it is important to select a topology with a buck-boost operation in order to compensate the required compensated voltage v_{pc}. That is also the reason to justify the selection of the Flyback instead of the Full-bridge topology as the suitable solution for this application, so that with a turns ratio $n_T = 1$ the voltage gain is not limited because of the inherent buck-boost operation.

Step-Up II Full-bridge based PPC

The experimental efficiency waveforms for the Step-Up II configuration, are illustrated in Fig. 7.25. In the measured range, with the converter operating below $K_{pr} \leq 10\%$ of the total power, the global conversion efficiency varies between $98\% \sim 99\%$, as presented in Fig. 7.25 (a). On the other hand, the conversion efficiency of the dc-dc converter varies between $70\% \sim 94\%$, as depicted in Fig. 7.25 (b) where it is possible to note the experimental points obtained from measurements and the curve fitting. This can be understood in the sense that the Full-bridge converter is handling a very low power, in comparison for which it was designed. Moreover, in order to enhance the analysis of efficiency, Table 7.4 illustrates an experimental operating point.

As can be seen in that case, the PV system is rated at $P_{pv} = 821W$ but it is handling $K_{pr} = 6.4\%$ of the total power. As was explained before, the partial power ratio K_{pr} is related to the global voltage gain, which is $G_v = 1.05$.
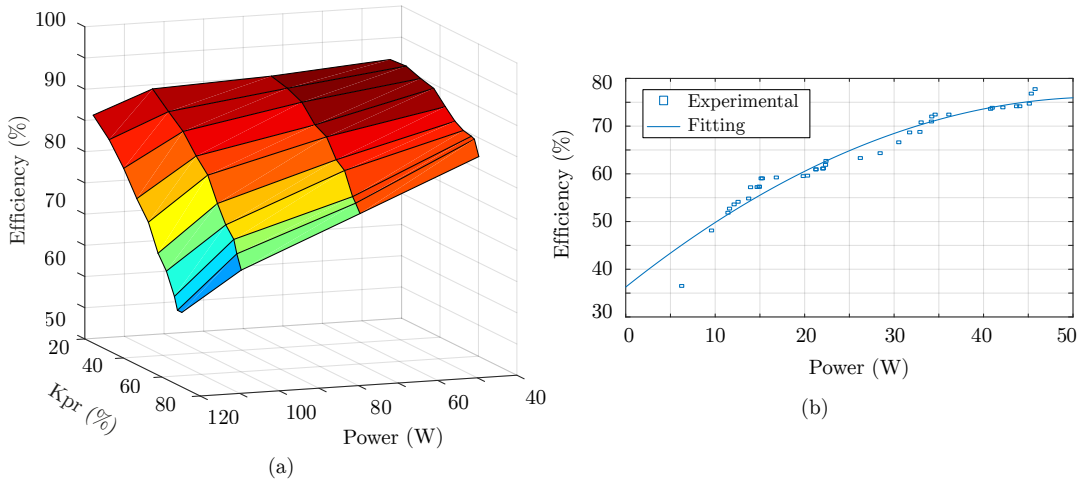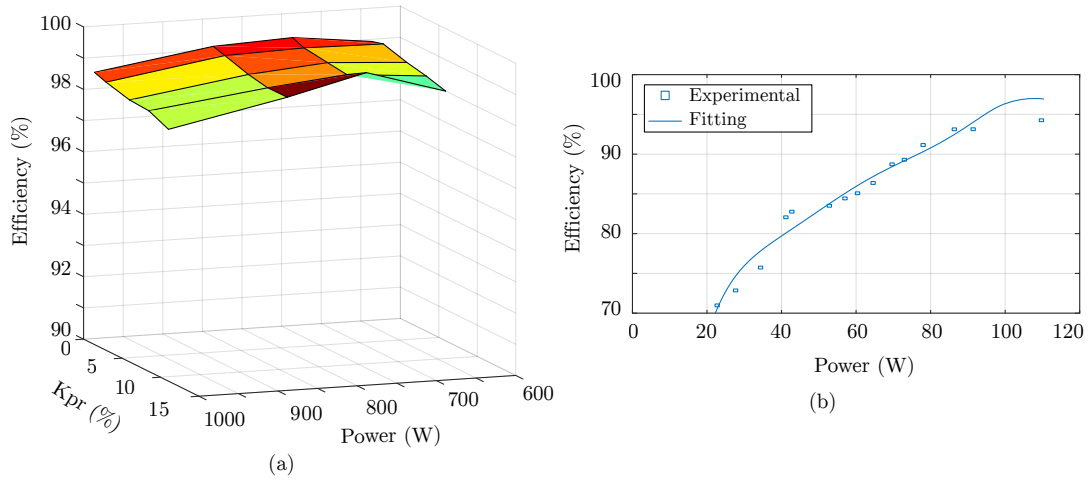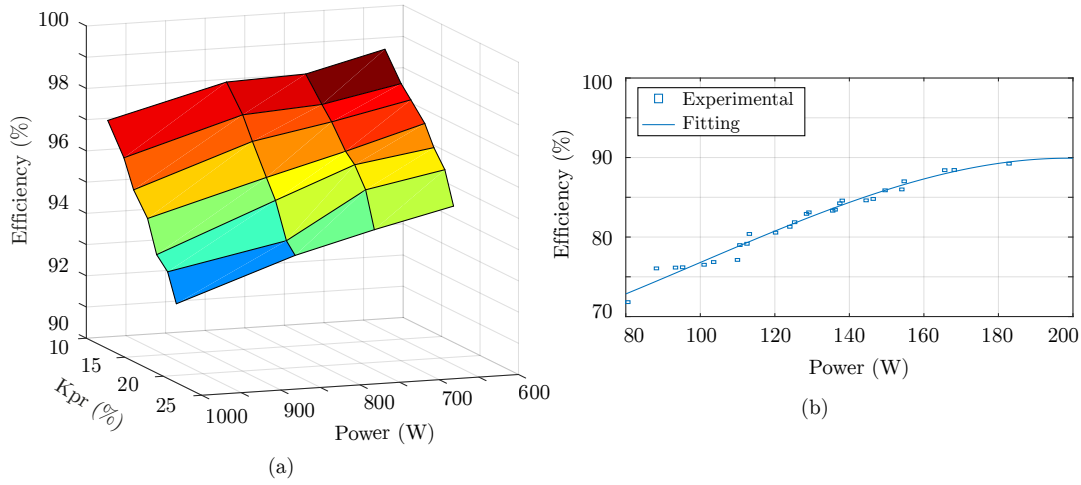
Figure 7.26: Curve of experimental efficiency: (a) Total power conversion system. (b) Isolated dc-dc converter in the Step-Down II Full-bridge based PPC.

However, due to the series connection, the voltage at converter side is very small $V_{pc} = 9.6V$, which leads to a high voltage gain for the isolated Full-bridge dc-dc converter $G_{vc} = 20.83$. That is the reason behind the low efficiency reached by the Full-bridge converter. However, it does not represent a problem for the whole system, due to the low power the converter is handling. Therefore, the power loss related to the dc-dc conversion is $P_{dc,l} = 9.45W$, which represents the 1.15% of the global system losses.

Step-Down II Full-bridge based PPC

The same analysis is made for the Step-Down II configuration, and the experimental efficiency waveforms are shown in Fig. 7.26. In the measured range, with the converter operating below $K_{pr} \leq 25\%$ of the total power, the global conversion efficiency varies between $90\% \sim 99\%$, as illustrated in Fig. 7.26 (a). On the other hand, the conversion efficiency of the dc-dc converter varies between $72\% \sim 93\%$, as presented in Fig. 7.26 (b).

   As it can be seen in the Table 7.4, the PV system is rated at $P_{pv} = 822W$ but it is handling $K_{pr} = 13.4\%$ of the total power. In that case, the global voltage gain is $G_v = 0.84$. Nevertheless, due to the series connection the voltage at converter side is $V_{pc} = 47V$, which leads to a different voltage gain for the isolated Full-bridge dc-dc converter $G_{vc} = 0.31$. This deep step-down operation impacts the efficiency reached by the Full-bridge converter itself, which is relatively low. Therefore, the power loss of the dc-dc conversion is $P_{dc,l} = 23.23W$,
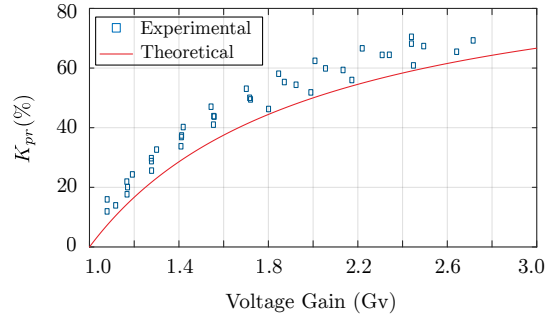
Figure 7.27: Experimental partial power ratio for the Step-Up I Flyback based PPC.

which represents 2.83% of the global system losses.

7.5 Analysis of the Partial Power Ratio

In order to evaluate the ratio of power processed by the converter, the voltage and current are measured at the Mosfet bridge, and the mean value is multiplied in order to obtain the converter power P_{pc}. Then, it is divided by the input power P_{pv} in order to obtain the partial power ratio K_{pr}. The experimental results are shown with points and the theoretical value is shown with a continuous line.

The experimental result for the Step-Up I Flyback based PPC is depicted in Fig. 7.27. It is possible to notice the increase of K_{pr} when the voltage gain is also increasing. The behavior fits with the theoretical result in (4.1.8). Nevertheless, it presents a small bias but it can be explained in the sense that the theoretical analyzed was made considerer a global efficiency $\eta_{dc_s} = 1$. Nevertheless, the important fact is the validation of the dependence between the voltage and gain and the power processed by the converter.

Considering the Step-Up II Full-bridge based PPC, the experimental result is shown in Fig. 7.28. It is possible to notice the linear increase of K_{pr} when the voltage gain also increases. The behavior fits with the theoretical result in (4.1.18). Nevertheless, it presents a small bias but it can be explained in the sense that the theoretical analyzed was also made considerer a global efficiency $\eta_{dc_s} = 1$. In this case, the voltage gain was not evaluated until reach a higher value, it is because the converter is oriented to PV applications with a large number of PV modules per string. So that they will be sized close to the dc-link voltage and the PPC converter will only compensate the variations produced by the MPPT algorithm, or the solar irradiation changes.
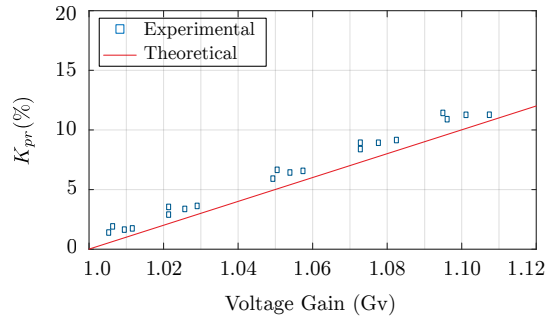
Figure 7.28: Experimental partial power ratio for the Step-Up II Full-bridge based PPC.

Finally, the experimental result for the Step-Down II Full-bridge based PPC is illustrated in Fig. 7.29. It is possible to notice the linear reduction of K_{pr} when the voltage gain increases. The behavior fits with the theoretical result in (4.2.14). Nevertheless, in contrast with the configurations discussed before, it does not present the bias between the theoretical and experimental results. It is because the converter is processing the input current i_{pv} (without considering the losses in the input capacitor C_{pv}), which is flowing directly form the PV side. It is the difference with the Step-Up PPC configurations, where the current processed by the converters is i_{pc} which represents the difference between i_{in} and i_o measured in the node of connection. In this case, the voltage range was extended in order to show the advantage of the configuration. Considering that the PV application is sized to a higher value compared with the dc-link voltage, the input voltage v_{pv} will be reduced in case of a reduction of the solar irradiation. It means, that the converter will handle a lower power in case of changes of atmospheric variations.

7.6   Summary and Conclusion

In this chapter the experimental results of the PPC configurations built in the laboratory were presented. It is important to highlight that the laboratory prototypes were not optimized in their design in terms of efficiency for the power rating in which they operate. They were designed based on the commercial availabilities and the laboratory facilities. Consequently, it is expected that for commercial developments, which are optimized in terms of efficiency for a power rating and specific PV applications, similar or improved efficiencies can be obtained.
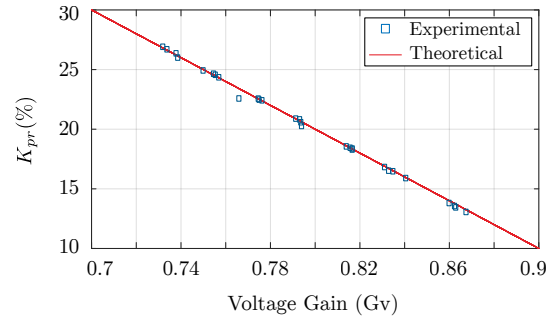
Figure 7.29: Experimental partial power ratio for the Step-Down II Full-bridge based PPC.

From the results obtained by the measurements, it is concluded that the proposed PPC configurations process a fraction of the power. Furthermore, the partiality ratio can vary depending on the voltage difference between the PV voltage and the dc-link voltage. The main feature comes from the fraction of power handled by the converter, which reduces the total converter losses in the system. The analyzed topologies and configurations show that the PPC concept is sufficiently flexible to be implemented for step-up PPC dc-dc stages, which are suitable for microinverters and small PV strings, or for step-down PPC dc-dc stages for larger PV strings. The results show that despite the limitation of processing only a fraction of the power, the converter is capable of retaining the MPPT performance. Moreover the PPC connection used in Step-Up configurations, adds new benefits such as input current ripple reduction, which can extend the lifespan of capacitors.

On the other hand, the operation of the converter depends on the turns ratio of the transformer and the selected topology, all of which also affect the system efficiency. It is also worth mentioning that since the converter efficiency varies depending the power rating, a particular PPC configuration that operates at a lower fraction of power not necessarily translates to higher system efficiency, since it may force the converter to operate at low power ratings where it may not be at its most efficient point. This means that it is necessary to optimize the converter design for a particular partiality given by the system parameters.

Chapter 8

CONCLUSION AND OUTLOOK

In this thesis, the partial power dc-dc converters are presented as possible solution for two-stage PV applications. The benefit of process a reduced portion of the whole power, makes the PPC as an attractive solution in order to increase the conversion efficiency without compromising control performance.

As in all power electronics systems, there is an inherent trade-off between the different performances achieved. The partial power conversion approach, employs traditional isolated dc-dc converters within the dc-stage in order to allow a series connection of active power sources, avoiding short circuits in different switching states. However, the galvanic isolation is lost because of the bypass connection. In addition, the partial power operation (step-up or step-down), does not come from the dc-dc topology but the connection made to built the configuration. Nevertheless, the limitations in terms of converter operation depends on the turns ratio of the transformer and the dc-topology, all of which also affect the system efficiency.

From the investigation related with the partial power conversion approach, the most outstanding benefits obtained from theoretical analysis, simulations and experimental evaluations are:

- *System conversion efficiency:* The dc-stage conversion efficiency increases due to the lower power processed by the converter, so that the losses are related with the efficiency of the isolated dc-dc topology, and the power processed by it. Then, even if the dc-dc converter presents low efficiency in some operation points, specially when high voltage gains are required, the complete efficiency will be higher. On the other hand, the ratio of the power processed by the converter determines the global conversion efficiency.

- *Control performance:* The main objective of a two-stage conversion, besides of decouple the power between the PV and dc-side, is to control inde-

pendently the PV voltage to work at the MPP for increasing the maximum power extracted from the PV system. Therefore, the PPC must operate in partial mode without loosing the MPPT performance, it means that in front of solar irradiations changes the converter must process a reduced power.

- *Volume reduction:* From the theoretical analysis, assuming that a power converter stage is a regular geometric body, and the process for designing is the same as a full power converter, the volume of the partial power converter can be reduced by reducing the power flowing through the dc-dc converter. Moreover, since components with lower current and voltage ratings can be employed, the economic cost of the converter prototype can also decrease. It is also worth noticing that the transformer could be considered as a drawback, however due to the reduced power and high-frequency operation, the transformer size can also be reduced.

- *Power density:* By considering that the density is calculated based on the power processed by the dc-dc converter per volume unit, the power density of the partial power converter increases by reducing the power flowing through the dc-dc converter. Moreover, considering that the dc-stage comprises not only the power processed by the PPC , but also the power flowing trough the direct path, it is possible to conclude that the power density of the dc-stage is highly increased compared with a traditional full power converter.

From the experience obtained starting from the design of the converters, until the evaluation in experimental test-bench. It is worth giving some commentaries which can help to follow the research and extend the presented converters in other applications. First of all, in terms of the prototype construction, the commercial facilities of high-frequency transformers are limited. As was discussed, there is a direct dependence between the turns ratio and operation range, which means that depending the PV application, either larger or fewer turns ratio are required, but in all cases it is better to have a wide voltage range so that this is the series connected voltage source.

In addition, the EMI effects would be considered for further PCB designs of HF dc-dc converters. In this thesis one problem was the interference produced by the switching frequency, specially in the voltage and current sensors. The external filters were not a solution because the frequency of the interference was always located at the sampling frequency.

Finally, in this presented work the main focus was the evaluation of the partial power conversion concept in PV applications. After that, the next step is the improvement of the prototypes design. It should include a further evaluation of topologies so that it would help to improve the performance of each PPC configuration, leading to reach even higher conversion efficiencies.

REFERENCES

[1] B. K. Bose, "Power electronics," 2014. [Online]. Available: http://ethw.org/Power_electronics

[2] ABB, "Power electronics: the hidden technology that makes the modern world run," 2013. [Online]. Available: http://www.abb.com/

[3] REN21, "Renewables 2017 global status report," 2017.

[4] S. Kouro, B. Wu, H. Abu-Rub, and F. Blaabjerg, "Chapter 7: Photovoltaic energy conversion systems," in *Power Electronics for Renewable Energy Systems, Transportation and Industrial Applications*. Wiley, 2014.

[5] S. Kouro, J. Leon, D. Vinnikov, and L. Franquelo, "Grid-connected photovoltaic systems: An overview of recent research and emerging pv converter technology," *Industrial Electronics Magazine, IEEE*, vol. 9, no. 1, pp. 47–61, March 2015.

[6] R. Teodorescu, M. Liserre, and P. Rodriguez, in *Grid Converters for Photovoltaic and Wind Power Systems*. IEEEPressWiley, 2011.

[7] A. Luque and S. Hegedus, in *Handbook of Photovoltaic Science and Engineering*. Wiley, 2011.

[8] H. Haberlin, in *Photovoltaics System Design and Practice*. Wiley, 2012.

[9] S. Shongwe and M. Hanif, "Comparative analysis of different single-diode pv modeling methods," *IEEE Journal of Photovoltaics*, vol. 5, no. 3, pp. 938–946, May 2015.

[10] A. Jain, S. Sharma, and A. Kapoor, "Solar cell array parameters using lambert w-function," *Solar Energy Materials and Solar Cells*, vol. 90, no. 1, pp. 25 – 31, 2006. [Online]. Available: http://www.sciencedirect.com/science/article/pii/S0927024805000334

[11] H. Tian, F. Mancilla-David, K. Ellis, E. Muljadi, and P. Jenkins, "A detailed performance model for photovoltaic systems," *Solar Energy*, Jul.

[12] N. Kishor, M. G. Villalva, S. R. Mohanty, and E. Ruppert, "Modeling of pv module with consideration of environmental factors," in *2010 IEEE PES Inno-*

vative Smart Grid Technologies Conference Europe (ISGT Europe), Oct 2010, pp. 1–5.

[13] D. Picault, B. Raison, S. Bacha, J. de la Casa, and J. Aguilera, "Forecasting photovoltaic array power production subject to mismatch losses," *Solar Energy*, vol. 84, no. 7, pp. 1301 – 1309, 2010. [Online]. Available: http://www.sciencedirect.com/science/article/pii/S0038092X10001556

[14] A. Jain and A. Kapoor, "Exact analytical solutions of the parameters of real solar cells using lambert w-function," *Solar Energy Materials and Solar Cells*, vol. 81, no. 2, pp. 269 – 277, 2004. [Online]. Available: http://www.sciencedirect.com/science/article/pii/S0927024803002605

[15] H. Fathabadi, "Lambert w function-based technique for tracking the maximum power point of pv modules connected in various configurations," *Renewable Energy*, vol. 74, pp. 214 – 226, 2015. [Online]. Available: http://www.sciencedirect.com/science/article/pii/S0960148114004571

[16] J. W. Zapata, M. A. Perez, S. Kouro, A. Lensu, and A. Suuronen, "Design of a cleaning program for a pv plant based on analysis of energy losses," *IEEE Journal of Photovoltaics*, vol. 5, no. 6, pp. 1748–1756, Nov 2015.

[17] SolarWorld, "Sunmodule sw 285-290 mono black," 2017. [Online]. Available: http://www.solarworld-usa.com/products-and-services/sunmodule-solar-panels

[18] E. I. Batzelis, I. A. Routsolias, and S. A. Papathanassiou, "An explicit pv string model based on the lambert w function and simplified mpp expressions for operation under partial shading," *IEEE Transactions on Sustainable Energy*, vol. 5, no. 1, pp. 301–312, Jan 2014.

[19] G. Walker and J. Pierce, "Photovoltaic dc-dc module integrated converter for novel cascaded and bypass grid connection topologies - design and optimisation," in *Power Electronics Specialists Conference, 2006. PESC '06. 37th IEEE*, June 2006, pp. 1–7.

[20] T. V. Thang, A. Ahmed, C. i. Kim, and J. H. Park, "Flexible system architecture of stand-alone pv power generation with energy storage device," *IEEE Transactions on Energy Conversion*, vol. 30, no. 4, pp. 1386–1396, Dec 2015.

[21] A. J. C. of Govt of Andhra Pradesh & Govt of India, "Kurnool ultra mega solar park (1000 mw)," 2017. [Online]. Available: http://apspcl.ap.gov.in/content/kurnoolultramegasolarparks

[22] F. Blaabjerg, Z. Chen, and S. B. Kjaer, "Power electronics as efficient interface in dispersed power generation systems," *IEEE Transactions on Power Electronics*, vol. 19, no. 5, pp. 1184–1194, Sept 2004.

[23] M. Calais, J. Myrzik, T. Spooner, and V. Agelidis, "Inverters for single-phase grid connected photovoltaic systems-an overview," in *Power Electronics Specialists Conference, 2002. pesc 02. 2002 IEEE 33rd Annual*, vol. 4, 2002, pp. 1995–2000.

[24] J. Muñoz Cruzado-Alba, C. A. Rojas, S. Kouro, and E. Galván Díez, "Power production losses study by frequency regulation in weak-grid-connected utility-scale photovoltaic plants," *Energies*, vol. 9, no. 5, 2016. [Online]. Available: http://www.mdpi.com/1996-1073/9/5/317

[25] M. Kasper, D. Bortis, and J. W. Kolar, "Classification and comparative evaluation of pv panel-integrated dc/dc converter concepts," *IEEE Transactions on Power Electronics*, vol. 29, no. 5, pp. 2511–2526, May 2014.

[26] Huawei, "Sun2000-36-42ktl," 2017. [Online]. Available: http://www.huawei.com/en/all-products/Solar/Product/Smart-PV-Cotroller/

[27] Y. shi, L. Wang, R. Xie, Y. Shi, and H. Li, "A 60kw 3kw/kg 5-level t-type sic pv inverter with 99.2% peak efficiency," *IEEE Transactions on Industrial Electronics*, vol. PP, no. 99, pp. 1–1, 2017.

[28] J. W. Kolar, F. Krismer, Y. Lobsiger, J. Muhlethaler, T. Nussbaumer, and J. Minibock, "Extreme efficiency power electronics," in *2012 7th International Conference on Integrated Power Electronics Systems (CIPS)*, March 2012, pp. 1–22.

[29] M. Kasper, D. Bortis, and J. W. Kolar, "Scaling and balancing of multi-cell converters," in *2014 International Power Electronics Conference (IPEC-Hiroshima 2014 - ECCE ASIA)*, May 2014, pp. 2079–2086.

[30] S. Muller, M. Deicke, and R. W. D. Doncker, "Doubly fed induction generator systems for wind turbines," *IEEE Industry Applications Magazine*, vol. 8, no. 3, pp. 26–33, May 2002.

[31] R. M. Button, "An advanced photovoltaic array regulator module," in *Energy Conversion Engineering Conference, 1996. IECEC 96., Proceedings of the 31st Intersociety*, vol. 1, Aug 1996, pp. 519–524 vol.1.

[32] J. P. Lee, B. D. Min, T. J. Kim, D. W. Yoo, and J. Y. Yoo, "A novel topology for photovoltaic dc/dc full-bridge converter with flat efficiency under wide pv module voltage and load range," *IEEE Transactions on Industrial Electronics*, vol. 55, no. 7, pp. 2655–2663, July 2008.

[33] B. D. Min, J. P. Lee, J. H. Kim, T. J. Kim, D. W. Yoo, and E. H. Song, "A new topology with high efficiency throughout all load range for photovoltaic pcs," *IEEE Transactions on Industrial Electronics*, vol. 56, no. 11, pp. 4427–4435, Nov 2009.

[34] J. i. Itoh and T. Fujii, "A new approach for high efficiency buck-boost dc/dc converters using series compensation," in *2008 IEEE Power Electronics Specialists Conference*, June 2008, pp. 2109–2114.

[35] H. Kim, J. Kim, H. Kim, K. Lee, J. Kim, D. Yoo, and D. Shin, "A high efficiency photovoltaic module integrated converter with the asymmetrical half-bridge flyback converter," *Solar Energy*, vol. 84, no. 8, pp. 1376 – 1381, 2010. [Online]. Available: http://www.sciencedirect.com/science/article/pii/S0038092X10001787

[36] J. Zhao, K. Yeates, and Y. Han, "Analysis of high efficiency dc/dc converter processing partial input/output power," in *Control and Modeling for Power Electronics (COMPEL), 2013 IEEE 14th Workshop on*, June 2013, pp. 1–8.

[37] M. Harfman-Todorovic, F. Tao, M. Agamy, D. Dong, X. Liu, L. Garces, R. Zhou, E. Delgado, D. Marabell, C. Stephens, and R. Steigerwald, "A high efficiency pv micro-inverter with grid support functions," in *2014 IEEE Energy Conversion Congress and Exposition (ECCE)*, Sept 2014, pp. 4244–4250.

[38] J. W. Zapata, H. Renaudineau, S. Kouro, M. A. Perez, and T. A. Meynard, "Partial power dc-dc converter for photovoltaic microinverters," in *IECON 2016 - 42nd Annual Conference of the IEEE Industrial Electronics Society*, Oct 2016, pp. 6740–6745.

[39] J. R. R. Zientarski, J. R. Pinheiro, M. L. d. S. Martins, and H. L. Hey, "Understanding the partial power processing concept: A case-study of buck-boost dc/dc series regulator," in *2015 IEEE 13th Brazilian Power Electronics Conference and 1st Southern Power Electronics Conference (COBEP/SPEC)*, Nov 2015, pp. 1–6.

[40] H. Zhou, J. Zhao, and Y. Han, "Pv balancers: Concept, architectures, and realization," *IEEE Transactions on Power Electronics*, vol. 30, no. 7, pp. 3479–3487, July 2015.

[41] A. Morrison, J. W. Zapata, S. Kouro, M. A. Perez, T. A. Meynard, and H. Renaudineau, "Partial power dc-dc converter for photovoltaic two-stage string inverters," in *2016 IEEE Energy Conversion Congress and Exposition (ECCE)*, Sept 2016, pp. 1–6.

[42] A. D. Marzouk, S. Fournier-Bidoz, J. Yablecki, K. McLean, and O. Trescases, "Analysis of partial power processing distributed mppt for a pv powered electric aircraft," in *2014 International Power Electronics Conference (IPEC-Hiroshima 2014 - ECCE ASIA)*, May 2014, pp. 3496–3502.

[43] J. H. R. Enslin and D. B. Snyman, "Combined low-cost, high-efficient inverter, peak power tracker and regulator for pv applications," *IEEE Transactions on Power Electronics*, vol. 6, no. 1, pp. 73–82, Jan 1991.

[44] J. W. Zapata, T. A. Meynard, and S. Kouro, "Multi-channel partial power dc-dc converter for current balancing of led strings," in *2017 IEEE 26th International Symposium on Industrial Electronics (ISIE)*, June 2017, pp. 775–780.

[45] ——, "Partial power dc-dc converter for large-scale photovoltaic systems," in *2016 IEEE 2nd Annual Southern Power Electronics Conference (SPEC)*, Dec 2016, pp. 1–6.

[46] M. Kazimierczuk, *Pulse-width Modulated Dc-Dc Power Converters.* IEEE/Wiley, 2008.

[47] R. Watson, F. C. Lee, and G. C. Hua, "Utilization of an active-clamp circuit to achieve soft switching in flyback converters," *IEEE Transactions on Power Electronics*, vol. 11, no. 1, pp. 162–169, Jan 1996.

[48] M. Albach, T. Durbaum, and A. Brockmeyer, "Calculating core losses in transformers for arbitrary magnetizing currents a comparison of different approaches," in *PESC Record. 27th Annual IEEE Power Electronics Specialists Conference*, vol. 2, Jun 1996, pp. 1463–1468 vol.2.

[49] M. Rosekeit, J. Burkard, M. Lelie, D. U. Sauer, and R. W. D. Doncker, "Full-bridge dc-dc converter with planar transformer and center-tap rectifier for fuel cell powered uninterruptible power supply," in *Power Electronics and Applications (EPE'14-ECCE Europe), 2014 16th European Conference on*, Aug 2014, pp. 1–10.

[50] L. A. R. Tria, D. Zhang, and J. E. Fletcher, "Implementation of a nonlinear planar magnetics model," *IEEE Transactions on Power Electronics*, vol. 31, no. 9, pp. 6534–6542, Sept 2016.

[51] A. Mohammadpour, L. Parsa, M. H. Todorovic, R. Lai, R. Datta, and L. Garces, "Series-input parallel-output modular-phase dc-dc converter with soft-switching and high-frequency isolation," *IEEE Transactions on Power Electronics*, vol. 31, no. 1, pp. 111–119, Jan 2016.

[52] A. Ammouri, T. B. Salah, and F. Kourda, "Modeling and simulation of a high-frequency planar power transformers," in *2015 4th International Conference on Electrical Engineering (ICEE)*, Dec 2015, pp. 1–6.

[53] AN-9005, "Driving and layout design for fast switching super-junction mosfets," 2013.

[54] SLPA010, "Ringing reduction techniques for nexfet high performance mosfets," 2011.

[55] L. A. R. Tria, D. Zhang, and J. E. Fletcher, "High-frequency planar transformer parameter estimation," *IEEE Transactions on Magnetics*, vol. 51, no. 11, pp. 1–4, Nov 2015.

[56] S. R. Cove, M. Ordonez, F. Luchino, and J. E. Quaicoe, "Applying response surface methodology to small planar transformer winding design," *IEEE Transactions on Industrial Electronics*, vol. 60, no. 2, pp. 483–493, Feb 2013.

[57] T. Meng, S. Yu, H. Ben, and G. Wei, "A family of multilevel passive clamp circuits with coupled inductor suitable for single-phase isolated full-bridge boost pfc converter," *IEEE Transactions on Power Electronics*, vol. 29, no. 8, pp. 4348–4356, Aug 2014.

[58] H. Cha, L. Chen, R. Ding, Q. Tang, and F. Z. Peng, "An alternative energy recovery clamp circuit for full-bridge pwm converters with wide ranges of input voltage," *IEEE Transactions on Power Electronics*, vol. 23, no. 6, pp. 2828–2837, Nov 2008.

[59] E.-S. Park, S. J. Choi, J. M. Lee, and B. H. Cho, "A soft-switching active-clamp scheme for isolated full-bridge boost converter," in *Applied Power Electronics Conference and Exposition, 2004. APEC '04. Nineteenth Annual IEEE*, vol. 2, 2004, pp. 1067–1070 vol.2.

[60] M. Fornage, "Method and Apparatus for Converting Direct Current To Alternating Current," US patent 2007/0221267A1, 2007.

[61] T. LaBella, W. Yu, J. S. . Lai, M. Senesky, and D. Anderson, "A bidirectional-switch-based wide-input range high-efficiency isolated resonant converter for photovoltaic applications," *IEEE Transactions on Power Electronics*, vol. 29, no. 7, pp. 3473–3484, July 2014.

[62] E. Serban, M. Ordonez, and C. Pondiche, "Dc-bus voltage range extension in 1500 v photovoltaic inverters," *IEEE Journal of Emerging and Selected Topics in Power Electronics*, vol. 3, no. 4, pp. 901–917, Dec 2015.

[63] N. Femia, G. Petrone, G. Spagnuolo, and M. Vitelli, "Optimization of perturb and observe maximum power point tracking method," *IEEE Transactions on Power Electronics*, vol. 20, no. 4, pp. 963–973, July 2005.

[64] J. W. Zapata, S. Kouro, M. Aguirre, and T. Meynard, "Model predictive control of interleaved dc-dc stage for photovoltaic microconverters," in *Industrial Electronics Society, IECON 2015 - 41st Annual Conference of the IEEE*, Nov 2015, pp. 004 311–004 316.

[65] Y. Lian, G. Adam, D. Holliday, and S. Finney, "Modular input-parallel output-series dc/dc converter control with fault detection and redundancy," *IET Generation, Transmission Distribution*, vol. 10, no. 6, pp. 1361–1369, 2016.